Alternative splicing of CARM1 regulated by *LincGET*-guided paraspeckles biases the first cell fate in mammalian early embryos

Check for updates

Jiaqiang Wang [1] ✉, Yiwei Zhang [1], Jiaze Gao[1], Guihai Feng [2], Chao Liu[2], Xueke Li[1,2], Pengcheng Li[1,2], Zhonghua Liu[1], Falong Lu [3,4], Leyun Wang [2] ✉, Wei Li [2,4,5] ✉, Qi Zhou [2,4,5] ✉ & Yusheng Liu [6] ✉

The heterogeneity of CARM1 controls first cell fate bias during early mouse development. However, how this heterogeneity is established is unknown. Here, we show that *Carm1* mRNA is of a variety of specific exon-skipping splicing (ESS) isoforms in mouse two-cell to four-cell embryos that contribute to CARM1 heterogeneity. Disruption of paraspeckles promotes the ESS of *Carm1* precursor mRNAs (pre-mRNAs). *LincGET*, but not *Neat1*, is required for paraspeckle assembly and inhibits the ESS of *Carm1* pre-mRNAs in mouse two-cell to four-cell embryos. We further find that *LincGET* recruits paraspeckles to the *Carm1* gene locus through HNRNPU. Interestingly, PCBP1 binds the *Carm1* pre-mRNAs and promotes its ESS in the absence of *LincGET*. Finally, we find that the ESS seen in mouse two-cell to four-cell embryos decreases CARM1 protein levels and leads to trophectoderm fate bias. Our findings demonstrate that alternative splicing of CARM1 has an important role in first cell fate determination.

During mammalian early embryonic development, the first two lineages to emerge are the trophectoderm and the inner cell mass. When and how the first cell fate bias happens remains the topic of intense investigation. The shreds of evidence to date suggest that the initial heterogeneities in CARM1 (which is regulated by the endogenous retrovirus (ERV)-associated nuclear long intergenic non-coding RNA *LincGET*[1,2]) and paraspeckles[3] is the key epigenetic basis to influence first cell fate determination. However, how the CARM1 heterogeneity is established remains largely unknown. Alternative splicing is the most prominent mechanism to generate mRNA structural complexity[4,5], which participates in various cell processes[6,7] including cell fate decisions, as it regulates stem cell differentiation[8–10] and epithelial–mesenchymal transitions[11–13].

It is well known that the nuclei contain distinct classes of subnuclear bodies that mediate RNA splicing, including splicing speckles and paraspeckles. The splicing speckles function as storage sites for the splicing factors[14]. Paraspeckles have been reported to be involved in numerous nuclear events, including DNA unwinding, transcriptional regulation, RNA splicing, RNA editing and nuclear retention of some RNAs[15,16]. The function of the subnuclear bodies is determined by their location, which is always regulated by their long non-coding RNA (lncRNA) component[17]. For example, paraspeckles are built around the *Neat1* lncRNA[18,19]. However, *Neat1* is not the only lncRNA involved in paraspeckles. Another lncRNA, termed CTN-RNA, is specifically localized to paraspeckles of numerous cell types[16]. It is reported that alternative splicing during mouse pre-implantation development is

[1]College of Life Science, Northeast Agricultural University, Harbin, China. [2]State Key Laboratory of Stem Cell and Reproductive Biology, Institute of Zoology, Chinese Academy of Sciences, Beijing, China. [3]State Key Laboratory of Molecular Developmental Biology, Institute of Genetics and Developmental Biology, Chinese Academy of Sciences, Beijing, China. [4]University of Chinese Academy of Sciences, Beijing, China. [5]Institute for Stem Cell and Regeneration, Chinese Academy of Sciences, Beijing, China. [6]College of Life Science, Northeast Forestry University, Harbin, China. ✉e-mail: wangjiaqiang@neau.edu.cn; wangleyun0828@hotmail.com; liwei@ioz.ac.cn; qzhou@ioz.ac.cn; liuys1126@foxmail.com

extremely complicated and extraordinary, and stage-linked splicing is related to embryonic development[20–23]. Therefore, we wonder whether alternative splicing may contribute to the first cell fate bias.

Results

Alternative splicing contributes to CARM1 heterogeneity

Given that alternative splicing is involved in cell fate decisions[8–13], we questioned whether alternative splicing contributes to CARM1 heterogeneity, which was established in two-cell to four-cell mouse embryos[3,24]. We analyzed the level of different types of alternative splicing events of *Carm1* pre-mRNAs, including exon-skipping, retained introns, alternative 5′-splicing site, alternative 3′-splicing site, mutually exclusive exons, alternative first exons and alternative last exons, using RNA sequencing (RNA-seq) data from mouse cell lines, tissues, gametes and early embryos. The result indicated a distinguishing feature of the two-cell to four-cell embryos: they presented the highest relative ratio of abnormal ESS events on exons 3 to 6 of *Carm1* pre-mRNAs among all analyzed transcriptomes, including exon 3 skipping (E3S), exon 5 skipping (E5S), exon 6 skipping (E6S), exon 5 and 6 skipping (E56S), and exon 3, 4, 5 and 6 skipping (E3456S). Other alternative splicing types were minimally detectable or not specific in two-cell to four-cell embryos (Fig. 1a,b, Extended Data Fig. 1, Supplementary Fig. 1 and Supplementary Table 1).

Intrigued by these distinguishing features, we used systematic parallel analysis of endogenous RNA regulation coupled to barcode sequencing (SPAR-seq)[25] to deeply analyze the ESS events around exons 3 to 6 of *Carm1* pre-mRNAs in mouse two-cell and four-cell embryos. Firstly, the SPAR-seq library was sequenced on a PacBio third-generation sequencer, and we confirmed the existence of ESS events around exons 3 to 6 of *Carm1* pre-mRNAs (Extended Data Fig. 2a and Supplementary Tables 2 and 3). Then we performed SPAR-seq at a single-cell level on an Illumina MiSeq sequencer under PE300 mode, using the synthetic *Gfp* RNA fragment as the spike-in. Consequently, we observed heterogeneous ESS of *Carm1* pre-mRNAs between blastomeres in both two-cell and four-cell embryos, whereas the levels of total *Carm1* transcripts were consistent among blastomeres as measured by single-cell quantitative PCR (qPCR) analysis (Fig. 1c). These results were confirmed by gel electrophoresis analysis of SPAR assays (Extended Data Fig. 2b). In addition, the RNA-seq results showed that the transcript levels of *Carm1* are similar between the two-cell and the four-cell stages (Extended Data Fig. 2c), which was confirmed by qPCR (Extended Data Fig. 2d), reflecting a relatively stable transcription of *Carm1* in two-cell to four-cell embryos.

The above results indicate that ESS on exons 3 to 6 of *Carm1* pre-mRNAs, encoding a key SAM-methyltransferase domain of CARM1, is specific and heterogeneous in mouse two-cell to four-cell embryos, which raises a new level of CARM1 that is heterogeneous for first cell fate bias. Therefore, we focus on ESS events on exons 3 to 6 of *Carm1* pre-mRNAs.

Although the ratios of exon 15 skipping splicing (E15S) and exon 11 skipping splicing (E11S) are probably higher than the skipping of exons 3 to 6, we did not focus on E15S and E11S for two reasons. First, E15S and E11S do not affect the CARM1 protein level, which was confirmed by transforming them into HEK293T cells and detecting the translated

products with western blotting using anti-HA antibody (Extended Data Fig. 2e). Second, E15S and E11S are not specific for two-cell and four-cell embryos, in which CARM1 heterogeneity is established.

Paraspeckle components inhibit the ESS of *Carm1* pre-mRNAs

Given that paraspeckles have been reported to regulate RNA splicing[15,16] and pre-implantation mouse embryo development[3], we wondered whether paraspeckle components regulate ESS of *Carm1* pre-mRNAs in mouse early embryos. Overexpression of *Nono* or *Pspc1* did not affect the ESS of *Carm1* pre-mRNAs; however, depletion of *Nono* or *Pspc1* increased the ESS of *Carm1* pre-mRNAs in mouse four-cell embryos, which was evident not only from the reverse transcription PCR (RT–PCR) results (Extended Data Fig. 3a,b) but also from SPAR-seq (Fig. 2a and Extended Data Fig. 3c). These results suggest that paraspeckle components inhibit the ESS of *Carm1* pre-mRNAs in mouse early embryos.

LincGET guides paraspeckle assembly in mouse early embryos

Paraspeckles in somatic cells are built around *Neat1* (ref. 18); however, we found that *Neat1* ablation did not affect the ESS of *Carm1* pre-mRNAs (Extended Data Fig. 3a,b). Moreover, we found that paraspeckles were assembled normally in mouse four-cell embryos upon *Neat1* ablation, along with partial re-localization of NONO from paraspeckles to the periphery of the nucleoli in 10 out of 25 embryos (Extended Data Fig. 3d), which is consistent with previous results[3]. These results reflect that *Neat1* is not essential for paraspeckle assembly in mouse early embryos. Therefore, we questioned whether there are other lncRNAs essential for the paraspeckle organization in mouse early embryos.

We previously found that *LincGET* forms granules with CARM1 in the nucleus of mouse two-cell to four-cell embryos[1], and it has been reported that CARM1 is involved in paraspeckles during this stage[3]. Interestingly, *LincGET* depletion increases and *LincGET* overexpression decreases the ESS of *Carm1* pre-mRNAs (Fig. 2a and Extended Data Fig. 3a–c), which is consistent with the previous RNA-seq data[2] (Extended Data Fig. 3e) and raises a possibility that *LincGET* may participate in the organization of paraspeckles in mouse early embryos.

The expression patterns of NONO and PSPC1 were highly consistent with that of *LincGET*, which bursts at the two-cell to four-cell stage (Extended Data Fig. 4a,b). Further analysis indicated the co-localization between *LincGET* and paraspeckles in mouse two-cell and four-cell embryos (Pearson's correlation coefficient (Rp) ≈ 0.7; Extended Data Fig. 4a).

To further confirm that *LincGET* is localized to paraspeckles, we tested the interaction between *LincGET* and components of paraspeckles using MS2-fused *LincGET* (*LincGET-MS2*) and an HA-tagged MS2 bacteriophage coat proteins (MS2P) system[26]. We performed RNA immunoprecipitation (RIP) and co-immunoprecipitation (co-IP) assays and found that *LincGET* forms complexes with NONO and PSPC1 (Fig. 2b). Furthermore, with a series of *LincGET-MS2* mutants, we found that the G-H-I fragment of *LincGET* is essential for its binding to NONO and PSPC1 (Fig. 2b).

To confirm these results, we performed selective 2′-hydroxyl acylation analyzed by primer extension and mutational profiling (SHAPE-MaP) assays[27]. By comparing the SHAPE-MaP data from in vitro transcribed *LincGET* under protein-free conditions (naked) and upon

---

Fig. 1 | Alternative splicing of exons encoding key SAM-methyltransferase domain of CARM1 is specific and heterogeneous in mouse two-cell to four-cell embryos. a, Sashimi plots visualizing that ESS happens on exons 5 and 6 of *Carm1* pre-mRNAs in mouse two-cell (2C)[2] embryos but not in mouse embryonic stem (mES) cells[51], mouse embryonic fibroblasts (MEFs)[52], NIH-3T3 cells, heart[53], kidney or liver[54] tissues. Each line represents one set of data. The constitutive splicing events are shown as gray arcs and the alternative splicing events are shown as red arcs. RPKM, reads per kilobase per million mapped reads. **b**, Percentage of ESS events on exons 3 to 6 of *Carm1* pre-mRNAs in mouse gametes, early embryos, cell lines and tissues. Each column represents a sample containing all replicates from the published data of others; three samples were used for each group (see Supplementary Table 1 for details). GV, germinal vesicle; MII, metaphase II; MO, morula stage; noS, non-skipping splicing; BL, blastocyst stage. See Methods for calculations. **c**, Single-cell SPAR-seq results for *Carm1* ESS analysis and single-cell qPCR results for *Carm1* expression level analysis in mouse 2C and 4C embryos. Each dot (top) and each column (bottom) represents one blastomere. The relative level of ESS and expression among blastomeres in the same embryo are shown in red and blue, respectively (top). The percentage of ESS events relative to noS splicing events in a single blastomere of each embryo is shown in the histogram (bottom).
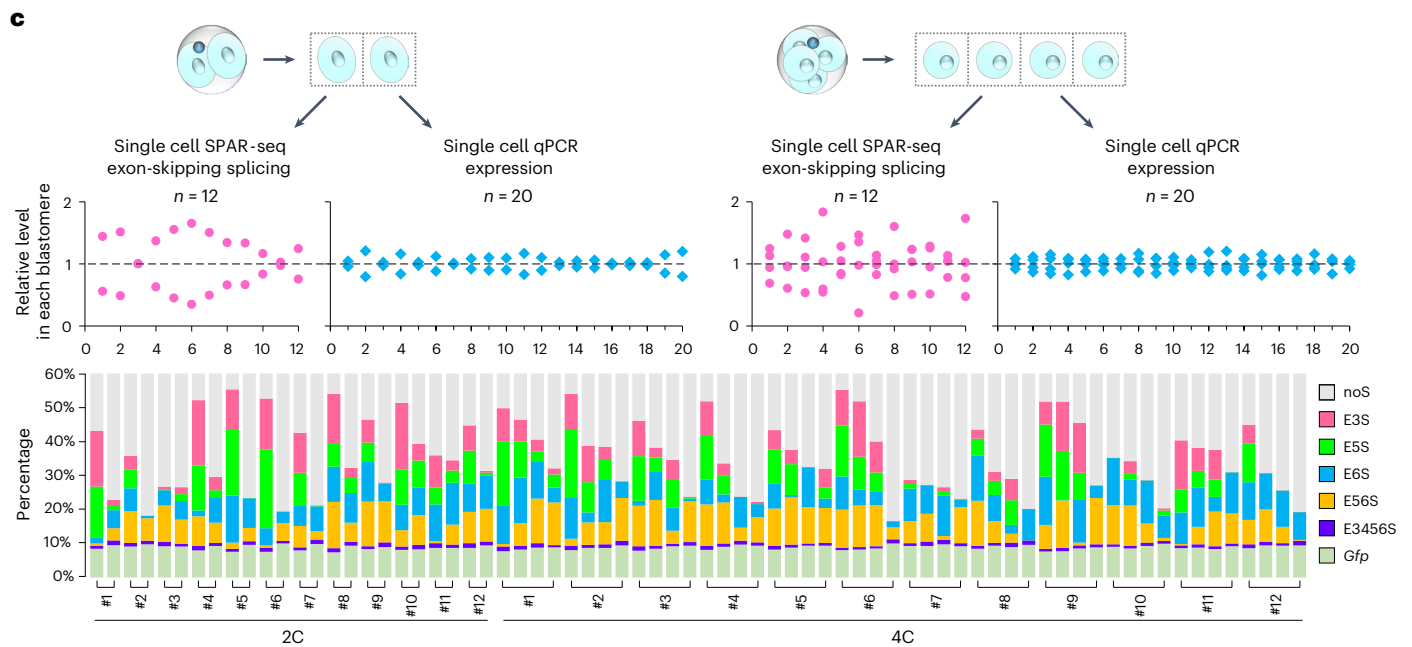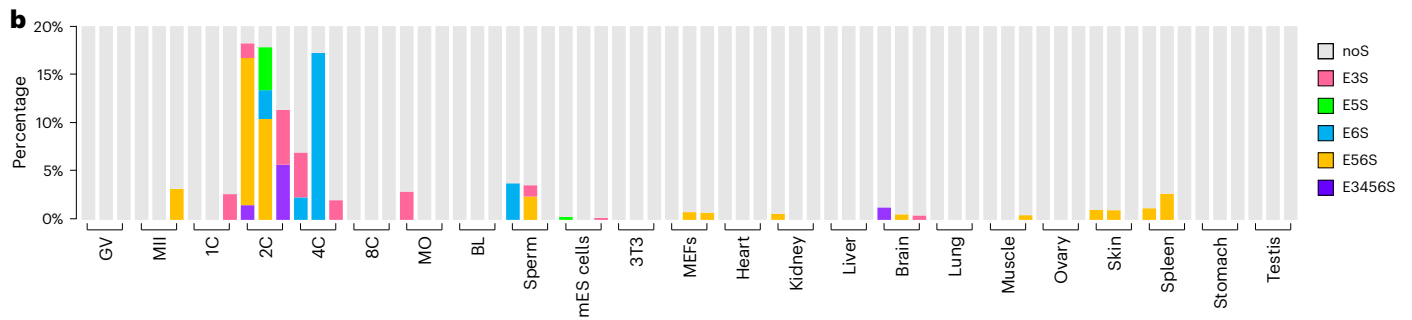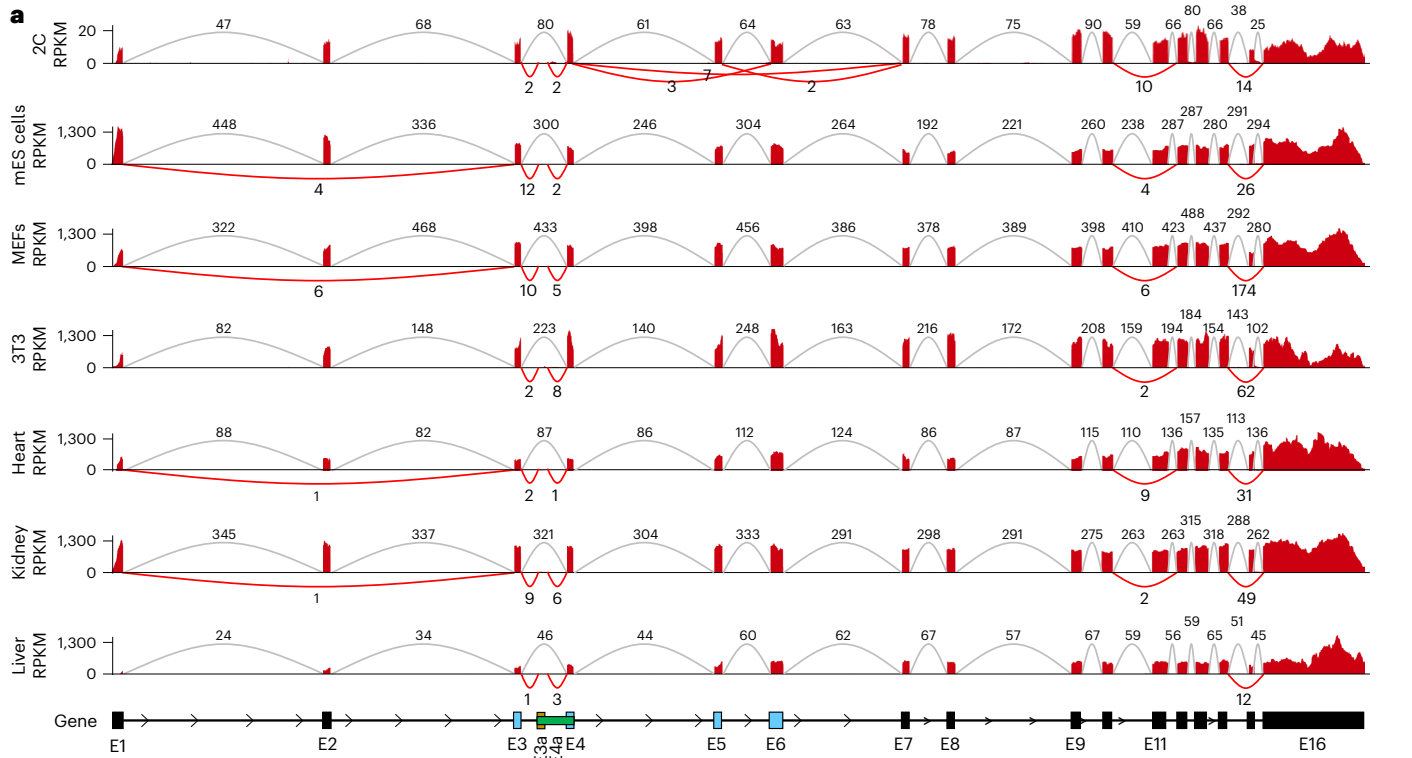
incubation with NONO or PSPC1 (bonded), we found that NONO and PSPC1 bind the 3,550–5,450 fragments of nucleotides of *LincGET* (Fig. 2c). The NONO/PSPC1-binding region of *LincGET* is enriched of sequences from MERVL and MERVK (Fig. 2c), which is consistent with the results of others[28]. We injected the *LincGET-MS2*, HA-tagged MS2P and NONO at the pronuclear stage and performed co-IP at the early four-cell stage. The results showed that *LincGET* forms complexes with NONO, PSPC1 and *Carm1* pre-mRNA in mouse four-cell embryos (Fig. 2d).

We found that most *LincGET* speckles disintegrated into the nucleoplasm without either NONO or PSPC1, and the paraspeckles disappeared when *LincGET* was depleted (Fig. 2e), just like *Neat1* ablation for paraspeckles in HeLa and NIH-3T3 cells[18]. Together, these results indicate that *LincGET*, rather than *Neat1*, guides the assembly of paraspeckles in mouse two-cell to four-cell embryos, which differs from paraspeckles in somatic cells.

Paraspeckle assembly is essential for *Carm1* ESS inhibition

As *LincGET* regulates the ESS of *Carm1* pre-mRNAs and guides the assembly of paraspeckles in mouse two-cell to four-cell embryos, we wondered whether the assembly of paraspeckles is essential for inhibiting ESS of *Carm1* pre-mRNAs. Therefore, we injected *Nono* and a series of truncated *LincGET* into mouse two-cell embryos in which the endogenous *LincGET* was depleted and found that no paraspeckles formed in ΔG, ΔH and ΔI groups (Fig. 2f and Extended Data Fig. 4c), indicating that the interaction between *LincGET* and NONO is needed for paraspeckle assembly in mouse early embryos. Moreover, we found that the ESS of *Carm1* pre-mRNAs increased when the endogenic *LincGET* was replaced by deletion mutants without the NONO/PSPC1-binding domain (ΔG, ΔH and ΔI in Fig. 2g and Extended Data Fig. 4d), reflecting that assembled paraspeckles are essential for inhibiting ESS of *Carm1* pre-mRNAs.

The D–E domain of *LincGET* regulates paraspeckle localization

Notably, the ESS of *Carm1* pre-mRNAs also increased when the endogenic *LincGET* was replaced by deletion mutants without the D–E domain (Fig. 2g, Extended Data Fig. 4d), whereas the assembly of paraspeckles is normal in deletion mutants without the D–E domain (Fig. 2f and Extended Data Fig. 4c), indicating that other mechanisms in addition to paraspeckle assembly are involved in the inhibition of ESS of *Carm1* pre-mRNAs.

As pre-mRNA is subjected to splicing during its synthesis[29], we questioned whether the localization of paraspeckles is the mechanism beyond paraspeckle assembly. Using RNA fluorescence in situ hybridization (RNA-FISH) combined with DNA-FISH, we found that *LincGET* locates to the *Carm1* gene locus (Fig. 3a), reflecting that a paraspeckle assembles around the *Carm1* gene locus. To confirm these results, we injected the *LincGET-MS2* and HA-tagged MS2P at the pronuclear stage and performed chromatin immunoprecipitation followed by high-throughput sequencing (ChIP–seq) using an anti-HA antibody at the early four-cell stage (*LincGET* ChIP–seq) to explore the genome-wide *LincGET*-binding sites. The results showed that *LincGET*

indeed binds around the *Carm1* gene locus, tending to bind long terminal repeats (LTRs) (Extended Data Fig. 5a). Generally, we found that *LincGET* tends to bind repeat elements, such as long interspersed nuclear elements (LINEs, 59.76%) and LTRs (32.52%) (Fig. 3b), which is consistent with our reports that *LincGET* increases chromatin openness around retrotransposon elements[1].

It has been reported that lncRNA *Terra* consists of repeat sequences and maintains telomeric structure through sequence complementarity with R-loop formation[30]. As *LincGET* also consists of repeat sequences, most of which are from ERV, we reasoned that *LincGET* can bind ERV-associated LTRs by sequence complementarity. To test this hypothesis, we used the LongTarget prediction tool[31] and found that *LincGET* binds to the *Carm1* gene locus at multiple sites, especially the LTRs and LINEs with higher mean identity (Extended Data Fig. 5a and Supplementary Table 4), which is consistent with the results of *LincGET* ChIP–seq. These results suggested that *LincGET* binds to the *Carm1* gene locus through sequence complementarity.

Next, we questioned whether the D–E domain of *LincGET* guides the localization of paraspeckles. We took advantage of CRISPR-mediated live imaging of the genome[32] (Supplementary Table 3), and used blue fluorescent protein (BFP)-labeled NONO to visualize paraspeckles (Fig. 3c). As a result, we discovered that no paraspeckles formed when the endogenic *LincGET* was replaced by deletion mutants without the G, H or I domain (Fig. 3d and Extended Data Fig. 5b) and paraspeckles formed but no longer targeted the *Carm1* gene locus when the endogenic *LincGET* was replaced by deletion mutants without the D or E domain (Fig. 3d and Extended Data Fig. 5b). These results reveal that the NONO/PSPC1-binding domain of *LincGET* is essential for paraspeckle assembly, and the D–E domain of *LincGET* is essential for paraspeckle localization to the *Carm1* gene locus, both of which are needed for inhibiting ESS of *Carm1* pre-mRNAs.

LincGET–HNRNPU complex guides paraspeckle localization

Given that the interaction between RNA and chromatin needs chromatin-associated proteins[33], we reasoned that chromatin-associated proteins bind the D–E domain of *LincGET* and regulate its association with the *Carm1* gene locus. We previously reported that *LincGET* binds heterogeneous nuclear ribonucleoprotein U (HNRNPU)[2], which has a critical role in the high-order organization of the nucleus[34]. We next wondered whether the D–E domain of *LincGET* interacts with HNRNPU. Results of the RIP and co-IP assays showed that the D–E domain of *LincGET* is crucial for HNRNPU binding (Fig. 3e), and these findings were confirmed by the SHAPE-MaP assays (Fig. 3f), indicating that the D–E domain of *LincGET* interacts with HNRNPU. In addition, the analysis of fluorescence staining results indicated the co-localization between *LincGET* and HNRNPU in mouse four-cell embryos (Rp ≈ 0.70; Fig. 3g).

We next investigated whether HNRNPU is essential for mediating the chromatin localization of *LincGET*-guided paraspeckles. We observed that HNRNPU depletion (Extended Data Fig. 5c) did not affect the assembly of paraspeckles but did result in an inability of

Fig. 2 | *LincGET*-guided assembly of paraspeckles is essential for protecting *Carm1* from ESS. a, Combination charts of bar plots and dot plots showing the percentage of ESS events of *Carm1* pre-mRNAs in 4C embryos measured by SPAR-seq. Data are mean and s.e.m. One-tailed Student's *t*-tests were used for statistical analysis (*n* = 3 biological replicates). i- denotes knockdown by RNA interference. **b**, Co-IP followed by RT–PCR and western blot in mouse epiblast stem cells (mEpiSCs). Three biological replicates were performed. Full denotes full-length *LincGET* without LNA-targeting sites; rev denotes the reverse sequence of *LincGET*. **c**, SHAPE-MaP assays. Alu denotes transposon elements originally from *Arthrobacter luteus* restriction endonuclease; MMERGLN, MERVK and MERVL are transposon elements from mouse ERV with tRNA^Gln, tRNA^Lys(K) and tRNA^Leu(L), respectively. **d**, Co-IP followed by RT–PCR and western blot in early 4C (E4C) embryos. Three biological replicates were performed. **e**, Immunofluorescence

combined with RNA-FISH assays in late 2C (L2C). Scale bar, 10 μm. Top right, line scans of the relative fluorescence intensity of signals indicated by the dotted line in the left panel. Bottom right, the relationship between the numbers of *LincGET* speckles and NONO or PSPC1 speckles calculated by Imaris (19 × 4 cells of i-control group, 19 × 4 cells of i-*Nono* group, and 15 × 4 cells of i-*Pspc1* group) is shown in dot plots. **f**, Single nucleus of L2C injected with fluorescently labeled *LincGET* and NONO. Scale bar, 10 μm. Bottom, line scans of the relative fluorescence intensity of signals indicated by the dotted line in the top panel. **g**, Agarose gel analysis of RT–PCR (top) and quantification (bottom). AS, alternative splicing. Data are mean and s.e.m. One-tailed Student's *t*-tests were used for statistical analysis and *P* values are shown in Extended Data Fig. 4d (*n* = 3 biological replicates). Rp values in **e** and **f** were calculated by Fiji/ImageJ.

paraspeckles to localize to the *Carm1* gene locus (Fig. 3h and Extended Data Fig. 5d), reflecting that HNRNPU is necessary for the localization of paraspeckles to the *Carm1* gene locus. Therefore, we conclude that the *LincGET*–HNRNPU interaction is indispensable for the correct

localization of paraspeckles in mouse two-cell to four-cell embryos. As mentioned above, the results of the *LincGET* ChIP–seq revealed that *LincGET* binds LTR and LINE elements in the *Carm1* gene locus, which was confirmed by LongTarget (Fig. 3b, Extended Data Fig. 5a and

Nature Structural & Molecular Biology | Volume 31 | September 2024 | 1341–1354
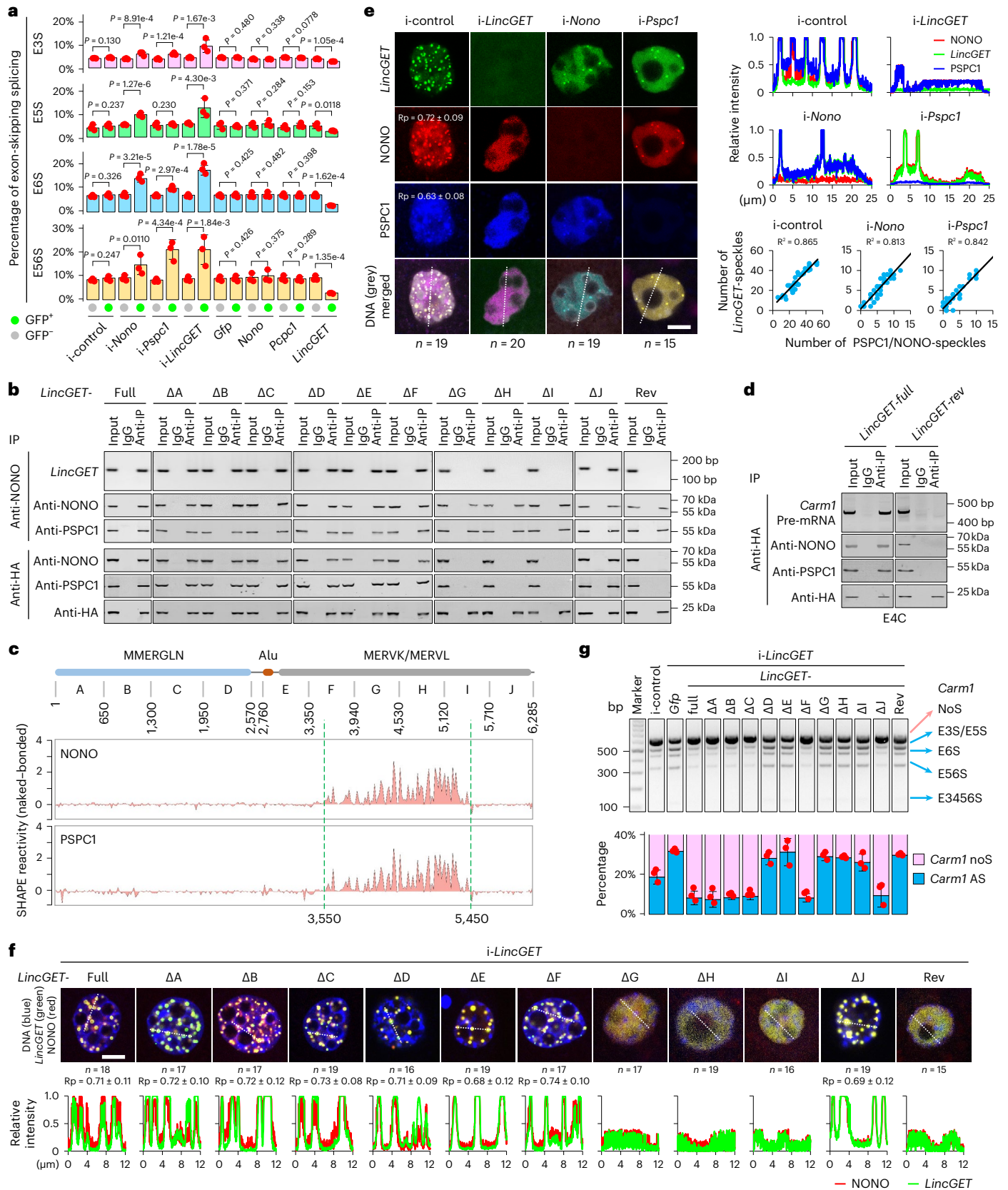
Supplementary Table 4). These results suggest that *LincGET* binding to the *Carm1* gene locus depends on both sequence complementarity and HNRNPU.

We found that HNRNPU ablation increased the ESS of *Carm1* pre-mRNAs (Fig. 3i and Extended Data Fig. 5e). Considering that the ESS of *Carm1* pre-mRNAs increased when the endogenic *LincGET* was replaced by deletion mutants without the HNRNPU-binding domain (ΔD and ΔE in Fig. 2g and Extended Data Fig. 4d), the correct localization of paraspeckles to the *Carm1* gene locus guided by the *LincGET*–HNRNPU complex is essential for inhibition of ESS of *Carm1* pre-mRNAs.

LincGET opens up *Carm1* gene locus by H3 arginine methylation

We reasoned that *LincGET* opens up a target gene locus by establishing H3 arginine methylation, given that we previously reported that *LincGET* physically binds to CARM1 and further increases the level of H3 arginine methylation[1], which can open chromatin and activate gene expression[35,36]. Based on the CARM1-binding motif and asymmetrical histone H3 arginine 17 dimethylation (H3R17me2a) motif generated from the ChIP–seq data[37], we found seven CARM1-binding or H3R17me2a sites in the *Carm1* gene locus, five of which located are in or near *LincGET*-binding peaks (Extended Data Fig. 5a). Moreover, we performed ChIP on H3R26me2 followed by qPCR after *LincGET* depletion or CARM1 inhibition. The results showed that all the *LincGET*-binding sites and all CARM1-binding or H3R17me2a sites are enriched for H3R26me2 modification (Extended Data Fig. 5a). In addition, we found that *LincGET* depletion or CARM1 inhibition resulted in deceased H3R26me2 modification in the sites in or near *LincGET*-binding peaks (Extended Data Fig. 5a). These results suggest that *LincGET* binds to the *Carm1* gene locus and further increases the level of H3 arginine methylation to open up the target gene locus.

Comparison between *LincGET* speckle and *Neat1* paraspeckle

The above results show that *LincGET*, rather than *Neat1*, functions in the organization of paraspeckles to their roles in alternative splicing regulation in mouse two-cell and four-cell embryos. However, in tissues and cell lines, it is *Neat1* that functions in the assembly of paraspeckles to regulate alternative splicing. We wanted to determine the potential similarities and differences between *LincGET* and *Neat1*.

First, we wondered whether *LincGET* contains similar structures as *Neat1*. We identified sequence similarity in a sequence of about 200 nucleotides in length (Supplementary Fig. 2a,b), and found similarities in the RNA second structure between *LincGET* and *Neat1* (Supplementary Fig. 2b–f, Supplementary Table 5 and Methods). These results suggest that *LincGET* and *Neat1* contain similar structures.

Next, we wondered whether the *LincGET* speckles are similar to *Neat1* paraspeckles. We co-stained *LincGET* and other paraspeckle-essential components, including SFPQ, FUS, TARDBP and SMARCA4. The results showed the co-localization of *LincGET* with SFPQ, FUS, TARDBP and SMARCA4 in mouse late two-cell and early four-cell embryos (Rp ≈ 0.7; Extended Data Fig. 6a), suggesting that *LincGET* speckles are like the *Neat1* paraspeckles in protein components.

As both *LincGET* and *Neat1* bind to paraspeckle components, we wondered whether *Neat1* is involved in *LincGET* speckles. The co-staining result showed that there are only a few *Neat1* speckles in each nucleus of early four-cell embryos but are all co-stained with *LincGET* and NONO (Extended Data Fig. 6b), which suggests that *Neat1* can be involved in *LincGET*-guided paraspeckles. Using absolute qPCR, we found hundreds of copies of *LincGET* but fewer than ten copies of *Neat1* in one mouse late two-cell or early four-cell embryo (Supplementary Table 6), which might explain why *Neat1* ablation has only a slight effect on the assembly of paraspeckle components in mouse early four-cell embryos (Extended Data Fig. 3d).

We also explored the structure of *LincGET* speckles. The results showed that the 3′ part of *LincGET*, NONO, PSPC1, SFPQ and FUS is located in the shell, whereas the 5′ part of *LincGET*, HNRNPU, TARDBP and SMARCA4 is located in the core of *LincGET* speckles (Extended Data Fig. 6c). As HNRNPU binds the middle part of *LincGET* (Fig. 3f), the middle part of *LincGET* locates in the core of *LincGET* speckles (Extended Data Fig. 6d). NONO, PSPC1, SFPQ and FUS locate in the core while TARDBP and SMARCA4 locate in the shell of *Neat1* paraspeckles[38], which suggests that *LincGET* speckles differ from *Neat1* paraspeckles in structure (Extended Data Fig. 6d).

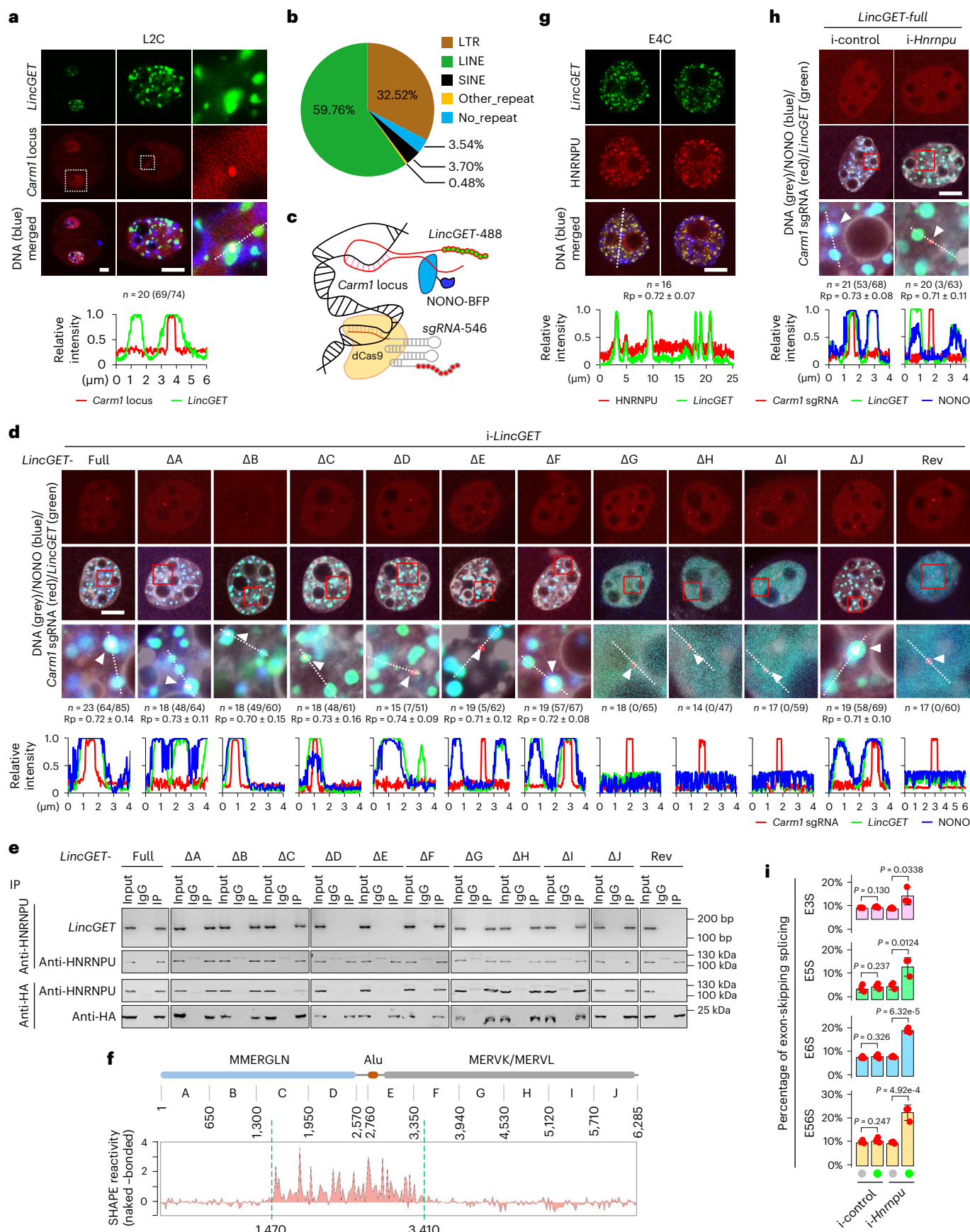### PCBP1 promotes ESS of *Carm1* pre-mRNAs

To further investigate the mechanism of the ESS of *Carm1* pre-mRNAs, we examined in detail the signature of splicing acceptor and splicing donor sequences around exons 2 to 7 of *Carm1* pre-mRNAs. Using RBPDB and CISBP-RNA databases, we found binding sites for FUS, NONO, RBMX, PUM2 and SRSF1/9 in splicing donor and acceptor elements around these exons (Fig. 4a). However, these binding sites are not specific to exons 3, 5 and 6, which are susceptible to be skipped during splicing. In addition, we noted that the splicing donor and acceptor elements flanking exons 3, 5 and 6, but not exons 2, 4 and 7, possess intronic C-rich motifs that could potentially be bound by PCBPs[39,40] such as PCBP1 and PCBP2 (Fig. 4a), which are involved in alternative splicing[41–44].

We found that PCBP1 was persistently expressed during mouse pre-implantation development (Extended Data Fig. 7a). The results showed that PCBP1 was diffusely distributed in the cytoplasm and nucleus, but the nuclear localization is higher at late two-cell and early four-cell stages while is lower at one-cell and early two-cell stages than at other stages (Extended Data Fig. 7a,b). These results reflect a potential role of PCBP1 in regulating alternative splicing in mouse two-cell to four-cell embryos.

To investigate whether PCBP1/2 regulates alternative splicing of *Carm1* pre-mRNAs by directly binding the exons susceptible to be skipped during splicing, we performed RNA electrophoretic mobility shift assays. The results showed that PCBP1/2 binds to splicing acceptor and donor sequence-flanked exons 3, 5 and 6, which contain C-rich motifs, but not exons 2, 4 and 7, which do not contain C-rich motifs (Fig. 4b). In addition, we found that the binding activity of PCBP1/2 was slightly higher when the C-rich composition increased in the splicing acceptor sequence 5′ to exon 3 of *Carm1* (SA-C26 in Fig. 4b). However, no PCBP1 binding was seen when the sequence was modified from C-rich to U-rich (SA-Mut in Fig. 4b). These results confirm that PCBP1

Fig. 3 | Interaction between *LincGET* and HNRNPU guides localization of paraspeckle to *Carm1* gene locus to inhibit ESS of *Carm1*. a, RNA-FISH combined with DNA-FISH assays in L2C. Scale bar, 10 μm. *n* = 20(69/74), which indicates 20 embryos were analyzed, 74 *Carm1* gene loci were detected and 69 of them were covered by *LincGET*. Bottom, relative fluorescence intensity. **b**, Pie chart showing the binding preference of *LincGET*. **c**, Model for co-localization of fluorescently labeled *LincGET*, sgRNA–dCas9 complex and NONO. **d**, Single nucleus of L2C injected with fluorescently labeled *LincGET* mutants, sgRNA–dCas9 complex and NONO. White triangles indicate sgRNA signals. Scale bar, 10 μm. The *n* values are as in **a**. Bottom, relative fluorescence intensity. **e**, Co-IP followed by RT–PCR and western blot in mEpiSCs. Three biological replicates were performed. **f**, SHAPE-MaP assays. **g**, Immunofluorescence combined with RNA-FISH assays in E4C. Scale bar, 10 μm. Bottom, relative fluorescence intensity. **h**, Immunofluorescence combined with RNA-FISH assays in L2C. Scale bar, 10 μm. White triangles indicate sgRNA signals. The *n* values are as in **a**. Bottom, relative fluorescence intensity. **i**, Combination charts showing changes of ESS of *Carm1* pre-mRNAs. Data are mean and s.e.m. One-tailed Student's *t*-tests were used for statistical analysis (*n* = 3 biological replicates). Rp values in **d**, **g** and **h** were calculated by Fiji/ImageJ.

prefers to bind C-rich motifs flanked by exons susceptible to be skipped in *Carm1* pre-mRNAs.

To test whether the binding of PCBP1 to intronic C-rich motifs is essential for ESS of *Carm1* pre-mRNAs, we cloned the *Carm1* exon 3 along with its flanked intronic C-rich motifs into a splice-reporter minigene[45] and then transfected it into MCF-7 cells with PCBP1 and PCBP2 depletion (Supplementary Table 3). Given that PCBP1 and PCBP2 have extensive functional overlap, we co-depleted *Pcbp1* and *Pcbp2*

Fig. 4 | PCBP1 promotes ESS of *Carm1* which is inhibited by *LincGET*-guided paraspeckles. a, Protein-binding site analysis of splicing acceptor or donor flanking exons 2 to 7 of *Carm1* pre-mRNA. The sequences for E3-Mut and E3-C26 are shown. The known binding motifs are shown in the table (bottom left). **b**, RNA electrophoretic mobility shift assay analysis. Three biological replicates were performed. **c**, Combination charts showing changes in ESS of *Carm1* pre-mRNAs. Data are mean and s.e.m. One-tailed Student's *t*-tests were used for statistical analysis (*n* = 3 biological replicates). **d**, Immunofluorescence combined with RNA-FISH assays in L2C. Scale bar, 10 µm. Bottom left, relative fluorescence intensity. Right, numbers of *LincGET* speckles and PCBP1 speckles calculated by Imaris. Two-tailed Student's *t*-tests were used for statistical analysis. **e**, Assays of

qPCR following sequential co-IP. Data are mean and s.e.m. One-tailed Student's *t*-tests were used for statistical analysis and *P* values are shown in Extended Data Fig. 7f (three biological replicates). N_P, sequential co-IP by anti-NONO antibody and then anti-PCBP1 antibody; P_N, sequential co-IP by anti-PCBP1 antibody and anti-NONO antibody. **f**, Single nucleus of L2C injected with fluorescently labeled *LincGET* mutants, sgRNAs–dCas9 complex and PCBP1. White triangles indicate sgRNA signals. Scale bar, 10 µm. *n* = 18(48/5/59) means that 18 embryos were analyzed, 59 *Carm1* gene loci were detected, and 48 and 5 of them were covered by *LincGET* speckles and PCBP1, respectively. Bottom, relative fluorescence intensity. Rp values in **d** and **f** were calculated by Fiji/ImageJ.

(*Pcbp1/2*). As a result, we found that PCBP1 and PCBP2 co-depletion significantly repressed *Carm1* exon 3 skipping splicing, and no ESS occurred when the splicing acceptor sequence 5′ to exon 3 of *Carm1* was modified from C-rich to U-rich, even in the control group (Extended Data Fig. 7c). These data suggest that PCBP1 promotes ESS of *Carm1* pre-mRNAs by binding to the intronic C-rich motifs close to the splicing acceptor or donor sequences. Moreover, we found that *Pcbp1* overexpression increased and *Pcbp1* depletion decreased the ESS of *Carm1* pre-mRNAs in mouse four-cell embryos (Fig. 4c and Extended Data Fig. 7d,e). Together, these results indicate that PCBP1/2 binds *Carm1* pre-mRNAs and promotes its ESS.

LincGET speckles prevent access of PCBP1 to *Carm1* gene locus

Pcbp1 overexpression increased the ESS of *Carm1* pre-mRNAs but can be reversed by overexpression of *LincGET* (Extended Data Fig. 7e), reflecting competition between *LincGET* and PCBP1. Given that some lncRNAs can inhibit target protein function by physical binding[46], we tested whether *LincGET* forms a complex with PCBP1. Based on immunostaining, we noted that both *LincGET* and PCBP1 formed speckles in the nucleus, but they were not co-localized and somewhat parallel to each other, both at two-cell and four-cell stages (Supplementary Fig. 3a), indicating that *LincGET* and PCBP1 are probably not in the same complex. In addition, we found that *LincGET* depletion did not affect the formation of PCBP1 speckles and vice versa (Fig. 4d and Supplementary Fig. 3b). These results indicate no interaction between PCBP1 and *LincGET*.

Splicing speckles have a crucial role, serving as storage and assembly sites for various pre-mRNA processing factors such as SRSF1 and the U2AF2 splicing factor[14,47]. Therefore, we asked whether *LincGET* or PCBP1 participate in splicing peckles. The staining results showed that PCBP1 co-localizes with SRSF1 in the nucleus of late two-cell and early four-cell embryos (Rp ≈ 0.6; Supplementary Fig. 3c), and the co-IP results revealed that PCBP1 forms complexes with SRSF1 in early four-cell embryos (Supplementary Fig. 3d), suggesting that PCBP1 is involved in splicing speckles. Additionally, *LincGET* does not co-localize with U2AF2 or SRSF1 (Supplementary Fig. 3e), and SRSF1 ablation did not affect the formation of *LincGET* speckles and vice versa

(Supplementary Fig. 3f). These results suggest that PCBP1 participates in splicing speckles while *LincGET* is involved in the paraspeckles.

Considering that both PCBP1 and *LincGET* can bind to *Carm1* pre-mRNAs, we surmised that *LincGET*-guided paraspeckles affect the binding of PCBP1 to *Carm1* pre-mRNAs. To test our hypothesis, we performed sequential co-IP by anti-NONO antibody and then anti-PCBP1 antibody, as well as by anti-PCBP1 antibody and anti-NONO antibody (Supplementary Fig. 3g). The results showed that about 80% of *Carm1* pre-mRNA was captured by NONO in the control group, and about 45% and 85% of *Carm1* pre-mRNA was captured by PCBP1 upon PCBP1 overexpressing or upon *LincGET* depletion, respectively (Fig. 4e and Extended Data Fig. 7f). These results indicate that the affinity of *Carm1* pre-mRNA is higher for *LincGET*-guided paraspeckles than for PCBP1 in mouse four-cell embryos. We also tested the localization of PCBP1 when the localization of paraspeckles was disturbed, by replacing endogenic *LincGET* with *LincGET*-ΔD/ΔE mutants, or when paraspeckles were destroyed, by replacing endogenic *LincGET* with *LincGET*-ΔG/ΔH/ΔI mutants. We found that *LincGET* paraspeckles assembled around *Carm1* gene loci while the PCBP1 speckles were out of the *Carm1* gene loci when the full-length *LincGET* was injected (Fig. 4f and Supplementary Fig. 4a,b). However, the PCBP1 speckles assembled around *Carm1* loci both when the localization of paraspeckles was disturbed and when paraspeckles were destroyed (Fig. 4f and Supplementary Fig. 4a,c). These results indicate that *LincGET*-guided paraspeckles prevent access of PCBP1 to the *Carm1* gene locus to inhibit the ESS of *Carm1* pre-mRNAs.

LincGET speckles occupancy links to *Carm1* ESS heterogeneity

Given that the above results indicated that the competitive occupancy of *LincGET* speckles and PCBP1 regulates skipping splicing of exons 3 to 6 of *Carm1* pre-mRNAs, we wondered whether the occupancy of *LincGET* speckles and PCBP1 around the *Carm1* gene locus is heterogenous in mouse two-cell and four-cell embryos and whether the heterogenous occupancy is associated with the heterogeneity of exon-skipping events on exon 3 to 6 of *Carm1* pre-mRNAs. Interestingly, the immunofluorescence combined with RNA-FISH and DNA-FISH results supported the heterogenous occupancy of *LincGET* speckles and PCBP1 around

Fig. 5 | Alternative splicing contributes to CARM1 heterogeneity.
a–**c** Illustration of the heterogenous analysis (**a**) using immunofluorescence combined with RNA-FISH and DNA-FISH (**b**) and single-cell SPAR assay (**c**). pB and npB denote the blastomeres attached (pB) or not attached (npB) by the second polar body (PB2) in two-cell embryos; nB and fB denote the blastomeres near (nB) or farthest (fB) from PB2 in tetrahedral four-cell embryos. **b**, Histogram showing the heterogenous occupancy of *LincGET* speckles and PCBP1 around the *Carm1* gene loci according to the spatial position relative to PB2 in L2C and E4C. χ^2 tests are used for statistical analysis with df = 2; *n* = 60 L2C or E4C examined over four biological replicates. **c**, Dot plots showing the heterogeneity of ESS of *Carm1* pre-mRNAs according to the spatial position relative to PB2 in L2C and E4C. Two-tailed Student's *t*-tests are used for statistical analysis. *n* = 60 L2C or E4C examined over four biological replicates. **d**, Illustration of the correlation between heterogeneous occupancy of *LincGET*

speckles around the *Carm1* gene loci and the heterogeneity of ESS of *Carm1* pre-mRNAs. **e**, Single-cell qPCR assays in E4C. Two-tailed Student's *t*-tests were used for statistical analysis. **f**, ESS events on exons 3 to 6 of *Carm1* pre-mRNAs and the corresponding protein structures. Primer sites and antibody-recognizing sites are shown. IF, immunfluorescence; WB, western blot. **g**, Western blot assays in E4C. Tubulin is used as a control. Data are mean and s.e.m. One-tailed Student's *t*-tests were used for statistical analysis (left, *n* = 3; right, *n* = 4 biological replicates). **h**, Examples of three-dimensional (3D) reconstruction analysis. Scale bar, 50 mm. TE, trophectoderm; ICM, inner cell mass. **i**, Analysis of the distribution of progeny of injected blastomere at the blastocyst stage based on 3D reconstruction. Data are mean ± s.e.m. Two-tailed Student's *t*-tests were used for statistical analysis and *P* values are shown in Extended Data Fig. 10d. Key to table headings are shown in Supplementary Table 8.
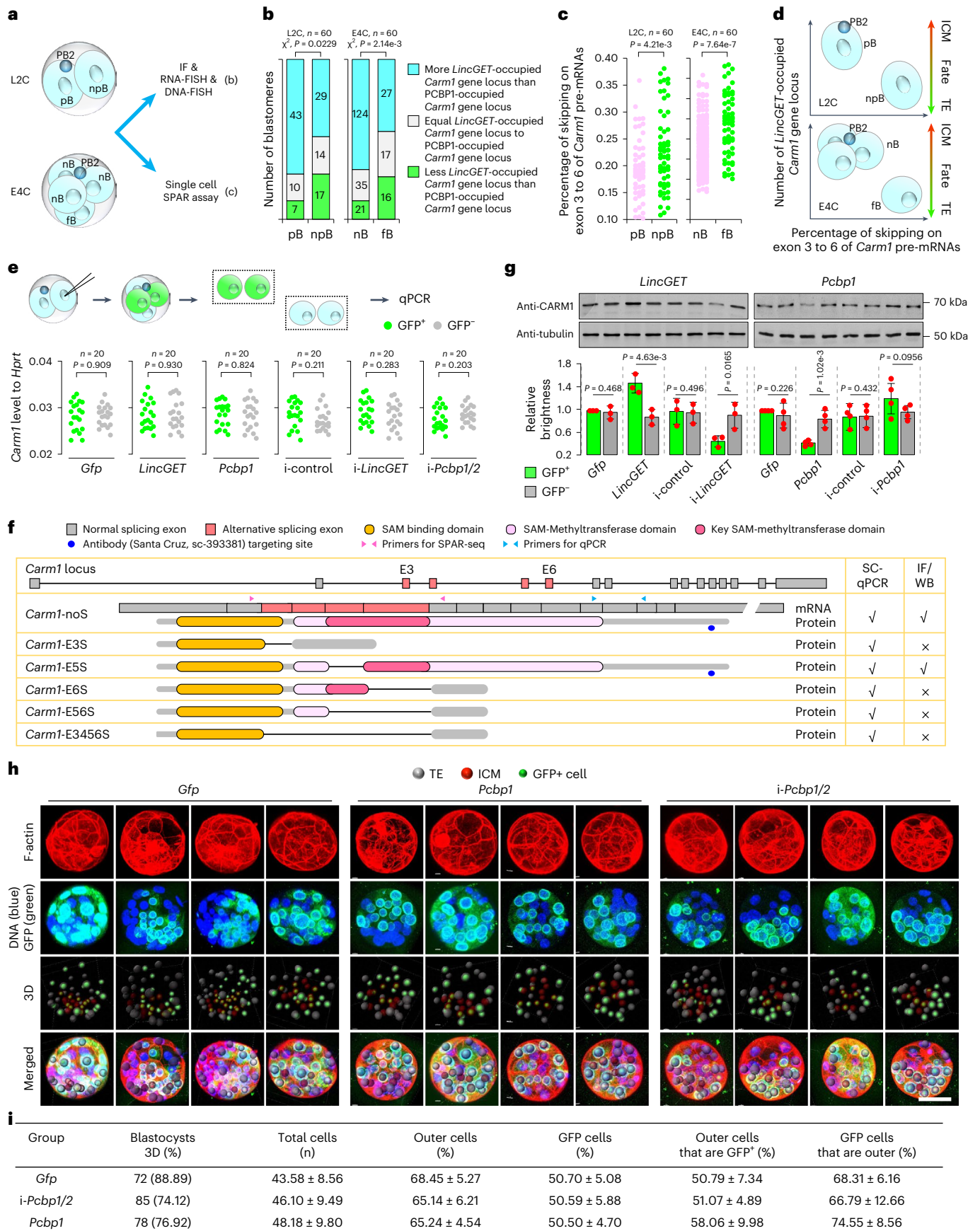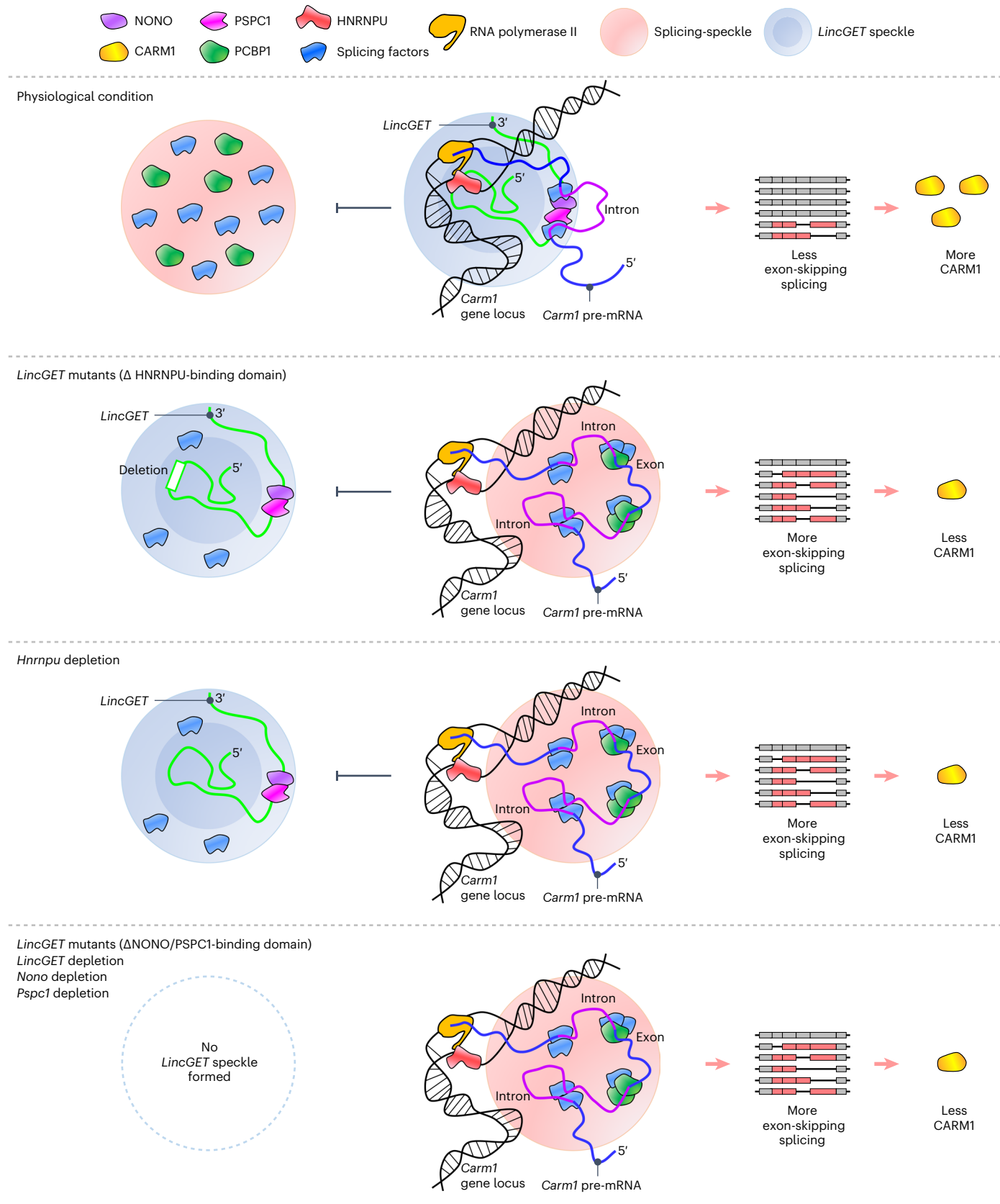
Fig. 6 | Model of *LincGET*-guided paraspeckles and PCBP1 on ESS regulation of *Carm1* pre-mRNAs. In physiological conditions (first line), *LincGET* speckles assemble around the *Carm1* gene locus and inhibit the access of splicing speckles, leading to less ESS of *Carm1* pre-mRNAs and more CARM1 protein. When *LincGET* loses the HNRNPU-binding domain (second line) or without HNRNPU (third line), *LincGET* speckles assemble but cannot localize to the *Carm1* gene locus, while splicing speckles assemble around the *Carm1* gene locus, leading to more ESS of *Carm1* pre-mRNAs and less CARM1 protein. When *LincGET* loses the NONO/PSPC1-binding domain, or without *LincGET*, *Nono* or *Pspc1* (fourth line), *LincGET* speckles cannot assemble, while splicing speckles assemble around the *Carm1* gene locus, leading to more ESS of *Carm1* pre-mRNAs and less CARM1 protein.

the *Carm1* gene loci in mouse late two-cell and early four-cell embryos (Extended Data Fig. 8a–c). Simultaneous detection of the heterogenous occupancy and the heterogeneity of *Carm1* ESS events in single blastomeres is very difficult because RNA degradation is severe after immunofluorescence combined with RNA-FISH and DNA-FISH and there are no instruments capable of microdissection in three dimensions.

We then used the spatial position relative to the second polar body (PB2) as a link to study the relationship between the heterogenous occupancy and the heterogeneity of *Carm1* ESS events for two reasons. Firstly, the spatial position of blastomeres in the two-cell to four-cell stage can be recorded by their positions relative to PB2. Blastomeres in two-cell embryos can be recorded as blastomeres that are attached by PB2 (pB) and not attached by PB2 (npB); blastomeres in tetrahedral four-cell embryos can be recorded as blastomeres that are near PB2 (nB) and far from PB2 (fB) (Fig. 5a). Secondly, pB and npB as well as nB and fB have a cell fate bias but not a random fate[24,48]. As a result, we found that the *Carm1* gene loci are more likely to be occupied by *LincGET* speckles, and the percentage of exon-skipping events on exon 3 to 6 of *Carm1* pre-mRNAs is lower in pB than in npB in late two-cell embryos, and lower in nB than in fB in tetrahedral late four-cell embryos (Fig. 5b,c, Extended Data Fig. 9a–c and Supplementary Table 7). These results demonstrate that the more *LincGET* speckles there are around the *Carm1* gene loci, the fewer ESS events there are on exon 3 to 6 of *Carm1* pre-mRNAs (Fig. 5d).

Alternative splicing contributes to CARM1 heterogeneity

Given that ESS can lead to decreased protein levels[49], we wondered whether ESS contributes to CARM1 protein heterogeneity in mouse early embryos. We found that neither overexpression nor depletion of *Nono*, *Pspc1*, *LincGET* or *Pcbp1* affects *Carm1* mRNA levels (Fig. 5e and Extended Data Fig. 10a), reflecting that neither *LincGET*-paraspeckles nor PCBP1 are involved in transcriptional regulation of *Carm1*. However, we found that depletion of *Nono*, *Pspc1* and *LincGET* and overexpression of *Pcbp1* decreased while overexpression of *LincGET* increased the CARM1 protein level (Fig. 5f,g, Extended Data Fig. 10b). These results were consistent with the previous observation that knockdown of paraspeckle components (NONO) decreased CARM1 protein levels in mouse early embryos[3]. To further explore whether the ESS is correlated with CARM1 protein level, single blastomeres separated from late two-cell and early four-cell embryos were used for dot plotting for CARM1 and qPCR for the ESS isoform *Carm1_E56S* and the total expression level of *Carm1*. The results showed that the ESS level but not the expression level of *Carm1* correlates with CARM1 protein levels in mouse two-cell to four-cell embryos (Extended Data Fig. 10c). Together, our findings indicate that both *LincGET* speckles and PCBP1 regulate CARM1 protein levels through the regulation of ESS.

As PCBP1 promotes ESS of *Carm1* pre-mRNAs, which contrasts with the role of *LincGET*, we wondered whether PCBP1 overexpression biases first cell fate toward the trophectoderm as opposed to *LincGET*, which biases blastomeres toward inner cell mass[1]. The total number of cells and the percentage of GFP+ cells in blastocysts were similar among *Pcbp1* overexpression, *Pcbp1/2* ablation and the control groups (Fig. 5h,i, Extended Data Fig. 10d and Supplementary Table 8), indicating that *Pcbp1* overexpression or depletion does not affect the overall mouse pre-implantation development. However, the percentage of outer cells that are GFP+ was significantly higher in the *Pcbp1* overexpression group (58.06 ± 9.98%) than in the control group (50.79 ± 7.34%) and *Pcbp1* ablation group (51.07 ± 4.89%), and the percentage of GFP+ cells that were outer was also significantly higher in the *Pcbp1* overexpression group (74.55 ± 8.56%) than in the control group (68.31 ± 6.16%) and *Pcbp1* ablation group (66.79 ± 12.66%) (Fig. 5h,i, Extended Data Fig. 10d and Supplementary Table 8). These results reflect that overexpression of PCBP1 in one of the two-cell blastomeres leads to decreased CARM1 protein levels and biases its progeny cells toward a trophectoderm fate.

Discussion

CARM1 heterogeneity is the core factor that biases the first cell fate in mice, yet the mechanism by which CARM1 heterogeneity is established is far from understood. Here, we found that *LincGET* contributes to CARM1 heterogeneity at the post-transcriptional level by tethering paraspeckle components to the *Carm1* gene locus to inhibit the ESS of *Carm1* pre-mRNAs (Fig. 6). In light of our earlier work[1], our findings reflect that *LincGET* both helps to correctly splice *Carm1* mRNA and, after CARM1 is translated, *LincGET* binds CARM1 to regulate epigenetic modifications and cell fate bias as early as the two-cell stage in mice. Moreover, we found that PCBP1 promotes the ESS of *Carm1* pre-mRNAs and biases the blastomere towards a trophectoderm fate. This study demonstrates that alternative splicing contributes to the first cell fate bias in mouse pre-implantation embryos.

There are other non-membrane-bound subnuclear domains that function in RNA processing, such as the nuclear poly(A) domains (NPADs) that work as the hub for newly synthesized mRNA in growing mouse oocytes[50]. In addition to nuclear poly(A)-binding protein 1 (PABPN1), NPADs also involve alternative splicing factors such as SRSF2 (also known as SC35)[50]. Although *LincGET* is not expressed in metaphase II (MII) oocytes[2], it is a worthwhile topic in the future to explore whether paraspeckles and/or splicing speckles exist and function in the growing oocytes when transcription is still active. If this is the case, whether or not the protein components of the NPAD, such as PABPN1 and SRSF2, co-localize with paraspeckles and/or splicing speckles would require further study.

Online content

Any methods, additional references, Nature Portfolio reporting summaries, source data, extended data, supplementary information, acknowledgements, peer review information; details of author contributions and competing interests; and statements of data and code availability are available at https://doi.org/10.1038/s41594-024-01292-9.

References

1. Wang, J. et al. Asymmetric expression of LincGET biases cell fate in two-cell mouse embryos. *Cell* **175**, 1887–1901.e18 (2018).
2. Wang, J. et al. A novel long intergenic noncoding RNA indispensable for the cleavage of mouse two-cell embryos. *EMBO Rep.* **17**, 1452–1470 (2016).
3. Hupalowska, A. et al. CARM1 and paraspeckles regulate pre-implantation mouse embryo development. *Cell* **175**, 1902–1916.e13 (2018).
4. Ule, J. & Blencowe, B. J. Alternative splicing regulatory networks: functions, mechanisms, and evolution. *Mol. Cell* **76**, 329–345 (2019).
5. Kalsotra, A. & Cooper, T. A. Functional consequences of developmentally regulated alternative splicing. *Nat. Rev. Genet.* **12**, 715–729 (2011).
6. Gabut, M. et al. An alternative splicing switch regulates embryonic stem cell pluripotency and reprogramming. *Cell* **147**, 132–146 (2011).
7. Baralle, F. E. & Giudice, J. Alternative splicing as a regulator of development and tissue identity. *Nat. Rev. Mol. Cell Biol.* **18**, 437–451 (2017).
8. Wu, J. Q. et al. Dynamic transcriptomes during neural differentiation of human embryonic stem cells revealed by short, long, and paired-end sequencing. *Proc. Natl Acad. Sci. USA* **107**, 5254–5259 (2010).
9. Salomonis, N. et al. Alternative splicing regulates mouse embryonic stem cell pluripotency and differentiation. *Proc. Natl Acad. Sci. USA* **107**, 10514–10519 (2010).
10. Tang, F. et al. Tracing the derivation of embryonic stem cells from the inner cell mass by single-cell RNA-seq analysis. *Cell Stem Cell* **6**, 468–478 (2010).

11. Warzecha, C. C. et al. An ESRP-regulated splicing programme is abrogated during the epithelial–mesenchymal transition. *EMBO J.* **29**, 3286–3300 (2010).

12. Valacca, C. et al. Sam68 regulates EMT through alternative splicing-activated nonsense-mediated mRNA decay of the SF2/ASF proto-oncogene. *J. Cell Biol.* **191**, 87–99 (2010).

13. Brown, R. L. et al. CD44 splice isoform switching in human and mouse epithelium is essential for epithelial–mesenchymal transition and breast cancer progression. *J. Clin. Invest.* **121**, 1064–1074 (2011).

14. Matera, A. G., Terns, R. M. & Terns, M. P. Non-coding RNAs: lessons from the small nuclear and small nucleolar RNAs. *Nat. Rev. Mol. Cell Biol.* **8**, 209–220 (2007).

15. Fox, A. H., Bond, C. S. & Lamond, A. I. P54nrb forms a heterodimer with PSP1 that localizes to paraspeckles in an RNA-dependent manner. *Mol. Biol. Cell* **16**, 5304–5315 (2005).

16. Prasanth, K. V. et al. Regulating gene expression through RNA nuclear retention. *Cell* **123**, 249–263 (2005).

17. Batista, P. J. & Chang, H. Y. Long noncoding RNAs: cellular address codes in development and disease. *Cell* **152**, 1298–1307 (2013).

18. Sasaki, Y. T., Ideue, T., Sano, M., Mituyama, T. & Hirose, T. MENε/β noncoding RNAs are essential for structural integrity of nuclear paraspeckles. *Proc. Natl Acad. Sci. USA* **106**, 2525–2530 (2009).

19. Mao, Y. S., Sunwoo, H., Zhang, B. & Spector, D. L. Direct visualization of the co-transcriptional assembly of a nuclear body by noncoding RNAs. *Nat. Cell Biol.* **13**, 95–101 (2011).

20. Ko, M. S. Zygotic genome activation revisited: looking through the expression and function of Zscan4. *Curr. Top. Dev. Biol.* **120**, 103–124 (2016).

21. Liu, X. et al. Reprogramming roadmap reveals route to human induced trophoblast stem cells. *Nature* **586**, 101–107 (2020).

22. Fan, X. et al. Single-cell RNA-seq analysis of mouse preimplantation embryos by third-generation sequencing. *PLoS Biol.* **18**, e3001017 (2020).

23. Qiao, Y. et al. High-resolution annotation of the mouse preimplantation embryo transcriptome using long-read sequencing. *Nat. Commun.* **11**, 2653 (2020).

24. Torres-Padilla, M. E., Parfitt, D. E., Kouzarides, T. & Zernicka-Goetz, M. Histone arginine methylation regulates pluripotency in the early mouse embryo. *Nature* **445**, 214–218 (2007).

25. Han, H. et al. Multilayered control of alternative splicing regulatory networks by transcription factors. *Mol. Cell* **65**, 539–553.e7 (2017).

26. Peabody, D. S. The RNA binding site of bacteriophage MS2 coat protein. *EMBO J.* **12**, 595–600 (1993).

27. Smola, M. J. et al. SHAPE reveals transcript-wide interactions, complex structural domains, and protein interactions across the Xist lncRNA in living cells. *Proc. Natl Acad. Sci. USA* **113**, 10322–10327 (2016).

28. Guallar, D. et al. RNA-dependent chromatin targeting of TET2 for endogenous retrovirus control in pluripotent stem cells. *Nat. Genet.* **50**, 443–451 (2018).

29. Kornblihtt, A. R. Shortcuts to the end. *Nat. Struct. Mol. Biol.* **11**, 1156–1157 (2004).

30. Azzalin, C. M., Reichenbach, P., Khoriauli, L., Giulotto, E. & Lingner, J. Telomeric repeat containing RNA and RNA surveillance factors at mammalian chromosome ends. *Science* **318**, 798–801 (2007).

31. He, S., Zhang, H., Liu, H. & Zhu, H. LongTarget: a tool to predict lncRNA DNA-binding motifs and binding sites via Hoogsteen base-pairing analysis. *Bioinformatics* **31**, 178–186 (2015).

32. Wang, H. et al. CRISPR-mediated live imaging of genome editing and transcription. *Science* **365**, 1301–1305 (2019).

33. Hendrickson, D. G., Kelley, D. R., Tenen, D., Bernstein, B. & Rinn, J. L. Widespread RNA binding by chromatin-associated proteins. *Genome Biol.* **17**, 28 (2016).

34. Fackelmayer, F. O., Dahm, K., Renz, A., Ramsperger, U. & Richter, A. Nucleic-acid-binding properties of hnRNP-U/SAF-A, a nuclear-matrix protein which binds DNA and RNA in vivo and in vitro. *Eur. J. Biochem.* **221**, 749–757 (1994).

35. Puri, P. et al. Elevated protein kinase A activity in stomach mesenchyme disrupts mesenchymal–epithelial crosstalk and induces preneoplasia. *Cell Mol. Gastroenterol. Hepatol.* **14**, 643–668.e1 (2022).

36. Litt, M., Qiu, Y. & Huang, S. Histone arginine methylations: their roles in chromatin dynamics and transcriptional regulation. *Biosci. Rep.* **29**, 131–141 (2009).

37. Cheng, D. et al. CARM1 methylates MED12 to regulate its RNA-binding ability. *Life Sci. Alliance* **1**, e201800117 (2018).

38. West, J. A. et al. Structural, super-resolution microscopy analysis of paraspeckle nuclear body organization. *J. Cell Biol.* **214**, 817–830 (2016).

39. Huang, S. et al. PCBP1 regulates the transcription and alternative splicing of metastasis-related genes and pathways in hepatocellular carcinoma. *Sci. Rep.* **11**, 23356 (2021).

40. O'Grady, T. et al. Genome-wide transcript structure resolution reveals abundant alternate isoform usage from murine gammaherpesvirus 68. *Cell Rep.* **27**, 3988–4002.e5 (2019).

41. Ji, X., Humenik, J., Yang, D. & Liebhaber, S. A. PolyC-binding proteins enhance expression of the CDK2 cell cycle regulatory protein via alternative splicing. *Nucleic Acids Res* **46**, 2030–2044 (2017).

42. Tripathi, V. et al. Direct regulation of alternative splicing by SMAD3 through PCBP1 is essential to the tumor-promoting role of TGF-β. *Mol. Cell* **64**, 549–564 (2016).

43. Romig, H., Fackelmayer, F. O., Renz, A., Ramsperger, U. & Richter, A. Characterization of SAF-A, a novel nuclear DNA binding protein from HeLa cells with high affinity for nuclear matrix/scaffold attachment DNA elements. *EMBO J.* **11**, 3431–3440 (1992).

44. Meng, Q. et al. Signaling-dependent and coordinated regulation of transcription, splicing, and translation resides in a single coregulator, PCBP1. *Proc. Natl Acad. Sci. USA* **104**, 5866–5871 (2007).

45. Kishore, S., Khanna, A. & Stamm, S. Rapid generation of splicing reporters with pSpliceExpress. *Gene* **427**, 104–110 (2008).

46. Kino, T., Hurt, D. E., Ichijo, T., Nader, N. & Chrousos, G. P. Noncoding RNA gas5 is a growth arrest- and starvation-associated repressor of the glucocorticoid receptor. *Sci. Signal* **3**, ra8 (2010).

47. Spector, D. L. & Lamond, A. I. Nuclear speckles. *Cold Spring Harb. Perspect. Biol.* **3**, a000646 (2011).

48. Jin, H. et al. The second polar body contributes to the fate asymmetry in the mouse embryo. *Natl Sci. Rev.* **9**, nwac003 (2022).

49. Sud, R., Geller, E. T. & Schellenberg, G. D. Antisense-mediated exon skipping decreases tau protein expression: a potential therapy for tauopathies. *Mol. Ther. Nucleic Acids* **3**, e180 (2014).

50. Dai, X. X. et al. PABPN1 functions as a hub in the assembly of nuclear poly(A) domains that are essential for mouse oocyte development. *Sci. Adv.* **8**, eabn9016 (2022).

51. Wang, L. et al. A novel lncRNA *Discn* fine-tunes replication protein A (RPA) availability to promote genomic stability. *Nat. Commun.* **12**, 5572 (2021).

52. Huyghe, A. et al. Comparative roadmaps of reprogramming and oncogenic transformation identify Bcl11b and Atoh8 as broad regulators of cellular plasticity. *Nat. Cell Biol.* **24**, 1350–1363 (2022).

53. Shi, Y. et al. Critical role of Znhit1 for postnatal heart function and vacuolar cardiomyopathy. *JCI Insight* **7**, e148752 (2022).

54. Acevedo-Acevedo, S. et al. LKB1 acts as a critical brake for the glucagon-mediated fasting response. *Hepatol. Commun.* **6**, 1949–1961 (2022).

Methods

Ethical statements

All the mouse procedures were carried out in compliance with the guidelines of the Animal Care and Use Committee of the Institute of Zoology, Chinese Academy of Sciences, and the Animal Care and Use Committee of the Northeast Agricultural University.

Antibodies

The following antibodies were used for immunoblotting, immunostaining and/or immunoprecipitation: mouse monoclonal (G-2) anti-CARM1 (Santa Cruz, sc-393381), chicken polyclonal anti-GFP (Abcam, ab13970), rat monoclonal (YL1/2) anti-Tubulin (Abcam, ab6160), goat polyclonal anti-PCBP1 (Abcam, ab109577), rat monoclonal (EPR14859(2)) anti-PCBP2 (Abcam, ab200835), rat monoclonal (EPR8239) anti-SRSF1 (Abcam, ab129108), rabbit polyclonal anti-HA (Abcam, ab9110), rabbit polyclonal anti-NONO (Abcam, ab70335), rabbit polyclonal anti-PSPC1 (Abcam, ab104238), rabbit polyclonal anti-HNRNPU (Abcam, ab20666), rabbit polyclonal anti-U2AF2 (Abcam, ab37530), rabbit polyclonal anti-H3R26me2 (Abcam, ab127095), FITC-conjugated donkey anti-Chicken IgY polyclonal secondary antibody (Invitrogen, SA1-72000), Alexa Fluor Plus 555-conjugated goat anti-Mouse IgG polyclonal secondary antibody (Invitrogen, A32727), Alexa Fluor Plus 555-conjugated donkey anti-Goat IgG polyclonal secondary antibody (Invitrogen, A32816), Alexa Fluor Plus 555-conjugated donkey anti-Rabbit IgG polyclonal secondary antibody (Invitrogen, A32794), Alexa Fluor Plus 555-conjugated donkey anti-Rat IgG polyclonal secondary antibody (Invitrogen, A48270), Alexa Fluor 488-conjugated rabbit anti-Rat IgG polyclonal secondary antibody (Invitrogen, A-21210), HRP-conjugated goat anti-Rabbit IgG polyclonal secondary antibody (Invitrogen, A27036), HRP-conjugated mouse anti-Goat IgG polyclonal secondary antibody (Invitrogen, 31400) and HRP-conjugated goat anti-Rat IgG polyclonal secondary antibody (Invitrogen, 31470).

Mouse embryo collection

The CD1 (ICR) mice were purchased from Vital River company. All mice used for experiments were 7–8 weeks old. All mice were housed in the animal care facilities under specific pathogen-free conditions, with a 12 h dark–light cycle, ambient temperature ranging from 21 °C to 26 °C and a humidity level of 50% to 60%. To obtain pre-implantation embryos, female mice were injected with 10 U of pregnant mare serum gonadotropin (PMSG, Prospec, HOR-272) and 10 U of human chorionic gonadotropin (hCG, Prospec, HOR-250) at 46–48 h intervals and then crossed with 7–8-week-old CD1 (ICR) male mice. Embryos were collected at the following times post hCG injection: early one-cell stage (phCG 19 h), late one-cell stage (phCG 30 h), early two-cell stage (phCG 39 h), late two-cell stage (phCG 48 h), early four-cell stage (phCG 54 h), late four-cell stage (phCG 62 h), early eight-cell stage (phCG 68 h), late eight-cell stage (phCG 74 h), 16-cell stage (phCG 80 h), 32-cell stage (phCG 90 h), early blastocyst stage (phCG 98 h) and late blastocyst stage (phCG 114 h).

Culture cells

mEpiSCs were established in Q. Zhou's lab in the State Key Laboratory of Stem Cell and Reproductive Biology, Institute of Zoology, Chinese Academy of Sciences, and cultured in a fibronectin-coated dish in N2B27 medium plus 12 ng ml^{-1} bFGF (R&D, 233-FB-001MG/CF) and 10 ng ml^{-1} activin A (R&D, 338-AC-01M) at 37 °C in a 5% CO$_2$ incubator. The culture medium was changed every day, and the mEpiSCs were passaged every 2–3 days and then digested to single cells by 0.05% trypsin/EDTA (GIBCO, 25300062). The MCF-7 cells were purchased from ATCC (ATCC, HTB-22). MCF-7 cells were cultured in DMEM/F-12 (1:1) medium supplemented with 10% FBS at 37 °C in a 5% CO$_2$ incubator. For cell transfection, the cells were passaged and seeded at a density of 1–1.5 × 10^4 cells per cm^2. After 2 days (60–70% confluence), plasmid DNA (MS2-LincGET and MS2P-HA for mEpiSCs; PCBP-shRNA for

MCF-7 cells) was transferred into cells using Lipofectamine 3000 transfection reagent (GIBCO, L3000015) according to the manufacturer's instructions. mEpiSCs and MCF-7 cells were collected for further analysis 36 and 72 h after transfection, respectively.

RNA extraction, reverse transcription and qPCR

RNA was extracted using the RNeasy Mini Kit (QIAGEN, 74104), and the RNase-Free DNase Set (QIAGEN, 79254) was used to prevent DNA contamination. Reverse transcription was performed using a High-Capacity cDNA Reverse Transcription Kit (ABI, 4368814). SYBR-qPCR was performed using a Power SYBR Green PCR Master Mix (ABI, 4367659). TM-qPCR was performed using TaqMan Universal Master Mix II (Life, 4440048). All kits were used following the manufacturers' guidelines.

Construction of plasmid vectors

To create Alexa Fluor 488-labeled RNA probes for LincGET RNA-FISH, the specific LincGET region (2,574–2,763) was amplified using the 2× Vazyme Lamp Master Mix (Dye Plus) (Vazyme, P312). Primers are shown in Supplementary Table 3. These sequences were sub-cloned into the plasmid pEASY-T3 cloning vector (TransGen, CT301-02), which contains the T7 promoter. For co-IP experiments, the MS2 coat protein (MS2P), MS2-labeled LincGET and HA-labeled MS2P were cloned into the PB533A vector (SBI, PB533A-2) digested with EcoRI or SalI, respectively.

For in vitro transcription, the GFP-KASH sequence with T7 promoter was synthesized by BGI company and sub-cloned into the pUC57 vector; LincGET mutants were generated by PCR, 5'-phosphorylation and ligation; plasmid containing NONO-BFP or NONO-mCherry with T7 promoter was purchased from YouBio company (YouBio, L3774 and L2772).

For coding potential analysis for exon-skipping variants of Carm1, Carm1 (NM_021531) cDNA for non-skipping splicing (noS) and Carm1 (NM_153141) cDNA for the E15S variant were purchased from YouBio company (YouBio, G156971 and G156972). The EF1α promoter from Addgene plasmid no. 61422, Carm1 cDNA and bGH poly(A) signal element from Addgene plasmid no. 61422 were sub-cloned into plasmid pEGFP-C1, purchased from YouBio company (YouBio, VT1118), using NEBuilder HiFi DNA Assembly Cloning Kit (NEB, E5520S). Carm1 mutants of E3S, E5S, E6S, E56S, E3456S and E11S were generated by PCR, 5'-phosphorylation and ligation.

For short hairpin RNA (shRNA) expression, primers containing sense-loop–antisense structure (Supplementary Table 3) were synthesized and annealed to generate double-strand oligonucleotides with a re-annealing process: 95 °C for 10 min; 95–85 °C ramping at −2 °C s^{-1}; 85–25 °C at −0.25 °C s^{-1}; and 25 °C hold for 1 min. Then the double-strand oligonucleotides were sub-cloned into the pLL3.7 vector (Addgene, 11795).

For protein expression and purification, the NONO, PCBP1 or PCBP2 sequence followed by a 14 amino acid linker sequence 'GAPG-SAGSAAGGSG' and mCherry or GFP was cloned into a modified version of a T7 pET expression vector (YouBio) containing a 5' MBP tag and a 3' 6×His tag.

For minigene analysis of ESS of Carm1 pre-mRNAs, wild-type Carm1 exon 3 flanked by a 539 bp 5' splicing acceptor sequence and 258 bp 3' splicing donor sequence, wild-type Carm1 exon 5 flanked by a 531 bp 5' splicing acceptor sequence and 506 bp 3' splicing donor sequence, and wild-type Carm1 exon 6 flanked by a 550 bp 5' splicing acceptor sequence and 418 bp 3' splicing donor sequence were amplified by PCR with the primers listed in Supplementary Table 3 using Q5U Hot Start High-Fidelity DNA Polymerase (NEB, M0515) and then cloned into the KpnI-digested pSpliceExpress (Addgene, 32485) splicing minigene plasmid[45] using the In-Fusion HD Cloning Kit (Clontech, 639636) following the manufacturers' guidelines. Plasmids for E3-C26 and E3-Mut were generated by PCR with primers containing mutations using Q5U Hot Start High-Fidelity DNA Polymerase (NEB, M0515), phosphorylation

using T4 polynucleotide kinase (NEB, M0201L) and ligation using T4 DNA ligase (NEB, M0202L).

Micro-injection

Mouse embryos at the one-cell stage were collected and microinjected with about 1–2 pL RNA at 150 ng μl⁻¹ concentration or plasmid at 10 ng μl⁻¹ concentration into the pronucleus at phCG 25 h, using an Eppendorf micromanipulator on a Nikon inverted microscope. The *LincGET* and mRNAs for NONO and PCBP1 were in vitro transcribed with HiScribe T7 ARCA pre-mRNAs Kit (with tailing) (NEB, E2060), while the single-guide RNAs (sgRNAs) were in vitro transcribed with HiScribe T7 Quick High Yield RNA Synthesis Kit (NEB, E2050) following the manufacturers' guidelines. DNA templates with T7 promoter were amplified using the 2× Vazyme Lamp Master Mix (Dye Plus) (Vazyme, P312). Primers are shown in Supplementary Table 3. The fluorescently labeled *LincGET* or sgRNAs were generated by Poly(U) Polymerase (NEB, M0337S) with modified nucleotide 5-(3-aminoallyl)-UTP (Ambion, AM8437) and then labeled with Alexa Fluor 488 NHS Ester (Succinimidyl Ester) (Invitrogen, A20000) or Alexa Fluor 546 NHS Ester (Succinimidyl Ester) (Invitrogen, A20002) following the manufacturers' guidelines. Locked nucleic acid (LNA) or short interfering RNA (siRNA) was used in co-injection, in the following concentrations: 10 μM LNA for control; 1 μM LNA for *LincGET*; and 10 μM siRNA for *Nono*, *Pspc1*, *Hnrnpu* or control.

Western blot

For each lane, 200 single blastomeres from embryos were lysed with RIPA lysis buffer (10 μl per lane; Beyotime, P00138) containing 1 mM phenylmethyl sulfonyl fluoride (PMSF; Beyotime, ST506), mixed with 30 μl of sample buffer (Beyotime, P0283) and incubated for 5 min in boiling water bath. The samples were then separated by SDS–PAGE with a 5% stacking gel (10 ml; 5.7 ml ddH₂O, 1.7 ml 30% acrylamide (29:1), 100 μl of 10% SDS, 2.5 ml 1.5 M pH 6.8 Tris-HCl, 50 μl of 10% ammonium persulfate and 10 μl of TEMED) and a 10% separating gel (10 ml; 4.1 ml ddH₂O, 2.5 ml 1.5 M pH 8.8 Tris-HCl, 3.3 ml 30% acrylamide (29:1), 100 μl of 10% SDS, 50 μl of 10% ammonium persulfate and 5 μl of TEMED) at 100 V for 1 h. Separated proteins were then electrophoretically transferred onto a nitrocellulose membrane at 250 mA for 1 h at 4 °C. Membranes were then blocked in TBST buffer (150 mM NaCl, 10 mM Tris, 0.1% Tween-20, pH 7.4) containing 3% BSA (Sigma, B2064), for 1 h at room temperature and then incubated with primary antibody, diluted (mass:volume ratio, 1:200) in TBST containing 1% BSA, overnight at 4 °C. After three washes for 10 min each in TBST, membranes were incubated for 1 h at room temperature with the fluorescence-labeled secondary antibody diluted (mass:volume ratio, 1:5,000) in TBST containing 1% BSA. After three washes for 10 min each, the membrane was exposed to a Bio-Rad GelDoc XR+ Gel imaging system for the acquisition of signals.

Immunoprecipitation

Magnetic Beads Protein G were coated with 5 μg of primary antibody in RIP wash buffer (150 mM sodium chloride, 50 mM Tris-HCl, pH 7.4, 1 mM MgCl₂ and 0.05% NP-40) containing 5% BSA overnight with rotation at 4 °C. Then, we collected approximately 1 × 10⁶ mEpiSCs expressing HA-MS2P, with or without MS2-*LincGET*, added to 100 μl of RIP lysis buffer (50 mM Tris-HCl pH 7.4, 150 mM NaCl, 1 mM EDTA pH 8.0 (Invitrogen, AM9260G), 1% NP-40, 0.1% SDS, 0.5% sodium deoxycholate, 0.5 mM DTT, 1 mM PMSF/cocktail) and 10 μl of RNase inhibitor (Ambion, AM2694) and incubated on ice for 10 min. For embryos injected with MS2-*LincGET* or MS2-*anti-LincGET*, pre-mRNAs for HA-MS2P and pre-mRNAs for NONO, about 400 embryos were used for each group. Next, we centrifuged the RIP lysate at 10,000×*g* for 10 min at 4 °C, removed 100 μl of the supernatant and added this to 900 μl of the beads–antibody complex (mass:volume ratio, 1:200) in RIP Immunoprecipitation Buffer (860 μl RIP wash buffer, 35 μl 0.5 M EDTA pH 8.0 and 5 μl RNase inhibitor) and incubated this with rotation overnight

at 4 °C. The residual 10 μl of the supernatant of RIP lysate was treated as input. After washing, the immunoprecipitate was divided into two parts. One part was mixed with 15 μl of western blot sample buffer and incubated for 5 min in boiling water; this blot was used to detect HA-MS2P and NONO/PSPC1/HNRNPU (according to the antibody). The other part was treated with proteinase K at 55 °C for 30 min with shaking to digest the protein, followed by RNA extraction from the supernatant; reverse transcription polymerase chain reaction (RT–PCR) was then performed to detect *LincGET*.

Immunofluorescence staining

Mouse embryos were permeabilized in 1% Triton X-100 (Sigma, T9284) in 1× PBS (Invitrogen, AM9625) and fixed in ice-cold 100% methanol for 30 min at −20 °C, followed by permeabilization again in 70% ethanol for 30 min at 4 °C. Then, embryos were blocked in blocking solution (1% BSA in 1× PBS) for 1 h at room temperature after three washes for 5 min each in washing solution (0.1% Tween-20, 0.01% Triton X-100 in 1× PBS), followed by incubation with primary antibody diluted (mass:volume ratio, 1:50) with blocking solution overnight at 4 °C. After three washes, embryos were incubated with Alexa series fluorescent tag-conjugated secondary antibody diluted (mass:volume ratio, 1:1,000) with washing solution for 1 h at room temperature. After three washes, embryos were mounted with DAPI-Vectashield solution (Vector laboratories, H1200). Notably, when the embryos were injected with Alexa Fluor 488-labeled *LincGET* and pre-mRNAs for NONO-mCherry, the embryos were directly mounted with DAPI-Vectashield solution (Vector laboratories, H1200) after permeabilization. When the embryos were injected with Alexa Fluor 488-labeled *LincGET*, pre-mRNAs for NONO-BFP and Alexa Fluor 546-labeled sgRNAs, the embryos were directly stained with SYTOX Deep Red Nucleic Acid Stain (Invitrogen, S11380) and then mounted after permeabilization. Imaging of embryos was then performed using a laser-scanning confocal microscope (Leica, TCS SP8). IMARIS software (Bitplane) was then used to calculate the number of speckles in each picture.

Immunofluorescence combined with RNA-FISH

Probes targeting *LincGET* used in RNA-FISH were labeled by in vitro transcription using the MEGAshortscript Kit (Ambion, AM1354) with ATP, CTP, GTP, UTP and ChromaTide Alexa Fluor 488-5-UTP (Invitrogen, C11403) solution (4:4:4:1:4) in which 80% of uracil was labeled by Alexa Fluor 488. The zona pellucida of the mouse embryos was removed with incubation in acidic Tyrode's Solution (Sigma, T1788). Then the embryos were incubated in PBSA (1× PBS containing 6 mg ml⁻¹ BSA) for 3 min and transferred onto Superfrost/Plus microscope slides and dried as quickly as possible (less than 5 min). Embryos were permeabilized in 1% Triton X-100 in 1× PBS and fixed in ice-cold 100% methanol for 30 min at −20 °C. Then, slides were transferred into 70% ethanol on ice for 20 min. To perform IF, slides were rinsed in PBS for 5 min, blocked in blocking buffer (1× PBS with 0.1% Tween-20, 1% BSA and 0.4 U μl⁻¹ of Ribonuclease Inhibitor (Invitrogen, 10777019)) for 20 min at room temperature, and then incubated with the primary antibody (mass:volume ratio, 1:50) in blocking buffer for 1 h at room temperature. After three washes with 0.1% Tween-20 in PBS, slides were incubated with secondary antibody (mass:volume ratio, 1:1,000) in blocking buffer for 1 h at room temperature. After three washes with 0.1% Tween-20 in PBS, slides were post-fixed in ice-cold 100% methanol for 30 min at −20 °C. The slides were then transferred into 70% ethanol on ice. Dehydration was performed in 80%, 95% and 100% ethanol (×2), with each incubation lasting for 5 min at room temperature. Slides were then dried for 5 min. Embryos were then hybridized in the hybridization solution (50% Formamide (Sigma, F9037), 1% Dextran Sulfate (Sigma, 30915), 2× SSC (Sigma, S6639-1L), 10 mM VRC (Sigma, 94742), 2 mg ml⁻¹ BSA) containing 5 μg of Alexa Fluor 488-labeled RNA probes per slide at 37 °C overnight (14–15 h). After three washes for 5 min each in hybridization washing solution (50% formamide, 2× SSC) at 42 °C and four washes for

5 min each in 2× SSC, embryos were mounted with DAPI-Vectashield solution (Vector laboratories, H1200). Fluorescence staining was imaged using a laser-scanning confocal microscope (Leica, TCS SP8). IMARIS software (Bitplane) was then used to calculate the number of speckles for each picture.

DNA-FISH combined with RNA-FISH

For the preparation of probes in DNA-FISH, 17 DNA fragments containing T7 promoter (2,100–2,700 bp) were amplified from the mouse genome using LongAmp *Taq* DNA Polymerase (NEB, M0534L). Primers are given in Supplementary Table 3. Then, in vitro transcription was performed with mixed 17 DNA fragments using the MEGAshortscript Kit (Ambion, AM1354) with ATP, CTP, GTP, UTP and ChromaTide Alexa Fluor 488-5-UTP (Invitrogen, C11403) solution (4:4:4:1:4), in which 80% of uracil was labeled by Alexa Fluor 488. The labeled RNA was then fragmented by adding 1× Ambion RNA fragmentation reagent (Ambion, AM8740) with incubation at 70 °C for 2 min. After adding the stop solution, the labeled RNA was purified and used as probes for DNA-FISH.

The zona pellucida of the mouse embryos was removed with incubation in acidic Tyrode's solution. Then the embryos were incubated in PBSA for 3 min and transferred onto Superfrost/Plus microscope slides and dried as quickly as possible (less than 5 min). Embryos were permeabilized in 1% Triton X-100 in 1× PBS and fixed in ice-cold 100% methanol for 30 min at −20 °C. Then, slides were transferred into 70% ethanol on ice for 20 min. To perform RNA-FISH, the procedures for dehydration and hybridization were performed as described in the 'IF combined with the RNA-FISH' section. After three washes for 5 min each in hybridization washing solution at 42 °C and four washes for 5 min each in 2× SSC, slides were post-fixed in 3% paraformaldehyde (PFA; Sigma, 158127) in PBS for 10 min at room temperature.

To perform DNA-FISH, the embryos were incubated with RNase Cocktail (Invitrogen, AM2288) in 1× PBS for 1 h at 37 °C. After three washes with 1× PBS, embryos were permeabilized in permeabilization solution II (0.7% Triton X-100 and 0.1 M HCl in 1× PBS) for 15 min on ice. Then, slides were transferred into 70% ethanol on ice for 20 min. Dehydration was performed in 80%, 95% and 100% ethanol (×2), with each incubation lasting for 5 min at room temperature. Slides were then dried for 5 min. Then the slides were denatured in the hybridization washing solution for 30 min at 80 °C. After dehydration in cold ethanol, the embryos were hybridized in the hybridization solution containing 5 μg of Alexa Fluor 546-labeled DNA probes per slide at 37 °C overnight (14–15 h). After three washes for 5 min each in hybridization washing solution (50% Formamide, 2× SSC) at 42 °C and four washes for 5 min each in 2× SSC, embryos were mounted with DAPI-Vectashield solution (Vector laboratories, H1200). Fluorescence staining was imaged using a laser-scanning confocal microscope (Leica, TCS SP8). IMARIS software (Bitplane) was then used to calculate the number of speckles for each picture.

Immunofluorescence combined with RNA-FISH and DNA-FISH

Immunofluorescence, RNA-FISH and DNA-FISH were performed as described above. For analysis of the heterogenous occupancy of *LincGET* speckles and PCBP1 around the *Carm1* gene loci, the embryos were injected with Alexa Fluor 488-labeled *LincGET*, pre-mRNAs for PCBP1-BFP and Alexa Fluor 546-labeled sgRNAs; then, the embryos were directly stained with SYTOX Deep Red Nucleic Acid Stain (Invitrogen, S11380) and Alexa Fluor 647 Phalloidin (Invitrogen, A22287) and then mounted after permeabilization.

ESS percentage analysis from published data

The raw data were downloaded from the GEO database. To trim the original data, the trim_galore (v.0.6.7) software was used with the default parameters. Next, STAR software was used to align reads to mouse genome sequences (https://ftp.ebi.ac.uk/pub/databases/gencode/Gencode_mouse/release_M29/GRCm39.primary_assembly.genome.fa.gz) with default parameters. RMATS (v.4.1.0) software was used to analyze the alternative splicing events and Rmats2sashimiplot (v.2.0.4) software was used for visualization. The levels of all types of alternative splicing events on *Carm1* pre-mRNAs were analyzed, including exon-skipping, retained introns, alternative 5′-splicing site, alternative 3′-splicing site, mutually exclusive exons, alternative first exons and alternative last exons.

The percentage of ESS events on exons 3 to 6 relative to noS splicing events is calculated based on Psi values (Ψ). The ESS events on exons 3 to 6 conclude E3S, E5S, E6S, E56S and E3456S; thus, the calculation formulas are as follows:

$$P(\text{noS}) = \frac{\frac{R(\text{noS})}{L(\text{E2 to E7})}}{\frac{R(\text{noS})}{L(\text{E2 to E7})} + \frac{R(\text{E3S})}{L(\text{E2}+\text{E4})} + \frac{R(\text{E5S})}{L(\text{E4}+\text{E6})} + \frac{R(\text{E6S})}{L(\text{E5}+\text{E7})} + \frac{R(\text{E56S})}{L(\text{E4}+\text{E7})} + \frac{R(\text{E3456S})}{L(\text{E2}+\text{E7})}}$$

$$P(\text{E3S}) = \frac{\frac{R(\text{E3S})}{L(\text{E2}+\text{E4})}}{\frac{R(\text{noS})}{L(\text{E2 to E7})} + \frac{R(\text{E3S})}{L(\text{E2}+\text{E4})} + \frac{R(\text{E5S})}{L(\text{E4}+\text{E6})} + \frac{R(\text{E6S})}{L(\text{E5}+\text{E7})} + \frac{R(\text{E56S})}{L(\text{E4}+\text{E7})} + \frac{R(\text{E3456S})}{L(\text{E2}+\text{E7})}}$$

$$P(\text{E5S}) = \frac{\frac{R(\text{E5S})}{L(\text{E4}+\text{E6})}}{\frac{R(\text{noS})}{L(\text{E2 to E7})} + \frac{R(\text{E3S})}{L(\text{E2}+\text{E4})} + \frac{R(\text{E5S})}{L(\text{E4}+\text{E6})} + \frac{R(\text{E6S})}{L(\text{E5}+\text{E7})} + \frac{R(\text{E56S})}{L(\text{E4}+\text{E7})} + \frac{R(\text{E3456S})}{L(\text{E2}+\text{E7})}}$$

$$P(\text{E6S}) = \frac{\frac{R(\text{E6S})}{L(\text{E5}+\text{E7})}}{\frac{R(\text{noS})}{L(\text{E2 to E7})} + \frac{R(\text{E3S})}{L(\text{E2}+\text{E4})} + \frac{R(\text{E5S})}{L(\text{E4}+\text{E6})} + \frac{R(\text{E6S})}{L(\text{E5}+\text{E7})} + \frac{R(\text{E56S})}{L(\text{E4}+\text{E7})} + \frac{R(\text{E3456S})}{L(\text{E2}+\text{E7})}}$$

$$P(\text{E56S}) = \frac{\frac{R(\text{E56S})}{L(\text{E4}+\text{E7})}}{\frac{R(\text{noS})}{L(\text{E2 to E7})} + \frac{R(\text{E3S})}{L(\text{E2}+\text{E4})} + \frac{R(\text{E5S})}{L(\text{E4}+\text{E6})} + \frac{R(\text{E6S})}{L(\text{E5}+\text{E7})} + \frac{R(\text{E56S})}{L(\text{E4}+\text{E7})} + \frac{R(\text{E3456S})}{L(\text{E2}+\text{E7})}}$$

$$P(\text{E3456S}) = \frac{\frac{R(\text{E3456S})}{L(\text{E2}+\text{E7})}}{\frac{R(\text{noS})}{L(\text{E2 to E7})} + \frac{R(\text{E3S})}{L(\text{E2}+\text{E4})} + \frac{R(\text{E5S})}{L(\text{E4}+\text{E6})} + \frac{R(\text{E6S})}{L(\text{E5}+\text{E7})} + \frac{R(\text{E56S})}{L(\text{E4}+\text{E7})} + \frac{R(\text{E3456S})}{L(\text{E2}+\text{E7})}}$$

where *P* is the percentage of the splicing event; *R* is the number of reads with the splicing event; and *L* is the length of exons.

For other alternative splicing events, including the alternative 3′-splicing site of exon 4 (E4A3SS), retained intron 14 (RI14), retained intron 15 (RI15), exon 2 skipping splicing (E2S), exon 3a inclusive (E3a), E11S and E15S, the percentage of these alternative splicing (AS) relative to non-alternative splicing (noAS) is calculated based on Ψ, and the formulas are as follows:

$$P(\text{noAS}) = \frac{R(\text{noAS})}{R(\text{noAS}) + R(\text{AS})}$$

$$P(\text{AS}) = \frac{R(\text{AS})}{R(\text{noAS}) + R(\text{AS})}$$

where *P* is the percentage of the splicing event and *R* is the number of reads with the splicing event.

SPAR-seq and data analysis

The zona pellucida of embryos was removed using Tyrode's solution (Sigma, T1788). Zona-free embryos were incubated for 5 min in Ca^{2+}-free and Mg^{2+}-free M2 medium before disaggregation by careful pipetting. For single-cell SPAR-seq, each blastomere of two-cell or four-cell embryos was transferred to individual tubes containing 2.3 μl of lysis buffer (0.2% Triton X-100 supplemented with 1 U ml^{-1} ribonuclease inhibitor (Invitrogen, 10777019)). For bulk SPAR-seq, blastomeres of 50 embryos at the four-cell stage of each group were placed into two individual tubes containing 2.3 μl of lysis buffer separated by GFP$^+$ or

GFP[−]. Reverse transcription was performed with a Single Cell-to-CT qRT–PCR Kit (Invitrogen, 4458237). PCR was performed using primers targeting exon 2 and exon 7 of *Carm1* mRNA (Supplementary Table 3).

The samples were sequenced using an Illumina MiSeq sequencer with 300 bp paired-end sequencing reactions (PE300) at BGI company (https://www.genomics.cn). Clean reads were merged using pear (v.0.9.6)[55] software with default parameters. Given that the noS and E3a (with longer exon 4, from XM_030244479.2) sequences are longer than 600 bp, the noS and E3a reads were separated into unassembled. forward.fastq and fq.unassembled.reverse.fastq files, whereas the AS reads (E3S, E4S, E5S, E6S, E34S, E56S, E345S and E3456S) and the *Gfp* spike-ins were separated into assembled.fastq files. To count the AS reads, reads in the assembled.fastq files were mapped to the reference transcripts, including all the exon-skipping candidates, with bowtie2 (v.2.2.5) software[56] and transferred into *bam* files with samtools (v.1.9)[57] software. To count the noS and E3a reads, Carm1_E3a_analysis. py (https://github.com/NEAU-Wang-lab/SPAR-seq) was used to note reads in unassembled.forward.fastq and fq.unassembled.reverse. fastq files.

Some samples were sequenced on a PacBio Sequel System according to the standard PacBio Iso-Seq procedures at Annoroad company (http://www.annoroad.com) mixed with samples from other experiments. Then, circular consensus sequencing (CCS) reads were generated using ccs (v.5.0.0) software and converted to fastq format using bam2fastq software in the pbbam (v.1.0.6) package. The number of passes for each of the raw CCS reads was generated using GetCCSpass. pl (https://github.com/Lulab-IGDB/polyA_analysis/blob/main/bin). Then the clean reads of *Carm1* were extracted from the CCS reads using Carm1_SPAR_reads_extract.py. Carm1_AS_analysis.py (https://github. com/NEAU-Wang-lab/SPAR-seq) was used to count the AS reads, and Carm1_E3a_analysis.py was used to count the noS and E3a reads.

SHAPE-MaP assays and data analysis

The in vitro transcribed *LincGET* was re-folded in folding buffer (100 mM NaCl, 100 mM HEPES pH 8.0 and 10 mM MgCl$_2$ in water) at 37 °C for 20 min with or without NONO, PSPC1 or HNRNPU. As a control, one group of *LincGET* was denatured in denaturing control buffer (50% formamide, 50 mM HEPES pH 8.0 and 4 mM EDTA pH 8.0 in water) at 95 °C for 1 min. For each group, approximately 5 μg RNA was added to the one-ninth volume of NMIA (Invitrogen, M25) at 100 mM in neat DMSO (10 mM final concentration) and incubated at 37 °C for 22 min. The background was assessed by performing no-reagent and denaturing controls.

After fragmentation with RNA fragmentation reagent (Ambion, AM8740), modified *LincGET* was subjected to MaP reverse transcription[27], with SuperScript II Reverse Transcriptase (Invitrogen, 18064014) under Mn^{2+} conditions (50 mM Tris-HCl pH 8.0, 75 mM KCl, 10 mM DTT, 2 mM dNTPs and 15 mM MnCl$_2$ in water) using random nonamer primers (200 ng μl^{-1}; NEB, S1254S). After synthesizing the second strand by NEBNext pre-mRNAs Second Strand Synthesis Module (NEB, E6111S), the resulting cDNAs were constructed for high-throughput sequencing libraries and sequenced by BGI company.

The deep sequencing datasets were analyzed by ShapeMapper2 (v.2.1.5)[58] software with default parameters. The reads were mapped to target sequences by bowtie2 (v.2.2.5)[56] software with default parameters as recommended by ShapeMapper2. RNA secondary structures were modeled by Superfold (v.1.0)[59] with map files produced by ShapeMapper2. The RNA stem-loop structures for specific fragments were produced by VARNA (v.3.93)[60]. The ct files from Superfold were used for visualization and varna_colors.txt files from ShapeMapper2 output were used for the reactivity coloring.

Protein purification

Plasmids expressing the NONO, PCBP1 or PCBP2 fused to EGFP tagged with MBP and 6×His (MBP–NONO-EGFP–6×His) were transformed into Transetta (DE3) Chemically Competent Cells (TransGen, CD801). A fresh bacterial colony was inoculated into 4 ml LB media containing ampicillin and grown for 6–8 h at 37 °C until the A600 reached about 0.5. Cells were diluted into 600 ml (1:150) room temperature LB with freshly added ampicillin and grown for 8–12 h at 37 °C. IPTG (TransGen, GF101-01) was added to 1 mM and growth continued for 18 h at 16 °C. Pellets from 600 ml cells were resuspended in 30 ml of Buffer A (50 mM Tris pH 7.5, 500 mM NaCl, 1% Triton X-100, 10 mM imidazole and 1× cOmplete protease inhibitors (Roche, 11873580001)) and divided equally into three 50 ml tubes. For each tube containing 10 ml suspended cells, 15 min of sonication (90 cycles of 5 s on, 5 s off) at 300 W was suitable. The lysate was mixed and cleared by centrifugation at 8,000*g* for 5 min at 4 °C followed by filtration with a 0.45 μm filter.

Next, the MBP-tagged proteins were purified using a PurKine MBP-Tag Dextrin Packed Column (Dextrin, BMC20206), according to the manufacturer's instructions. In brief, the top and bottom stoppers on the column were removed to let the stored buffer drain away. Two aliquots of resin-bed volume binding/washing buffer (2 mM Tris-HCl, 20 mM NaCl, 0.1 mM EDTA pH 8.0 and 1 mM DTT) were added to the column and drained away to equilibrate the column. The equilibration step was repeated three times. The cleared lysate was mixed with equal binding/washing buffer and added to the column. For maximal binding, the sample was incubated for 30 min at room temperature or 4 °C. After the sample was drained away, two aliquots of resin-bed volume binding/washing buffer were added to the column and drained to remove the non-specifically adsorbed protein. The washing step was repeated six times. Then, 10 ml of elution buffer (2 mM Tris-HCl, 0.1 mM EDTA pH 8.0, 1 mM Maltose pH 7.4 and 1 mM DTT) was added to the column to wash the target protein. The wash liquid was collected and the content was analyzed using a Coomassie-stained SDS–PAGE gel.

After testing the protein concentration using the Super-Bradford Protein Assay Kit (CWBio, CW0013S), the MBP tag was removed from the purified protein using Factor Xa Protease (NEB, P8010L), in which 1 μg of Factor Xa was added to 50 μg of MBP fusion protein for 24 h at 4 °C.

Next, the sample containing NONO-EGFP–6×His, PCBP1-EGFP–6×His or PCBP2-EGFP–6×His was purified by ProteinIso Ni-NTA Resin (TransGen, DP101-02) combined with an Affinity Chromatography Column (12 ml; TransGen, GP101-03), according to the manufacturer's instructions. In brief, 6 ml Ni-NTA was added to the column and equilibrated with 60 ml Buffer A. The sample was poured into the column and then washed with 15 volumes of Buffer B (20 mM Tris pH 7.5, 500 mM NaCl, 1% NP-40, 1 mM DTT, 10 mM imidazole and 1× cOmplete protease inhibitors). Protein was eluted with 4 ml Buffer C (20 mM Tris pH 7.5, 500 mM NaCl, 1% NP-40, 1 mM DTT, 200 mM imidazole, and 1× cOmplete protease inhibitors). The wash liquid was collected and the contents were analyzed using a Coomassie-stained SDS–PAGE gel.

Next, the sample (4 ml) was dialyzed in Slide-A-Lyzer 20K Dialysis Cassettes (Thermo, 66012) against 1 l of Buffer D (50 mM Tris-HCl pH 7.5, 125 mM NaCl, 10% glycerol, 1 mM DTT) twice at 4 °C for 8 h each time. Then the sample was concentrated using 30K MWCO Amicon MLtra Centrifugal Filters (Millipore, UFC803024) to 200–1,000 μl via centrifuge at 7,500×*g* at 4 °C for 30 min. The protein concentration was measured using the Super-Bradford Protein Assay Kit (CWBio, CW0013S).

ChIP and data analysis

For chromatin immunoprecipitation to analyze *LincGET* binding DNA sites, embryos were injected with the *LincGET-MS2* and mRNAs for HA-tagged MS2P at the pronuclear stage and collected at the early four-cell stage. For each batch, embryos were washed three times with 1× PBS and were crosslinked for 40 min in a droop containing 1.5 mM freshly prepared ethylene glycol bis(succinimidyl succinate) (EGS; Thermo Scientific, 21566) in a chemical fume hood at room temperature with rotation. Then the embryos were dual-crosslinked in a droop

containing 1% formaldehyde (Sigma, 8187081000) for 20 min in a chemical fume hood at room temperature with rotation. To quench the crosslinkers, the embryos were moved to a droop containing 200 mM glycine and were incubated for 10 min at room temperature with rotation in a chemical fume hood. Then embryos were washed three times with 1× PBS and stored at −80 °C with as little liquid as possible until use.

Some batches were combined to collect about 1,000 embryos for each replicate using 20 µl nuclei extraction buffer (10 mM Tris-HCl pH 8.5 (Sigma, 87772), 140 mM NaCl (Sigma, S6546), 5 mM MgCl$_2$ (Invitrogen, AM9530G), 0.6% NP-40 (Abcam, ab142227), 1 mM PMSF, 1× protease unhibitors complex (PIC, CST, 7012)) and incubated for 2 min on ice. For chromatin digestion, the samples were added with 80 µl chromatin digestion buffer (1× MNase buffer (NEB, M0247S), 2 mM DTT, 5% PEG6000 (Avantor, 1008060), 60 U µl^{-1} MNase (NEB, M0247S)) and incubated at room temperature for 5 min. Then the samples were added with 11 µl MNase stop solution and incubated at room temperature for 1 min. Next, the samples were added with 13 µl nuclear break buffer (1% Triton X-100, 1% odium deoxycholate (Sigma, 30970), 1× PIC) and 86 µl 10× ChIP buffer (CST, 7008) to a final volume of 210 µl, 10 µl of which was treated as input and the other 200 µl of which was used for immunoprecipitation. Before immunoprecipitation, the magnetic beads (CST, 9006) were washed three times with 1× ChIP buffer.

For immunoprecipitation, each sample was added with 1 µg anti-HA antibody (mass:volume ratio, 1:200) and incubated overnight at 4 °C with rotation. Then the samples were added with 12 µl magnetic beads (CST, 9006) and incubated for 5 h at 4 °C with rotation. Next, the beads were washed with 1× ChIP buffer four times for 5 min each time at 4 °C with rotation and with high salt wash buffer (300 µl 10× ChIP buffer, 2,700 µl H$_2$O, 210 µl 5 M NaCl) three times for 5 min at 4 °C with rotation. After washing, chromatin was eluted from the beads with 100 µl 1× ChIP elution buffer (CST, 7009) with incubation at 65 °C for 30 min. The reverse crosslink was performed by adding 4 µl 5 M NaCl and 1 µl proteinase K (20 mg ml^{-1}; Beyotime, ST533) and incubation at 65 °C for 4 h. Then the DNA was extracted by 100 µl chloroform and was precipitated by adding 10 µl of 3 M sodium acetate pH 5.5 (Invitrogen, AM9740), 300 µl isopropanol and 1 µl glycogen (15 mg ml^{-1}; Invitrogen, AM9516) and incubation for 30 min at −80 °C. After washing twice with cold 75% ethanol, the DNA pellet was dissolved with 10 µl of nuclease-free water. Finally, DNA library preparation and sequencing on Hiseq 2500 were performed by BGI company.

For H3R26me2 ChIP–qPCR, anti-H3R26me2 antibody (Abcam, ab127095) was used for immunoprecipitation (mass:volume ratio, 1:200), and qPCR was performed instead of DNA library preparation and sequencing.

The deep sequencing datasets were trimmed by trim_galore (v.0.6.7)[61] software with default parameters. The reads were mapped to mouse genome sequences (https://ftp.ebi.ac.uk/pub/databases/gencode/Gencode_mouse/release_M29/GRCm39.primary_assembly.genome.fa.gz) by bwa (v.0.7.17-r1188)[62] software with default parameters and transferred into bam files with samtools (v.1.9)[57] software. Finally, the bam files were loaded into the IGV (v.2.16.2) for visualization. Peak calling was performed by macs2 (v.2.1.1.20160309) software after duplex removing by picard (v.2.18.29-0) software.

RNA electrophoretic mobility shift assays
RNA oligonucleotides were in vitro transcribed using HiScribe T7 Quick High Yield RNA Synthesis Kit (NEB, E2050) following the manufacturers' guidelines. DNA templates with a T7 promoter were generated by annealing with primers listed in Supplementary Table 3. RNA oligonucleotides were then biotinylated using the Pierce RNA 3′ End Desthiobiotinylation Kit (Thermo Scientific, 20163) according to the manufacturer's instructions. The labeled oligonucleotides were gel-purified on 12% denaturing gels before use. The gel shift assay was carried out using the LightShift Chemiluminescent RNA EMSA Kit (Thermo Scientific, 20158). In brief, 5 ng biotinylated wild-type or

mutant RNA probe was mixed with 50 µg of 6×His-purified PCBP1 and PCBP2 mix (6×His−PCBP1) (and anti-PCBP1 or anti-PCBP2 antibody for super-shifts (mass:volume ratio, 1:500)) and incubated at room temperature for 30 min in a 20 µl binding reaction containing 1× binding buffer, 5% glycerol and 0.1 mg ml^{-1} tRNA. The samples were electrophoresed on a 5% native PAGE in 0.5× Tris Borate EDTA (Thermo Scientific, B52), transferred to a positively charged BrightStar-Plus Nylon membrane (Invitrogen, AM10100) and crosslinked in a UV Stratalinker 1800 (Stratagene). To block the membrane, the membrane was incubated in 20 ml nucleic acid detection blocking buffer for 15 min with gentle shaking and then was incubated in 20 ml conjugate/blocking solution (20 ml nucleic acid detection blocking buffer containing 66.7 µl stabilized streptavidin-horseradish peroxidase conjugate) for 15 min with gentle shaking. After washing four times for 5 min each in 20 ml 1× wash buffer with gentle shaking, the membrane was incubated in 30 ml substrate equilibration buffer for 5 min with gentle shaking. Then the membrane was incubated in 12 ml substrate working solution (6 ml luminol/enhancer solution and 6 ml stable peroxide solution) for 5 min without shaking. Finally, the membrane was exposed to a Bio-Rad GelDoc XR+ Gel imaging system for the acquisition of signals.

Minigene analysis of ESS
The minigene plasmids and plasmids encoding shRNAs targeting *Pcbp1/2* or control shRNAs were co-transfected into MCF-7 cells. Cells were collected 72 h post transcription, and total RNA was extracted. Then RT–PCR was performed with the primers listed in Supplementary Table 3.

Dot blotting
Single blastomeres were separated from late two-cell and early four-cell embryos and transferred into PCR tubes containing 10 µl of 0.2% (vol/vol) Triton X-100 (Sigma, T9284) and 0.5 µl of RNase inhibitor (Clontech, 2313A). The lysate was split into three equal portions, which were used for dot plotting for CARM1, qPCR for the ESS isoform *Carm1_E56S* and qPCR for the total expression level of *Carm1*. For dot blotting, lysates from a series of single blastomeres were spotted onto a nitrocellulose membrane and allowed to absorb. Then the membrane was blocked, incubated sequentially with anti-CARM1 antibody (mass:volume ratio, 1:100) and fluorescence-labeled secondary antibody (mass:volume ratio, 1:5,000), and then exposed to a Bio-Rad GelDoc XR+ Gel imaging system in the same way as those in the 'Western blot' section above.

Secondary structure comparison between *LincGET* and *Neat1*
The RNA secondary structures of *LincGET* and *Neat1* were predicted and compared using the ViennaRNA package[63]. Firstly, sequences of *LincGET* and *Neat1* were split into 500 nt fragments, with the two adjacent fragments overlapped by 100 nt. Then the RNAfold function was used to predict the RNA secondary structures and the RNAdistance function was used to measure the dissimilarity of the RNA secondary structures in a bracket format. The resulting f values are shown in Supplementary Table 5. The smaller the f value, the more similar the structure.

To determine the f values that represent high enough structural similarity, the distribution of f values from the comparison between 52 *Neat1* fragments and 10,000 random mRNA fragments (500 nt each) was plotted. We found that the distribution curve is approximately normal, and the boundary of the left 2.5% ($P < 0.05$) is 320 (Supplementary Fig. 2c). Therefore, we considered structural similarity to be high enough if the f value is less than 320.

Two comparisons with f values less than 320 (Supplementary Fig. 2d and Supplementary Table 5) were found. The secondary structures of these fragments were predicted using the RNAfold web server (http://rna.tbi.univie.ac.at/cgi-bin/RNAWebSuite/RNAfold.cgi).

Absolute qPCR for *LincGET* and *Neat1_2*

Firstly, PCR using Q5U Hot Start High-Fidelity DNA Polymerase (NEB, M0515) with primers for TaqMan quantitative real-time PCR (Supplementary Table 3) was performed, and the PCR products were purified using the Zymoclean Gel DNA Recovery Kit (ZYMO, D4007). Standard curves were made using the purified PCR results for *LincGET* and *Neat1*. Serial diluted PCR products were used. Standard curves with threshold cycle (C_t) values on the x axis and the logarithmic value with base 2 ($\log_2$) of molecular concentration (number of molecules/μl) on the y axis were generated for quantification (Supplementary Table 6). Next, three groups of late two-cell embryos (200 embryos each), three groups of early four-cell embryos (200 embryos each) and three groups of mEpiSCs using FACS (10,000 cells each) were collected. After total RNA extraction and reverse transcription, real-time PCR was performed using TaqMan Universal Master Mix II. The copy numbers of *LincGET* and *Neat1* in late two-cell and early four-cell embryos as well as in mEpiSCs were calculated in Excel.

Statistical analyses

Statistical analyses (mean ± s.e.m.) for differential gene expression, differential fluorescence intensity and differential abundance on gels were performed in Excel. Levels of significance were calculated with Student's t-tests. Isoform abundance on SDS–PAGE gels or agarose gels was measured in Fiji/ImageJ. The co-localization analysis of *LincGET* signals with NONO, PSPC1, PCBP1, U2AF2, SRSF1 or *Carm1* gene locus in live imaging assays, RNA-FISH combined with immunofluorescence assays and RNA-FISH combined with DNA-FISH assays were calculated by the two (green and red) or three (green, red and blue) separate channel signals per nucleus using Pearson's correlation coefficient with Coloc 2 plugins in Fiji/ImageJ. Line scans of the relative fluorescence intensity of signals were drawn by separate channel signals with the Plot Profile plugins in Fiji/ImageJ. Particle numbers of *LincGET* speckles, NONO speckles, PSPC1 speckles and PCBP1 speckles were calculated by Imaris with the particle building system. The R^2 value for linear regression was calculated in Excel.

Reporting summary

Further information on research design is available in the Nature Portfolio Reporting Summary linked to this article.

Data availability

The sequencing data of SPAR-seq, SHAPE-MaP-seq and *LincGET* ChIP–seq have been deposited in the Genome Sequence Archive of Beijing Institute of Genomics, Chinese Academy of Sciences (GSA; http://gsa.big.ac.cn) with accession numbers CRA007472, CRA007494 and CRA007495, respectively. This study also includes analysis of the following published data in the Gene Expression Omnibus database (GEO): GSE85019, GSE71257 (ref. 64), GSE163724 (ref. 65), GSE135457 (ref. 66), GSE45719 (ref. 67), GSE127106, GSE138760 (ref. 23), GSE153530 (ref. 68), GSE98150 (ref. 69), GSE66582 (ref. 70), GSE135678 (ref. 71), GSE151704, GSE171760 (ref. 72), GSE160894 (ref. 73), GSE169632 (ref. 74), GSE137630 (ref. 75), GSE161998 (ref. 51), GSE180259 (ref. 76), GSE165133 (ref. 77), GSE117815, GSE178298 (ref. 78), GSE162352 (ref. 79), GSE181800 (ref. 52), GSE173471 (ref. 80), GSE242289, GSE194115 (ref. 53), GSE194203, GSE201938, GSE226534 (ref. 81), GSE192404 (ref. 54), GSE151260 (ref. 82), GSE156568 (ref. 83), GSE228894 (ref. 84), GSE199546 (ref. 85), GSE189015, GSE150510 (ref. 86), GSE148019 (ref. 87), GSE184348 (ref. 88), GSE179888 (ref. 89), GSE181651, GSE197122 (ref. 90), GSE167360 (ref. 91), GSE234841 (ref. 92), GSE202260 (ref. 93), GSE190199, GSE114450 (ref. 94), GSE196236 (ref. 35), GSE147574, GSE235546, GSE71434 (ref. 95), GSE159484 and GSE149785 (ref. 96); and data from the GSA: CRA007513 (ref. 2).

The mouse genome sequences are available at the website https://ftp.ebi.ac.uk/pub/databases/gencode/Gencode_mouse/release_M29/GRCm39.primary_assembly.genome.fa.gz. Source data are provided with this paper.

Code availability

For analysis of SPAR-seq data, the Carm1_SPAR_reads_extract.py, Carm1_AS_analysis.py, and Carm1_E3a_analysis.py are available on the website https://github.com/NEAU-Wang-lab/SPAR-seq, and the GetC-CSpass.pl is available on the website https://github.com/Lulab-IGDB/polyA_analysis/blob/main/bin/.

References

55. Zhang, J., Kobert, K., Flouri, T. & Stamatakis, A. PEAR: a fast and accurate Illumina paired-end reAd mergeR. *Bioinformatics* **30**, 614–620 (2014).
56. Kent, W. J. BLAT—the BLAST-like alignment tool. *Genome Res.* **12**, 656–664 (2002).
57. Danecek, P. et al. Twelve years of SAMtools and BCFtools. *Gigascience* **10**, giab008 (2021).
58. Busan, S. & Weeks, K. M. Visualization of RNA structure models within the Integrative Genomics Viewer. *RNA* **23**, 1012–1018 (2017).
59. Siegfried, N. A., Busan, S., Rice, G. M., Nelson, J. A. & Weeks, K. M. RNA motif discovery by SHAPE and mutational profiling (SHAPE-MaP). *Nat. Methods* **11**, 959–965 (2014).
60. Darty, K., Denise, A. & Ponty, Y. VARNA: interactive drawing and editing of the RNA secondary structure. *Bioinformatics* **25**, 1974–1975 (2009).
61. Kechin, A., Boyarskikh, U., Kel, A. & Filipenko, M. cutPrimers: a new tool for accurate cutting of primers from reads of targeted next generation sequencing. *J. Computational Biol.* **24**, 1138–1143 (2017).
62. Li, H. & Durbin, R. Fast and accurate long-read alignment with Burrows–Wheeler transform. *Bioinformatics* **26**, 589–595 (2010).
63. Lorenz, R. et al. ViennaRNA package 2.0. *Algorithms Mol. Biol.* **6**, 26 (2011).
64. Yu, C. et al. BTG4 is a meiotic cell cycle-coupled maternal–zygotic-transition licensing factor in oocytes. *Nat. Struct. Mol. Biol.* **23**, 387–394 (2016).
65. Li, M. et al. Integrative proteome analysis implicates aberrant RNA splicing in impaired developmental potential of aged mouse oocytes. *Aging Cell* **20**, e13482 (2021).
66. Liu, B. et al. The landscape of RNA Pol II binding reveals a stepwise transition during ZGA. *Nature* **587**, 139–144 (2020).
67. Deng, Q., Ramskold, D., Reinius, B. & Sandberg, R. Single-cell RNA-seq reveals dynamic, random monoallelic gene expression in mammalian cells. *Science* **343**, 193–196 (2014).
68. Chen, Z., Djekidel, M. N. & Zhang, Y. Distinct dynamics and functions of H2AK119ub1 and H3K27me3 in mouse preimplantation embryos. *Nat. Genet.* **53**, 551–563 (2021).
69. Wang, C. et al. Reprogramming of H3K9me3-dependent heterochromatin during mammalian embryo development. *Nat. Cell Biol.* **20**, 620–631 (2018).
70. Wu, J. et al. The landscape of accessible chromatin in mammalian preimplantation embryos. *Nature* **534**, 652–657 (2016).
71. Lismer, A. et al. Histone H3 lysine 4 trimethylation in sperm is transmitted to the embryo and associated with diet-induced phenotypes in the offspring. *Dev. Cell* **56**, 671–686.e6 (2021).
72. Shi, Y. et al. Functional roles of the chromatin remodeler SMARCA5 in mouse and bovine preimplantation embryosdagger. *Biol. Reprod.* **105**, 359–370 (2021).
73. Wang, Y. et al. Sperm microRNAs confer depression susceptibility to offspring. *Sci. Adv.* **7**, eabd7605 (2021).
74. Zhang, C., Wang, M., Li, Y. & Zhang, Y. Profiling and functional characterization of maternal mRNA translation during mouse maternal-to-zygotic transition. *Sci. Adv.* **8**, eabj3967 (2022).
75. Zhang, C. et al. LncRNA5251 inhibits spermatogenesis via modification of cell–cell junctions. *Biol. Direct* **18**, 31 (2023).

76. Le, R. et al. Dcaf11 activates Zscan4-mediated alternative telomere lengthening in early embryos and embryonic stem cells. *Cell Stem Cell* **28**, 732–747.e9 (2021).

77. Gonen, N. et al. In vitro cellular reprogramming to model gonad development and its disorders. *Sci. Adv.* **9**, eabn9793 (2023).

78. Katsman, M., Azriel, A., Horev, G., Reizel, Y. & Levi, B. Z. N-VEGF, the autoregulatory arm of VEGF-A. *Cells* **11**, 1289 (2022).

79. Mrouj, K. et al. Ki-67 regulates global gene expression and promotes sequential stages of carcinogenesis. *Proc. Natl Acad. Sci. USA* **118**, e2026507118 (2021).

80. Mao, Y. et al. Continuous expression of reprogramming factors induces and maintains mouse pluripotency without specific growth factors and signaling inhibitors. *Cell Prolif.* **54**, e13090 (2021).

81. Gui, Y. et al. Calponin 2 regulates ketogenesis to mitigate acute kidney injury. *JCI Insight* **8**, e170521 (2023).

82. Yan, H. et al. Ten-eleven translocation methyl-cytosine dioxygenase 2 deficiency exacerbates renal ischemia–reperfusion injury. *Clin. Epigenetics* **12**, 98 (2020).

83. Gao, Y. et al. Systematic discovery of signaling pathways linking immune activation to schizophrenia. *iScience* **24**, 103209 (2021).

84. Shimazu, T. et al. Histidine N1-position-specific methyltransferase CARNMT1 targets C3H zinc finger proteins and modulates RNA metabolism. *Genes Dev.* **37**, 724–742 (2023).

85. Zheng, X. et al. Time-course transcriptome analysis of lungs from mice infected with hypervirulent *Klebsiella pneumoniae* via aerosolized intratracheal inoculation. *Front. Cell Infect. Microbiol.* **12**, 833080 (2022).

86. Meijboom, K. E. et al. Combining multiomics and drug perturbation profiles to identify muscle-specific treatments for spinal muscular atrophy. *JCI Insight* **6**, e149446 (2021).

87. Luo, W. et al. *TMEM182* interacts with integrin beta 1 and regulates myoblast differentiation and muscle regeneration. *J. Cachexia Sarcopenia Muscle* **12**, 1704–1723 (2021).

88. Zhang, X. et al. Characterization of cellular senescence in aging skeletal muscle. *Nat. Aging* **2**, 601–615 (2022).

89. Zhang, X., Liu, G., Zhang, N. & Hua, K. A time-resolved transcriptome landscape of the developing mouse ovary. *Biochem. Biophys. Res. Commun.* **572**, 57–64 (2021).

90. Chakraborty, P., Anderson, R. L. & Roy, S. K. Bone morphogenetic protein 2- and estradiol-17β-induced changes in ovarian transcriptome during primordial follicle formation. *Biol. Reprod.* **107**, 800–812 (2022).

91. Dai, Z., Chen, J., Chang, Y. & Christiano, A. M. Selective inhibition of JAK3 signaling is sufficient to reverse alopecia areata. *JCI Insight* **6**, e142205 (2021).

92. Rinaldi, A. O. et al. Household laundry detergents disrupt barrier integrity and induce inflammation in mouse and human skin. *Allergy* **79**, 128–141 (2024).

93. Lin, Z. et al. microRNA-144/451 decreases dendritic cell bioactivity via targeting interferon-regulatory factor 5 to limit DSS-induced colitis. *Front Immunol.* **13**, 928593 (2022).

94. Kim, J. E. et al. Single cell and genetic analyses reveal conserved populations and signaling mechanisms of gastrointestinal stromal niches. *Nat. Commun.* **11**, 334 (2020).

95. Zhang, B. et al. Allelic reprogramming of the histone modification H3K4me3 in early mammalian development. *Nature* **537**, 553–557 (2016).

96. Zhang, J. M. et al. Argonaute 2 is a key regulator of maternal mRNA degradation in mouse early embryos. *Cell Death Discov.* **6**, 133 (2020).

Acknowledgements

Author contributions

J.W. and Y.L. conceived and designed the study. J.W., C.L., X.L., P.L., L.W. and Y.L. performed the experiments. J.W., Y.Z., J.G., G.F. and Y.L. analyzed the data. J.W., Z.L., F.L., L.W., W.L., Q.Z. and Y.L. wrote the manuscript. J.W., L.W., W.L., Q.Z. and Y.L. supervised the project.

Competing interests

The authors declare no competing interests.

Additional information

Extended data is available for this paper at https://doi.org/10.1038/s41594-024-01292-9.

Supplementary information The online version contains supplementary material available at https://doi.org/10.1038/s41594-024-01292-9.

Correspondence and requests for materials should be addressed to Jiaqiang Wang, Leyun Wang, Wei Li, Qi Zhou or Yusheng Liu.

Peer review information *Nature Structural & Molecular Biology* thanks L. L. Chen, H. Y. Fan and W. Shu for their contribution to the peer review of this work. Primary Handling Editors: Carolina Perdigoto and Dimitris Typas, in collaboration with the *Nature Structural & Molecular Biology* team.

Reprints and permissions information is available at www.nature.com/reprints.
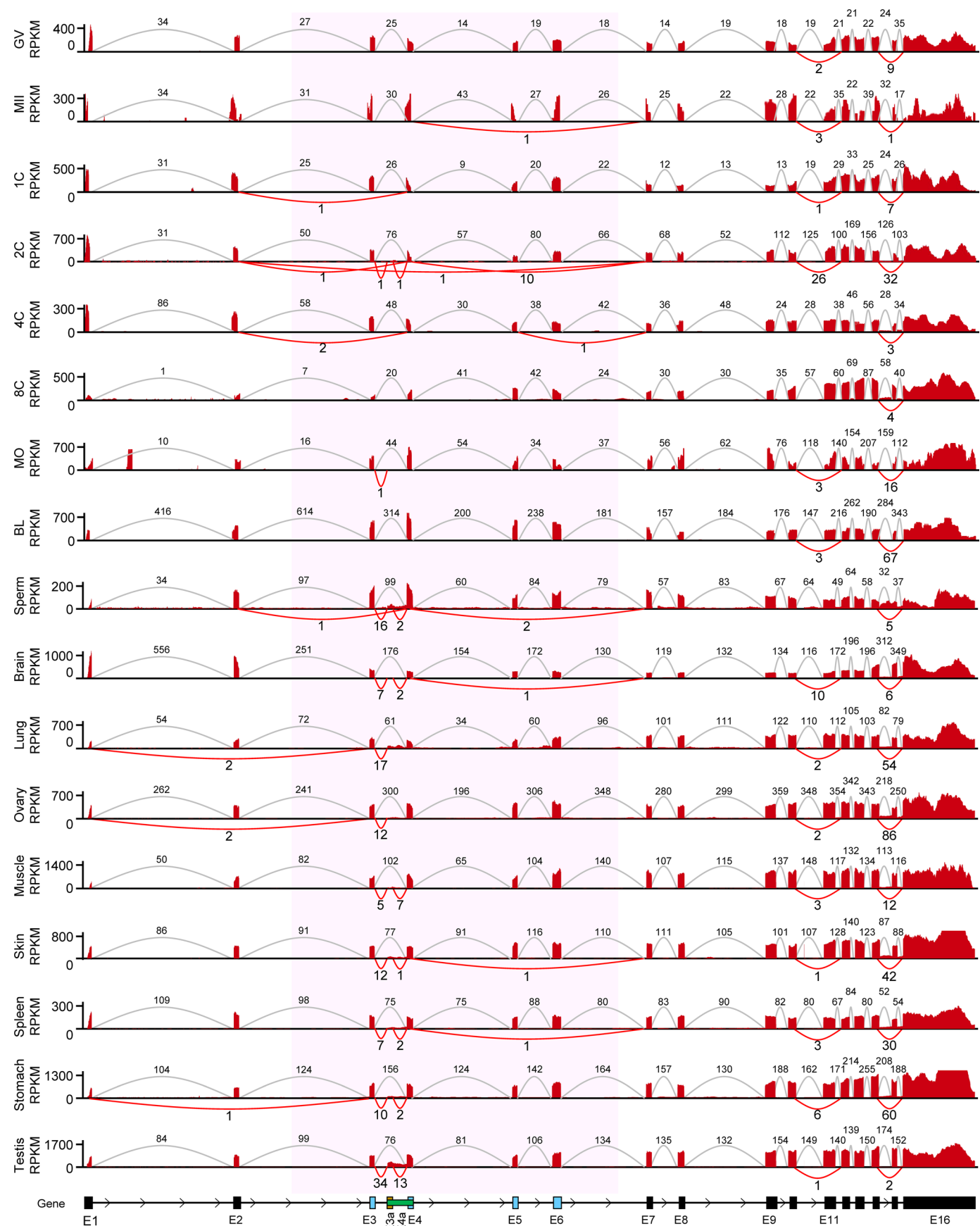
Extended Data Fig. 1 | Exon-skipping splicing (ESS) events of *Carm1* pre-mRNAs. Sashimi plots visualizing those ESS events of *Carm1* pre-mRNAs in mouse GV and MII oocytes; one-cell, and two-cell, embryos; sperm; as well as tissues including brain, lung, ovary, muscle, skin, spleen, stomach, and testis. Each line represents one set of data. The constitutive splicing events are shown in grey arcs and the alternative splicing events are shown in the red arcs.
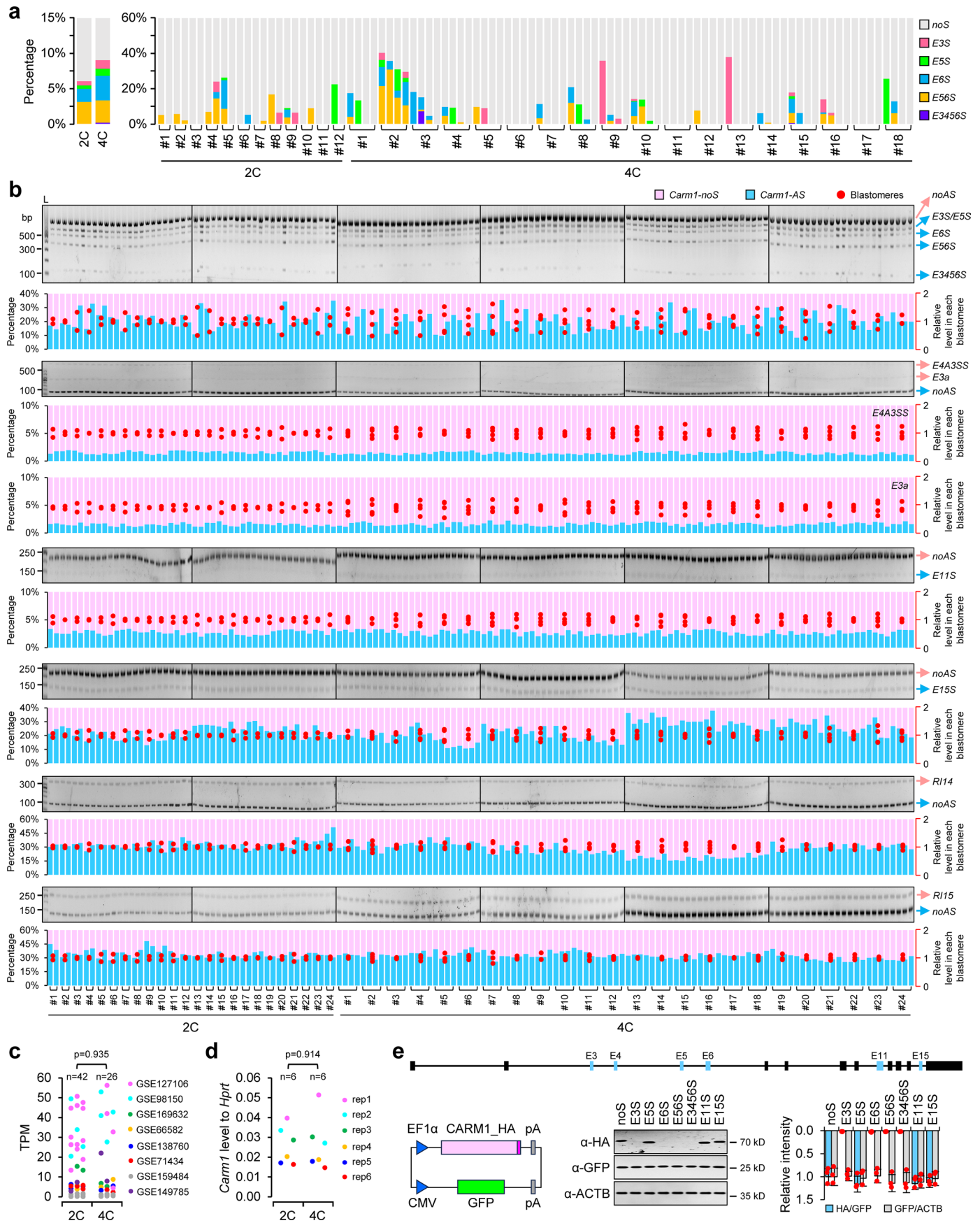
Extended Data Fig. 2 | See next page for caption.

Extended Data Fig. 2 | Heterogeneity of exon 3 to 6 skipping splicing of *Carm1* pre-mRNAs. a. Percentage of ESS events in mouse two- and four-cell embryos in total (left) or in each blastomere (right) sequenced via PacBio platform. **b**. The combination charts of bar plots depicting percentage of alternative splicing of *Carm1* pre-mRNAs (E3S, E5S, E6S, E56S, E3456S, E4A3SS, E11S, E15S, RI14, and RI15) in mouse late two- and early four-cell embryos and dot plots depicting the relative level of alternative splicing of *Carm1* pre-mRNAs among blastomeres in each embryo. Each dot or column respects one blastomere. noAS, non-alternative splicing. L, DNA ladder. Note that the results for exon 3 to 6 skipping splicing are also used in Extended Data Fig. 9b (L2C) and Extended Data Fig. 9c (E4C), and the spatial position information are shown in Extended Data Fig. 9b, c but not here. **c, d**. The dot plot depicting

Carm1 RNA levels based on RNA-seq data from two-cell embryos (n = 42) and four-cell embryos (n = 26) (c), and the qPCR results (d). **e**. The western blot results showing that the exon-skipping events of exons 3 to 6, but not exon 11 or 15, of *Carm1* pre-mRNAs seem to affect the protein level of CARM1. Top panel, illustration of exons of *Carm1* pre-mRNA. Bottom left panel, illustration of the vector from which HA-tagged CARM1 and green fluorescent protein (GFP) are expressed simultaneously, in which GFP works as a reference for exogenous transfection. Bottom middle panel, the western blot results. Bottom right panel, the combination charts of bar plots and dot plots showing the relative intensities of HA to GFP (HA/GFP) and GFP to ACTB (GFP/ACTB). EF1α, the promoter of human translation elongation factor 1 alpha. CMV, the promoter of cytomegalovirus. pA, the polyadenylation signal element. kD, kilodalton.
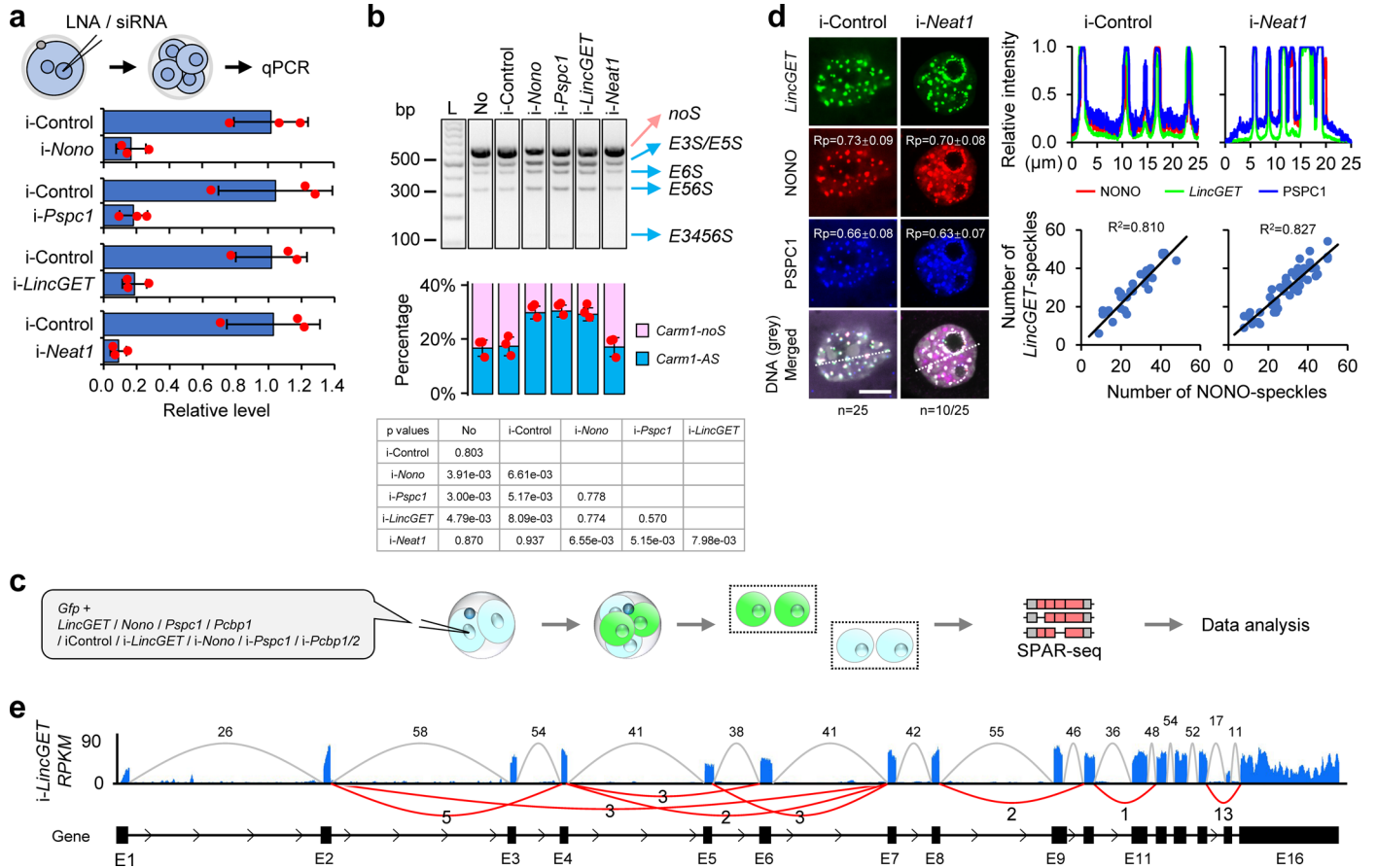
Extended Data Fig. 3 | *LincGET* participates in paraspeckles in mouse two-to four-cell embryos. a. Interference efficiency analysis of siRNAs on *Nono* and *Pspc1*, as well as locked nucleic acid (LNA) on *LincGET* and *Neat1*. Data are presented as mean values ± SEM (n = 3 biological replicates). **b**. Agarose gel analysis of RT-PCR showing changes of ESS of *Carm1* pre-mRNAs upon knockdown of *Nono*, *Pspc1*, *Neat1*, or *LincGET*. The percentages are shown below in combination charts of bar plots and dot plots. Data are presented as mean values ± SEM. One-tailed Student's t-tests were used for statistical analysis and p values are shown in the table below (n = 3 biological replicates). L, DNA ladder. No, group injected with nothing. **c**. Illustration of Systematic Parallel Analysis of Endogenous RNA Regulation Coupled to Barcode Sequencing (SPAR-seq). **d**. Fluorescence images showing *Neat1* depletion results in partial re-localization of

NONO and PSPC1 from paraspeckles to the periphery of the nucleoli. Scale bar, 10 μm. The Rp values are calculated by Fiji/ImageJ and shown on the pictures. Top right panel, line scans of the relative fluorescence intensity of signals indicated by the dotted line in left panel. Bottom right panel, the relationship between the numbers of *LincGET*-speckles and NONO-speckles calculated by Imaris (19 × 4 cells of i-Control group and 25 × 4 cells of i-*Neat1* group) is shown in the dot plot, and the R2 values were calculated in Excel. **e**. Sashimi plots visualizing that ESS happens on exons 3 to 6 of *Carm1* pre-mRNAs in mouse two-cell embryos upon *LincGET* depletion. The constitutive splicing events are shown in grey arcs and the alternative splicing events are shown in the red arcs. Note that the control group for *LincGET* depletion is the sample 2C in Fig. 1a, in which the control LNA is injected.

a

b

c i-*LincGET*

d

p values	i-Control	i-*LincGET* + *Gfp*	i-*LincGET* + *LincGET*-full	i-*LincGET* + *LincGET*-ΔA	i-*LincGET* + *LincGET*-ΔB	i-*LincGET* + *LincGET*-ΔC	i-*LincGET* + *LincGET*-ΔD	i-*LincGET* + *LincGET*-ΔE	i-*LincGET* + *LincGET*-ΔF	i-*LincGET* + *LincGET*-ΔG	i-*LincGET* + *LincGET*-ΔH	i-*LincGET* + *LincGET*-ΔI	i-*LincGET* + *LincGET*-ΔJ
i-*LincGET* + *Gfp*	3.67e-03												
i-*LincGET* + *LincGET*-full	0.0206	3.47e-04											
i-*LincGET* + *LincGET*-ΔA	0.0213	5.22e-04	0.8244										
i-*LincGET* + *LincGET*-ΔB	7.66e-03	7.08e-06	0.9479	0.7326									
i-*LincGET* + *LincGET*-ΔC	0.0118	3.07e-05	0.7412	0.5783	0.5784								
i-*LincGET* + *LincGET*-ΔD	0.0271	0.1477	1.85e-03	2.21e-03	5.08e-04	7.61e-04							
i-*LincGET* + *LincGET*-ΔE	0.0476	0.9315	6.38e-03	6.44e-03	4.46e-03	5.27e-03	0.5125						
i-*LincGET* + *LincGET*-ΔF	0.0115	6.46e-05	0.9784	0.7772	0.9571	0.6661	8.65e-04	5.05e-03					
i-*LincGET* + *LincGET*-ΔG	0.0121	0.1231	8.55e-04	1.14e-03	9.23e-05	1.85e-04	0.7076	0.6162	2.63e-04				
i-*LincGET* + *LincGET*-ΔH	9.62e-03	9.87e-03	5.70e-04	8.55e-04	6.35e-06	4.09e-05	0.9007	0.5080	9.51e-05	0.6397			
i-*LincGET* + *LincGET*-ΔI	0.0859	0.0937	4.98e-03	5.40e-03	2.23e-03	2.99e-03	0.5358	0.3245	3.03e-03	0.3394	0.4029		
i-*LincGET* + *LincGET*-ΔJ	0.0767	2.90e-03	0.7713	0.6597	0.7683	0.9052	8.26e-03	0.0135	0.7643	5.39e-03	5.02e-03	0.0166	
i-*LincGET* + *LincGET*-rev	6.05e-03	0.0412	4.37e-04	6.66e-04	3.69e-06	2.82e-05	0.4617	0.7076	6.95e-05	0.6324	0.0648	0.2206	3.92e-03

Extended Data Fig. 4 | See next page for caption.

Extended Data Fig. 4 | *LincGET* localizes to paraspeckles. a. Fluorescence images reflecting the expression pattern of *LincGET* and NONO (left) or PSPC1 (right) at different stages of mouse preimplantation embryos. Scale bar, 50 µm. Representative nuclei are shown below. The Rp values for co-localization of *LincGET* and NONO (left) or PSPC1 (right) in early two-cell embryos (E2C), late two-cell embryos (L2C), early four-cell embryos (E4C), and late four-cell embryos (L4C) are calculated by Fiji/ImageJ. Middle panel, line scans of the relative fluorescence intensity of signals indicated by the dotted lines in top panel. Bottom panel, the relationship between the numbers of *LincGET*-speckles and NONO-speckles (left, 18 × 2 cells of E2C, 24 × 2 cells of L2C, 15 × 4 cells of E4C, and 19 × 4 cells of L4C) or PSPC1-speckles (right, 17 × 2 cells of E2C, 23 × 2 cells of L2C, 14 × 4 cells of E4C, and 18 × 4 cells of L4C) calculated by Imaris is shown in

the dot plot, and the R^2 (coefficient of determination) values were calculated in Excel. 1C, one-cell embryos; 8C, eight-cell embryos; BL, blastocyst. **b**. Western blot results showing the expression pattern of NONO and PSPC1 during mouse early embryonic development. Three biological replicates were performed. Tubulin is used as a control. α-, anti. Data are presented as mean values ± SEM (n = 3 biological replicates). kD, kilodalton. **c**. Single channel of fluorescence images in Fig. 2f showing that *LincGET* deletion mutants in NONO/PSPC1 binding domain (ΔG, ΔH, or ΔI) cannot form speckles in E4C embryos. The *LincGET* signals were detected from the large amounts of injected *LincGET* or mutants. Scale bar, 10 µm. **d**. The p values for Fig. 2g. One-tailed Student's t-tests were used for statistical analysis (n = 3 biological replicates).

a

Carm1 (chr9:21,540,238-21,590,134)
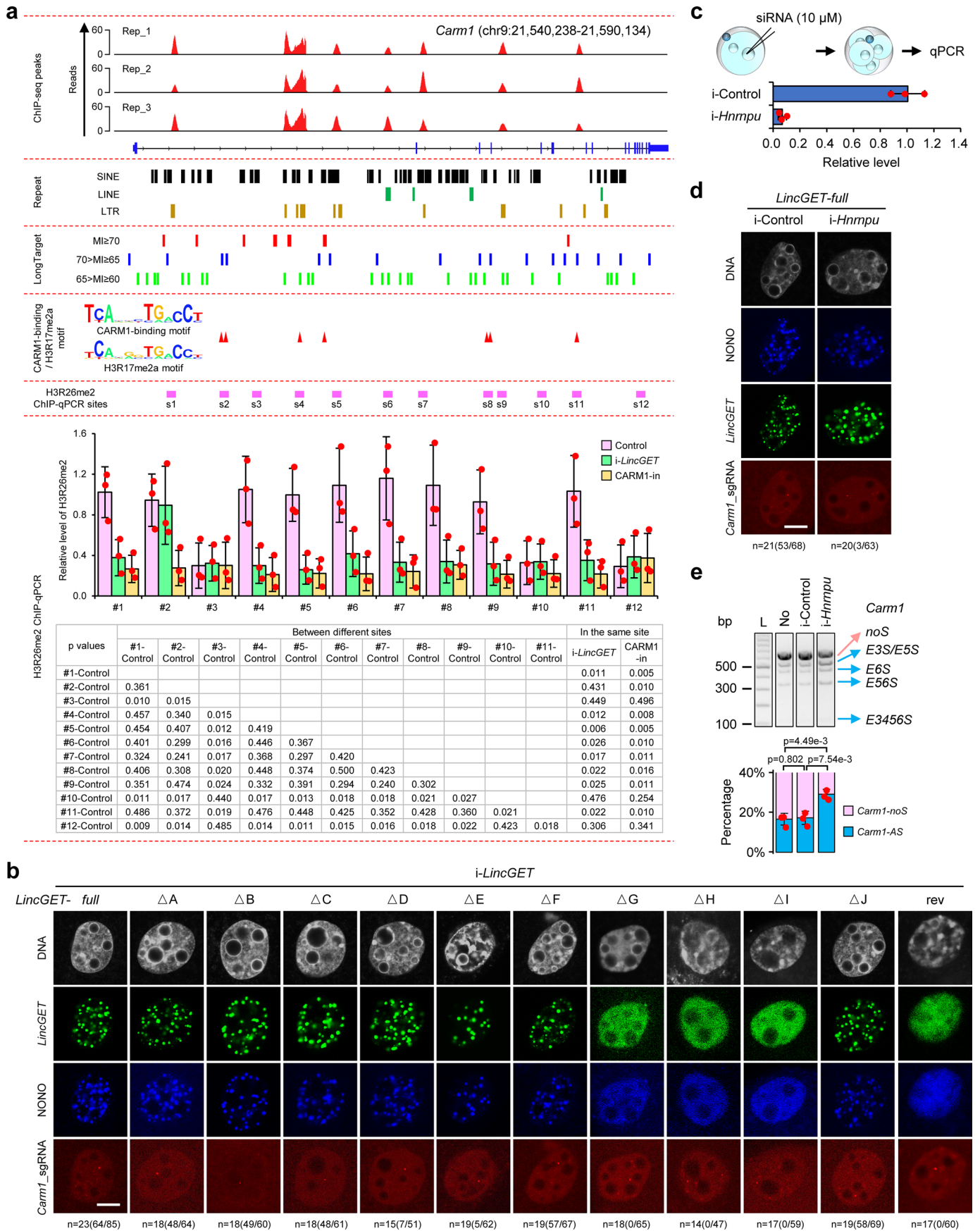
b i-LincGET

Extended Data Fig. 5 | See next page for caption.

Extended Data Fig. 5 | *LincGET* binds repeat sequences. a. Chromatin immunoprecipitation (ChIP) results showing that *LincGET* binds repeat sequences including SINE, LINE, and LTR in *Carm1* gene loci in E4C embryos. n = 3 biological replicates (rep_1, rep_2, and rep_3). ChIP-seq peaks lane, visualization of ChIP-seq peaks on *Carm1* gene locus. Repeat lane, the SINE, LINE, and LTR repeat elements in *Carm1* gene loci. SINE, short interspersed nuclear elements. LongTarget lane, the sequence complementarity of *LincGET* to the *Carm1* locus analyzed by *LongTarget*. MI, MeanIdentidy. CARM1-binding motif and H3R17me2a motif lane, the predicted CARM1-binding/H3R17me2a motif generated from the ChIP-seq data (PMID: 30456381). H3R17me2a, asymmetrically histone H3 arginine 17 dimethylation. H3R26me2 ChIP-qPCR sites lane, the tested sites by H3R26me2 ChIP-qPCR. H3R26me2, histone H3 arginine 26 dimethylation. H3R26me2 ChIP-qPCR lane top panel, combination charts of bar plots and dot plots showing the results of H3R26me2 ChIP-qPCR. Data are presented as mean 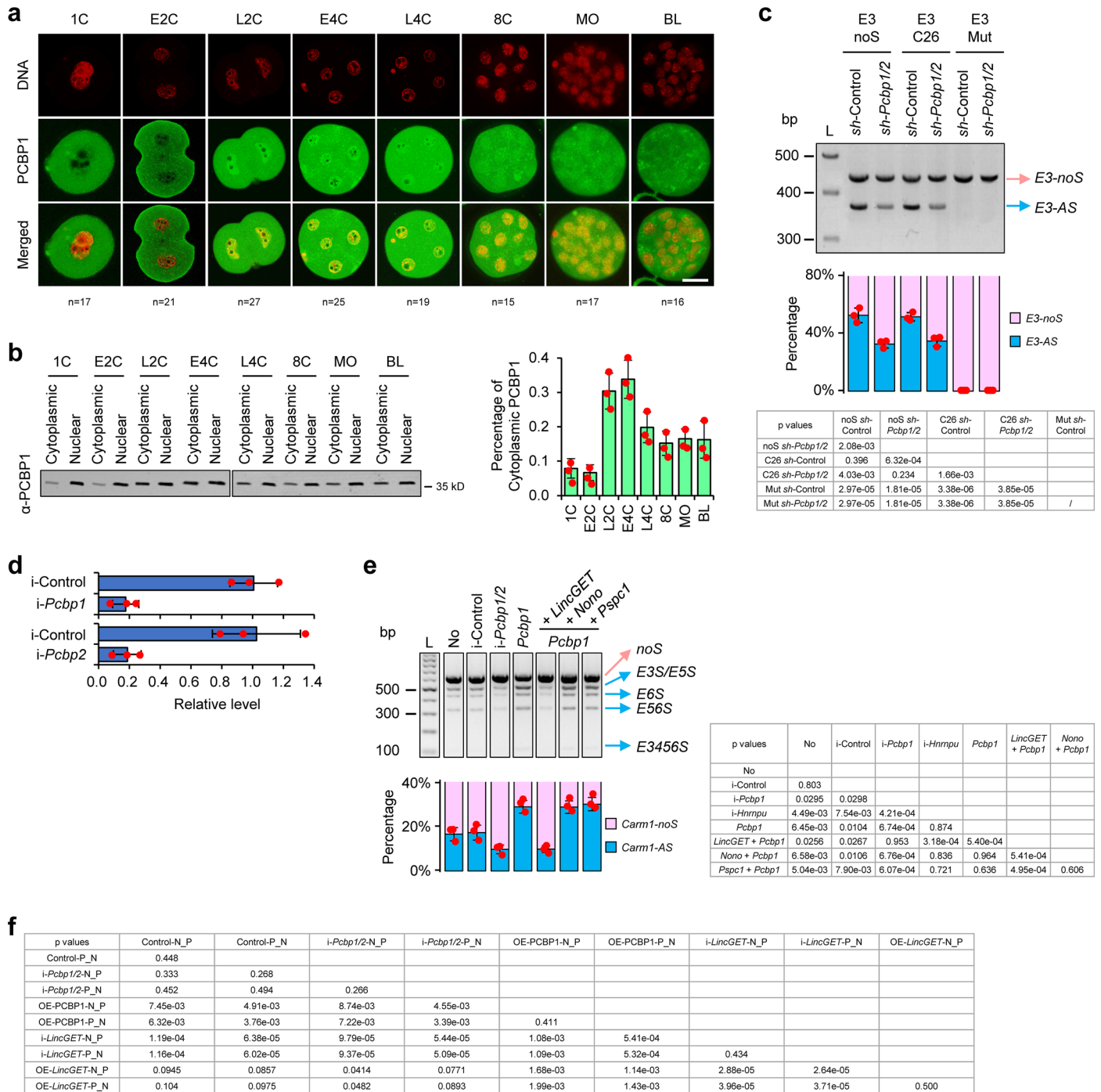values ± SEM (n = 3 biological replicates). H3R26me2 ChIP-qPCR lane bottom panel, one-tailed Student's t-tests were used for statistical analysis in H3R26me2 ChIP-qPCR lane top panel and the p values are shown in the table. For p values in the table, the left panel 'Between different sites' are p values between the control groups of different sites; the right panel 'In the same sites' are p values between the *LincGET* depletion (i-*LincGET*) and CARM1 inhibition (CARM1-in) groups of each site. **b**. Single channel of fluorescence images in Fig. 3d. Scale bar, 10 μm. The n values are shown as in Fig. 3d. **c**. Interference efficiency analysis of siRNAs on *Hnrnpu*. Data are presented as mean values ± SEM (n = 3 biological replicates). **d**. Single channel of fluorescence images in Fig. 3h. Scale bar, 10 μm. The n values are shown as in Fig. 3h. **e**. Agarose gel analysis of RT-PCR showing changes of ESS of *Carm1* pre-mRNAs upon *Hnrnpu* depletion. The percentages are shown below in combination charts of bar plots and dot plots. Data are presented as mean values ± SEM. One-tailed Student's t-tests were used for statistical analysis (n = 3 biological replicates). L, DNA ladder. No, group injected with nothing.
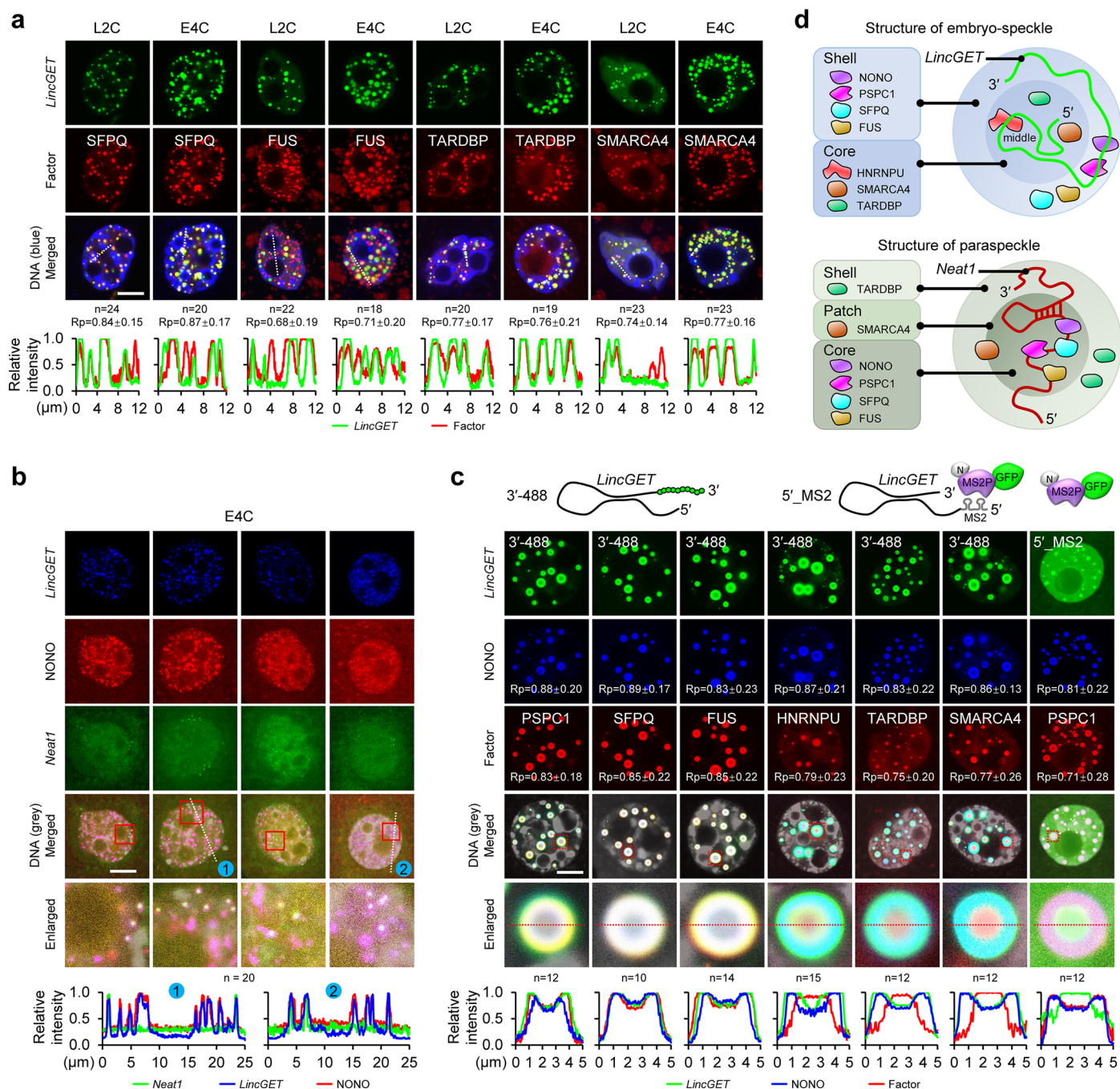
**Extended Data Fig. 6 | The structure of *LincGET*-speckle (embryo-speckle).**
a. Fluorescence images showing that *LincGET* co-localizes with SFPQ, FUS, TARDBP, and SMARCA4 in L2C and E4C embryos. Scale bar, 10 μm. The Rp values for co-localization of *LincGET* and SFPQ, FUS, TARDBP, or SMARCA4 are calculated by Fiji/ImageJ. Bottom panel, line scans of the relative fluorescence intensity of signals indicated by the dotted lines in top panel. **b**. Fluorescence images showing that *Neat1* co-localized with *LincGET* and NONO in mouse early four-cell embryos. Scale bar, 10 μm. Bottom panel, line scans of the relative fluorescence intensity of signals indicated by the dotted lines in top panel. **c**. Fluorescence images showing that the 3′-part of *LincGET*, NONO, PSPC1, SFPQ, and FUS locate in the shell, while the 5′-part of *LincGET*, HNRNPU, TARDBP, and

SMARCA4 locate in the core of *LincGET*-speckles. Scale bar, 10 μm. The Rp values for co-localization of *LincGET* and NONO (shown on images of blue channel) as well as *LincGET* and PSPC1, SFPQ, FUS, HNRNPU, TARDBP, or SMARCA4 (shown on images of red channel) are calculated by Fiji/ImageJ. Top panel, illustration of the injected 3′-488 (3′-Alexa Fluor™ 488-labelled *LincGET*), and 5′-MS2 (5′-MS2-labelled *LincGET* combine GFP-tagged MS2P with nucleus location signal (N)). Note that the GFP-tagged MS2P with nucleus location signal doesn't always bind to MS2-labelled *LincGET* and is dispersed throughout the nucleus. Bottom panel, line scans of the relative fluorescence intensity of signals indicated by the dotted line in top panel. **d**. Graphical representation of an *LincGET*-speckle (embryo-speckle) (top) and a *Neat1*-paraspeckle (bottom).

c p-values table:

p values	noS sh-Control	noS sh-Pcbp1/2	C26 sh-Control	C26 sh-Pcbp1/2	Mut sh-Control
noS sh-Pcbp1/2	2.08e-03				
C26 sh-Control	0.396	6.32e-04			
C26 sh-Pcbp1/2	4.03e-03	0.234	1.66e-03		
Mut sh-Control	2.97e-05	1.81e-05	3.38e-06	3.85e-05	
Mut sh-Pcbp1/2	2.97e-05	1.81e-05	3.38e-06	3.85e-05	/

e p-values table:

p values	No	i-Pcbp1	i-Control	i-Hnrnpu	Pcbp1	LincGET + Pcbp1	Nono + Pcbp1
No							
i-Control	0.803						
i-Pcbp1	0.0295	0.0298					
i-Hnrnpu	4.49e-03	7.54e-03	4.21e-04				
Pcbp1	6.45e-03	0.0104	6.74e-04	0.874			
LincGET + Pcbp1	0.0256	0.0267	0.953	3.18e-04	5.40e-04		
Nono + Pcbp1	6.58e-03	0.0106	6.76e-04	0.836	0.964	5.41e-04	
Pspc1 + Pcbp1	5.04e-03	7.90e-03	6.07e-04	0.721	0.636	4.95e-04	0.606

f

p values	Control-N_P	Control-P_N	i-Pcbp1/2-N_P	i-Pcbp1/2-P_N	OE-PCBP1-N_P	OE-PCBP1-P_N	i-LincGET-N_P	i-LincGET-P_N	OE-LincGET-N_P
Control-P_N	0.448								
i-Pcbp1/2-N_P	0.333	0.268							
i-Pcbp1/2-P_N	0.452	0.494	0.266						
OE-PCBP1-N_P	7.45e-03	4.91e-03	8.74e-03	4.55e-03					
OE-PCBP1-P_N	6.32e-03	3.76e-03	7.22e-03	3.39e-03	0.411				
i-LincGET-N_P	1.19e-04	6.38e-05	9.79e-05	5.44e-05	1.08e-03	5.41e-04			
i-LincGET-P_N	1.16e-04	6.02e-05	9.37e-05	5.09e-05	1.09e-03	5.32e-04	0.434		
OE-LincGET-N_P	0.0945	0.0857	0.0414	0.0771	1.68e-03	1.14e-03	2.88e-05	2.64e-05	
OE-LincGET-P_N	0.104	0.0975	0.0482	0.0893	1.99e-03	1.43e-03	3.96e-05	3.71e-05	0.500

Extended Data Fig. 7 | PCBP1 promotes ESS of *Carm1* via competitive binding to *Carm1* gene locus against *LincGET*-guided paraspeckles. a, **b**. The immunofluorescence results (**a**) and the western blotting results (**b**) of PCBP1 in mouse pre-implantation embryos, showing that PCBP1 was persistently expressed during mouse pre-implantation development, and PCBP1 was diffusely distributed in the cytoplasm and nucleus, but the nuclear localization is higher at late two- and early four-cell stages while is lower at one-cell and early two-cell stages than at other stages. The cytoplasm and nucleus are separated for western blotting. Three biological replicates were performed (**b**). Scale bar, 50 μm. α-, anti. Data are presented as mean values ± SEM (n = 3 biological replicates). kD, kilodalton. **c**. Top panel, splicing analysis using minigene containing exon 3 with flanked splicing acceptor and donor (SA and SD) sequences of *Carm1* pre-mRNAs. The splicing efficiency of exon 3 was assessed by RT-PCR. Middle panel, the percentages are shown in combination charts of

bar plots and dot plots for top panel. Data are presented as mean values ± SEM. Bottom panel, one-tailed Student's t-tests were used for statistical analysis and p values are shown in the table below (n = 3 biological replicates). L, DNA ladder. **d**. Interference efficiency analysis of siRNAs on *Pcbp1* and *Pcbp2*. Data are presented as mean values ± SEM (n = 3 biological replicates). **e**. Top left panel, agarose gel analysis of SPAR assays showing changes of ESS of *Carm1* pre-mRNAs upon *Pcbp1* overexpression or depletion. Bottom left panel, the percentages are shown in combination charts of bar plots and dot plots for top left panel. Data are presented as mean values ± SEM. Right panel, one-tailed Student's t-tests were used for statistical analysis in bottom left panel and p values are shown in the table (n = 3 biological replicates). L, DNA ladder. No, group injected with nothing. **f**. The p values for Fig. 4e. One-tailed Student's t-tests were used for statistical analysis (n = 3 biological replicates).
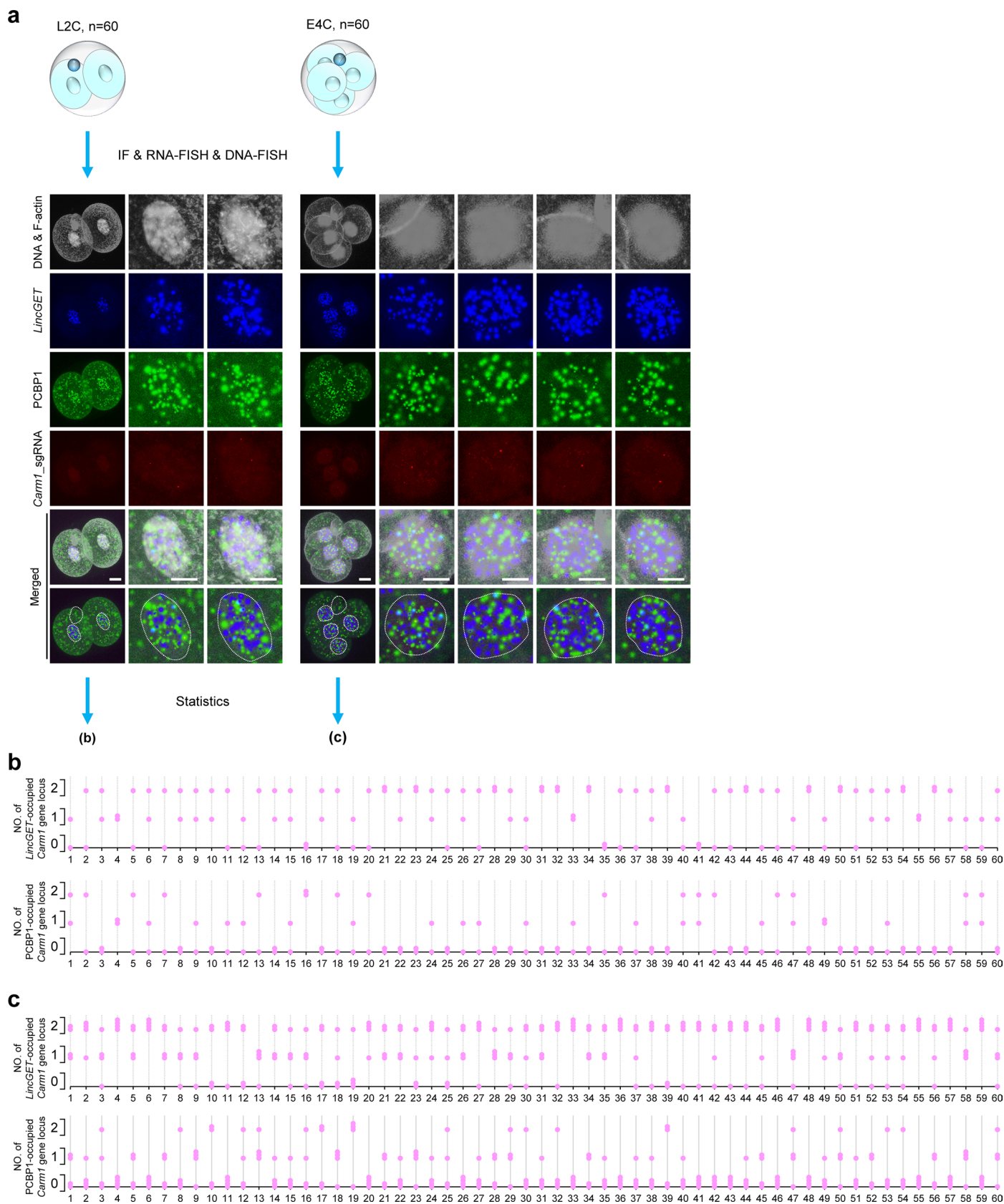
Extended Data Fig. 8 | Analysis of the heterogenous occupancy of *LincGET*-speckles and PCBP1 around the *Carm1* gene loci. a. Illustration of the analysis of the heterogenous occupancy of *LincGET*-speckles and PCBP1 around the *Carm1* gene loci using immunofluorescence (IF) combined with RNA-FISH and DNA-FISH. Representative fluorescence images are shown which exhibit the occupancy of *LincGET*-speckles or PCBP1 around the *Carm1* gene loci in late two- and early four-cell embryos. Scale bar, 10 μm. DNA & F-actin, the nucleus and membrane are displayed together with SYTOX™ Deep Red Nucleic Acid Stain (Invitrogen, S11380) and Alexa Fluor™ 647 Phalloidin (Invitrogen, A22287) to show the three-dimension structure of embryos. **b, c.** The dot plots showing the counting results of the number (NO.) of *LincGET*-occupied or PCBP1-occupied *Carm1* gene loci in late two- (**b**) and early four-cell embryos (**c**). To prevent the dots from overlapping completely, the y-axis is divided into three groups with NO. = 0, 1, and 2, respectively.
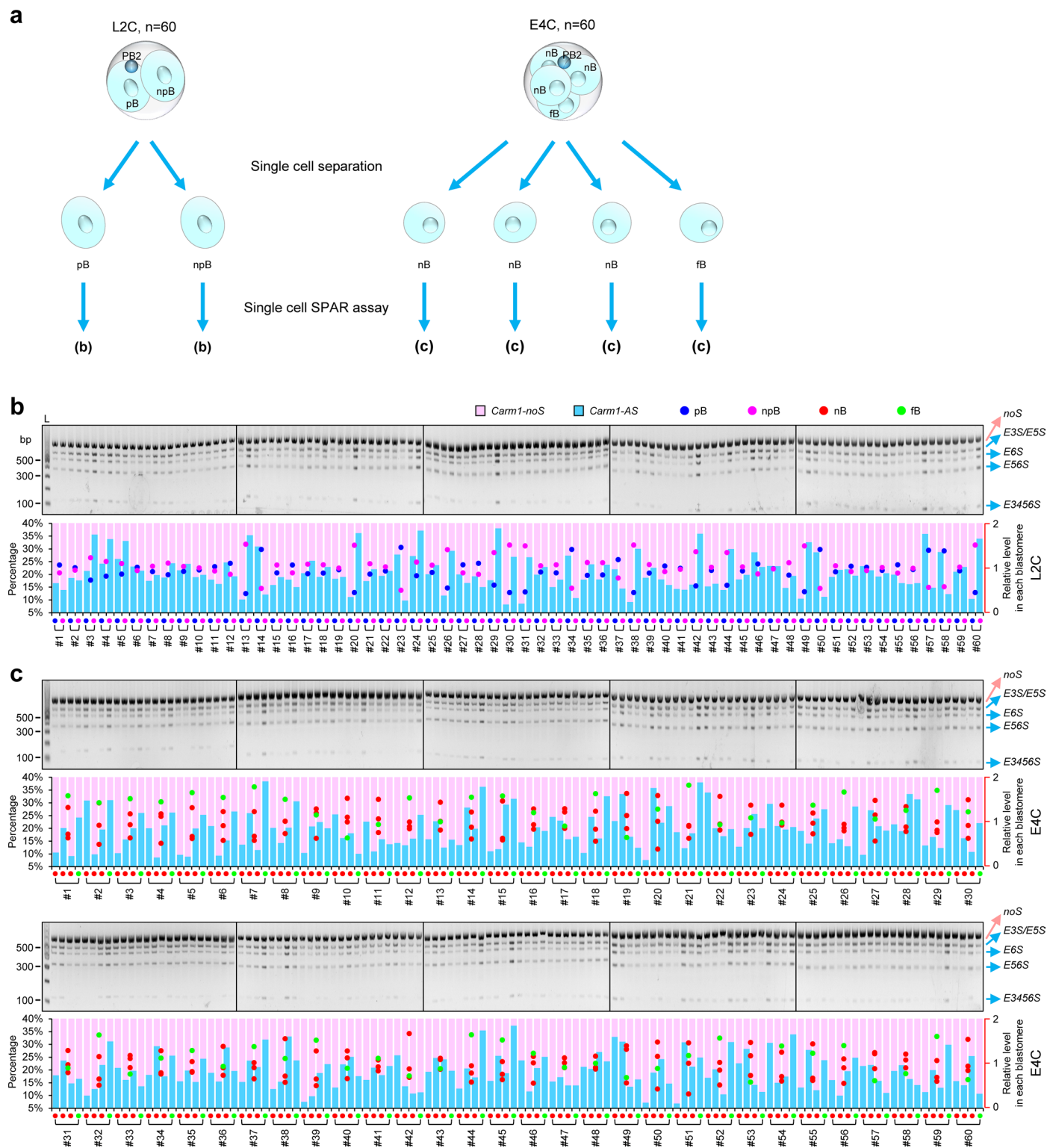
Extended Data Fig. 9 | Analysis of the heterogeneity of exon 3 to 6 skipping events of *Carm1* pre-mRNAs. a. Illustration of the analysis of the heterogeneity of exon 3 to 6 skipping events of *Carm1* pre-mRNAs via single-cell SPAR assay. **b, c**. Agarose gel analysis of single-cell SPAR assay showing the heterogeneity of exon-skipping events on exon 3 to 6 of *Carm1* pre-mRNAs in late two-cell (**b**) and early four-cell (**c**) embryos. The percentages are shown in bar plots below the gel. L, DNA ladder. Note that the embryos #1 to #24 of both L2C and E4C are also used in the results for exon 3 to 6 skipping splicing in Extended Data Fig. 2b, but the spatial position information are shown here with different colors for pB and npB as well as nB and fB, but not in Extended Data Fig. 2b.

a

b

c

d

p values	Total cells (n)	Outer cells (%)	GFP cells (%)	Outer cells that are GFP⁺ (%)	GFP cells that are outer (%)
Gfp vs i-*Pcbp1/2*	0.119	1.55e-03	0.915	0.803	0.392
Gfp vs Pcbp1	6.10e-03	4.19e-04	0.825	8.68e-06	7.22e-06
Pcbp1 vs i-*Pcbp1/2*	0.232	0.926	0.925	2.19e-06	1.25e-04
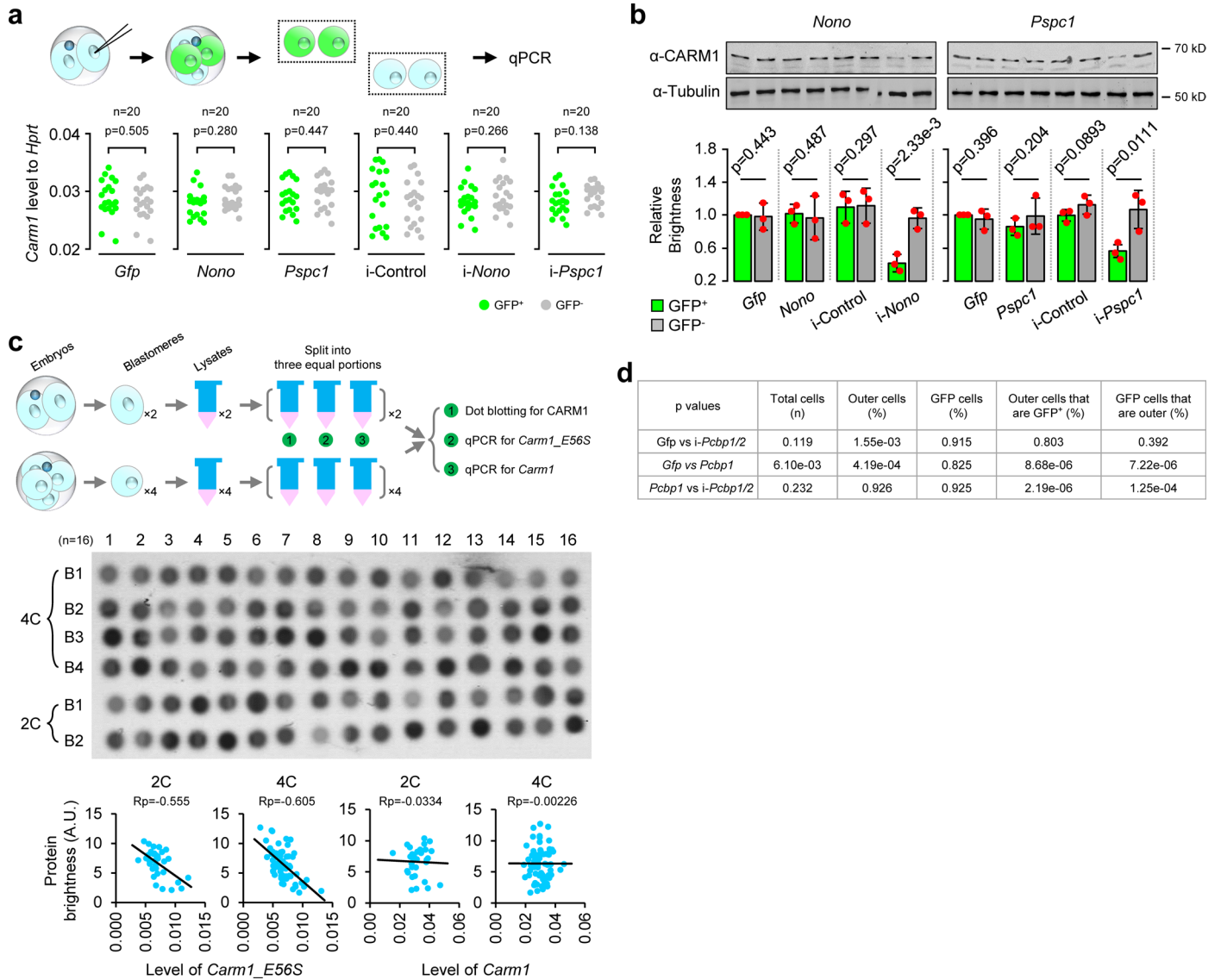
Extended Data Fig. 10 | NONO and PSPC1 regulate CARM1 protein level but not transcription level. a. Single-cell qPCR results showing neither *Nono* nor *Pspc1* affects the transcription level of *Carm1*. Two-tailed Student's *t*-tests were used for statistical analysis. **b**. Western blot results showing that *Nono* or *Pspc1* depletion downregulates CARM1 at the protein level. Tubulin is used as a control. Data are presented as mean values ± SEM (n = 3 biological replicates). Two-tailed Student's *t*-tests were used for statistical analysis. ns, *p* > 0.05. α-, anti.

kD, kilodalton. **c**. The ESS level but not the expression level of *Carm1* correlates with CARM1 protein level. The protein brightness from dot blotting is calculated by Fiji/ImageJ. Middle, results of dot plotting. Bottom, the relationship between protein brightness and expression level of the ESS isoform *Carm1_E56S* (Bottom left) or the total expression level of *Carm1* (Bottom right) is shown in the dot plot. The Rp values were calculated in Excel. **d**. The p values for Fig. 5i. One-tailed Student's *t*-tests were used for statistical analysis (n = 3 biological replicates).

Reporting Summary

Nature Portfolio wishes to improve the reproducibility of the work that we publish. This form provides structure for consistency and transparency in reporting. For further information on Nature Portfolio policies, see our Editorial Policies and the Editorial Policy Checklist.

Statistics

For all statistical analyses, confirm that the following items are present in the figure legend, table legend, main text, or Methods section.

n/a	Confirmed	
☐	☒	The exact sample size (*n*) for each experimental group/condition, given as a discrete number and unit of measurement
☒	☐	A statement on whether measurements were taken from distinct samples or whether the same sample was measured repeatedly
☐	☒	The statistical test(s) used AND whether they are one- or two-sided *Only common tests should be described solely by name; describe more complex techniques in the Methods section.*
☒	☐	A description of all covariates tested
☒	☐	A description of any assumptions or corrections, such as tests of normality and adjustment for multiple comparisons
☐	☒	A full description of the statistical parameters including central tendency (e.g. means) or other basic estimates (e.g. regression coefficient) AND variation (e.g. standard deviation) or associated estimates of uncertainty (e.g. confidence intervals)
☐	☒	For null hypothesis testing, the test statistic (e.g. F, t, r) with confidence intervals, effect sizes, degrees of freedom and P value noted *Give P values as exact values whenever suitable.*
☒	☐	For Bayesian analysis, information on the choice of priors and Markov chain Monte Carlo settings
☒	☐	For hierarchical and complex designs, identification of the appropriate level for tests and full reporting of outcomes
☐	☒	Estimates of effect sizes (e.g. Cohen's *d*, Pearson's *r*), indicating how they were calculated

Our web collection on statistics for biologists contains articles on many of the points above.

Software and code

Policy information about availability of computer code

Data collection	The majority of SPAR-seq data were mainly acquired from an Illumina MiSeq sequencer with 300 bp paired-end sequencing reactions (PE300) at BGI company (https://www.genomics.cn/), while partial were acquired from a PacBio Sequel System according to the standard PacBio Iso-Seq procedures at Annoroad company (http://www.annoroad.com/) mixed with samples from other experiments. The SHAPE-MaP data and the ChIP-seq data were both acquired from an Illumina HiSeq 2500 with 150 bp paired-end sequencing reactions (PE150) at BGI company (https://www.genomics.cn/). For exon-skipping splicing percentage analysis from published data, the raw data were downloaded from the GEO database.
Data analysis	For analysis of SPAR-seq data from PE300, clean reads were merged by pear (v0.9.6), reads were counted by bowtie2 (v2.2.5) and transferred into bam files with samtools (v1.9), and the Carm1_E3a_analysis.py (https://github.com/NEAU-Wang-lab/SPAR-seq) was used to note reads. For analysis of SPAR-seq data from PacBio, CCS reads were generated using ccs (v5.0.0) and converted to .fastq format using bam2fastq in the pbbam (v1.0.6). The number of passes for each of the raw CCS reads was generated using GetCCSpass.pl (https://github.com/Lulab-IGDB/polyA_analysis/blob/main/bin/). The Carm1_SPAR_reads_extract.py, Carm1_AS_analysis.py, and Carm1_E3a_analysis.py (https://github.com/NEAU-Wang-lab/SPAR-seq) were used to extract and count AS reads. For analysis of SHAPE-MaP data, ShapeMapper2 (v2.1.5) was used. The reads were mapped to target sequences by bowtie2 (v2.2.5). RNA secondary structures were modeled by Superfold (v1.0). The RNA stem-loop structures for specific fragments were produced by VARNA (v3.93). The .ct files from Superfold were used for visualization and varna_colors.txt files from ShapeMapper2 output were used for the reactivity coloring. For analysis of ChIP-seq data, reads were trimmed by trim_galore (v0.6.7), mapped to mouse genome sequences (https://ftp.ebi.ac.uk/pub/databases/gencode/Gencode_mouse/release_M29/GRCm39.primary_assembly.genome.fa.gz) by bwa (v 0.7.17-r1188), and transferred into .bam files with samtools (v1.9). The .bam files were loaded into the IGV (2.16.2) for visualization. Peak calling was performed by macs2 (2.1.1.20160309) software, after duplex removing by picard (2.18.29-0) software.

For exon-skipping splicing percentage analysis from published data, the trim_galore (v0.6.7) software was used to trim the original data with the default parameters. Next, the STAR software was used to align reads to mouse genome sequences (https://ftp.ebi.ac.uk/pub/databases/gencode/Gencode_mouse/release_M29/GRCm39.primary_assembly.genome.fa.gz) with default parameters. Then, the RMATS (v4.1.0) software was used to analyze the alternative splicing events and Rmats2sashimiplot (v2.0.4) software was used for visualization.

For manuscripts utilizing custom algorithms or software that are central to the research but not yet described in published literature, software must be made available to editors and reviewers. We strongly encourage code deposition in a community repository (e.g. GitHub). See the Nature Portfolio guidelines for submitting code & software for further information.

Data

Policy information about availability of data

All manuscripts must include a data availability statement. This statement should provide the following information, where applicable:

- Accession codes, unique identifiers, or web links for publicly available datasets
- A description of any restrictions on data availability
- For clinical datasets or third party data, please ensure that the statement adheres to our policy

Data availability
The sequencing data of SPAR-seq, SHAPE-MaP-seq, and LincGET-ChIP-seq have been deposited in the Genome Sequence Archive of Beijing Institute of Genomics, Chinese Academy of Sciences (GSA, http://gsa.big.ac.cn/) with the accession number of CRA007472, CRA007494, and CRA007495, respectively. This study also includes analysis of the following published data in Gene Expression Omnibus database (GEO): GSE85019, GSE71257, GSE163724, GSE135457, GSE45719, GSE127106, GSE138760, GSE153530, GSE98150, GSE66582, GSE135678, GSE151704, GSE171760, GSE160894, GSE169632, GSE137630, GSE161998, GSE180259, GSE165133, GSE117815, GSE178298, GSE162352, GSE181800, GSE173471, GSE242289, GSE194115, GSE194203, GSE201938, GSE226534, GSE192404, GSE151260, GSE156568, GSE228894, GSE199546, GSE189015, GSE150510, GSE148019, GSE184348, GSE179888, GSE181651, GSE197122, GSE167360, GSE234841, GSE202260, GSE190199, GSE114450, GSE196236, GSE147574, GSE235546, GSE71434, GSE159484, and GSE149785, and data in GSA: CRA007513.
The mouse genome sequences are available at the website https://ftp.ebi.ac.uk/pub/databases/gencode/Gencode_mouse/release_M29/GRCm39.primary_assembly.genome.fa.gz.

Research involving human participants, their data, or biological material

Policy information about studies with human participants or human data. See also policy information about sex, gender (identity/presentation), and sexual orientation and race, ethnicity and racism.

Reporting on sex and gender	n/a
Reporting on race, ethnicity, or other socially relevant groupings	n/a
Population characteristics	n/a
Recruitment	n/a
Ethics oversight	n/a

Note that full information on the approval of the study protocol must also be provided in the manuscript.

Field-specific reporting

Please select the one below that is the best fit for your research. If you are not sure, read the appropriate sections before making your selection.

☒ Life sciences   ☐ Behavioural & social sciences   ☐ Ecological, evolutionary & environmental sciences

For a reference copy of the document with all sections, see nature.com/documents/nr-reporting-summary-flat.pdf

Life sciences study design

All studies must disclose on these points even when the disclosure is negative.

Sample size	No statistical methods were used to pre-determine sample sizes but our sample sizes are similar to those used in previous publications (DOI: 10.1016/j.cell.2018.11.027).
Data exclusions	No data was excluded from the analysis.
Replication	All experiments were reliably reproduced. Each experiment was performed independently at least three times, but usually many more times.
Randomization	The embryos or cells were randomly assigned to each experimental groups.
Blinding	Blinding was not performed due to the unambiguous nature of measurements and systematic analyses used in these experiments.

Reporting for specific materials, systems and methods

We require information from authors about some types of materials, experimental systems and methods used in many studies. Here, indicate whether each material, system or method listed is relevant to your study. If you are not sure if a list item applies to your research, read the appropriate section before selecting a response.

Materials & experimental systems

n/a	Involved in the study
☐	☒ Antibodies
☐	☒ Eukaryotic cell lines
☒	☐ Palaeontology and archaeology
☐	☒ Animals and other organisms
☒	☐ Clinical data
☒	☐ Dual use research of concern
☒	☐ Plants

Methods

n/a	Involved in the study
☐	☒ ChIP-seq
☒	☐ Flow cytometry
☒	☐ MRI-based neuroimaging

Antibodies

Antibodies used	mouse monoclonal [G-2] anti-CARM1 (Santa Cruz, sc-393381), chicken polyclonal anti-GFP (Abcam, ab13970), rat monoclonal [YL1/2] anti-Tubulin (Abcam, ab6160), goat polyclonal anti-PCBP1 (Abcam, ab109577), rat monoclonal [EPR14859(2)] anti-PCBP2 (Abcam, ab200835), rat monoclonal [EPR8239] anti-SRSF1 (Abcam, ab129108), rabbit polyclonal anti-HA (Abcam, ab9110), rabbit polyclonal anti-NONO (Abcam, ab70335), rabbit polyclonal anti-PSPC1 (Abcam, ab104238), rabbit polyclonal anti-HNRNPU (Abcam, ab20666), rabbit polyclonal anti-U2AF2 (Abcam, ab37530), rabbit polyclonal anti-H3R26me2 (Abcam, ab127095) FITC-conjugated donkey anti-Chicken IgY polyclonal secondary antibody (Invitrogen, SA1-72000), Alexa Fluor Plus 555-conjugated goat anti-Mouse IgG polyclonal secondary antibody (Invitrogen, A32727), Alexa Fluor Plus 555-conjugated donkey anti-Goat IgG polyclonal secondary antibody (Invitrogen, A32816), Alexa Fluor Plus 555-conjugated donkey anti-Rabbit IgG polyclonal secondary antibody (Invitrogen, A32794), Alexa Fluor Plus 555-conjugated donkey anti-Rat IgG polyclonal secondary antibody (Invitrogen, A48270), Alexa Fluor 488-conjugated rabbit anti-Rat IgG polyclonal secondary antibody (Invitrogen, A-21210), HRP-conjugated goat anti-Rabbit IgG polyclonal secondary antibody (Invitrogen, A27036), HRP-conjugated mouse anti-Goat IgG polyclonal secondary antibody (Invitrogen, 31400), HRP-conjugated goat anti-Rat IgG polyclonal secondary antibody (Invitrogen, 31470)
Validation	All antibodies used are commonly used in the field and have been validated in previous publications/by the manufacturer. References and manufacturer validations can be found here: mouse monoclonal [G-2] anti-CARM1 (Santa Cruz, sc-393381; RRID: AB_2732840): https://www.scbt.com/p/carm1-antibody-g-2; Chicken polyclonal anti-GFP (Abcam, ab13970; RRID: AB_300798): https://www.abcam.cn/gfp-antibody-ab13970.html; Rat monoclonal [YL1/2] anti-Tubulin (Abcam, ab6160; RRID: AB_305328): https://www.abcam.cn/tubulin-antibody-yl12-loading-control-ab6160.html; Rabbit polyclonal anti-PCBP1 (Abcam, ab74793; RRID: AB_1281060): https://www.abcam.cn/pcbp1-antibody-ab74793.html; rat monoclonal [EPR14859(2)] anti-PCBP2 (Abcam, ab200835; RRID: AB_3094741): https://www.abcam.cn/products/primary-antibodies/pcbp2hnrnp-e2-antibody-epr148592-ab200835.html; Rabbit monoclonal anti-SRSF1 (Abcam, ab129108; RRID: AB_11141636): https://www.abcam.cn/sf2-antibody-epr8239-ab129108.html; Rabbit polyclonal anti-HA (Abcam, ab9110; RRID: AB_307019): https://www.abcam.cn/ha-tag-antibody-chip-grade-ab9110.html; Rabbit polyclonal anti-NONO (Abcam, ab70335; RRID: AB_1269576): https://www.abcam.cn/nmt55-p54nrb-antibody-ab70335.html; Rabbit polyclonal anti-PSPC1 (Abcam, ab104238; RRID: AB_11157752): https://www.abcam.cn/pspc1-antibody-ab104238.html; Rabbit polyclonal anti-hnRNPU (Abcam, ab20666; RRID: AB_732983): https://www.abcam.cn/hnrnp-up120-antibody-ab20666.html; rabbit polyclonal anti-U2AF2 (Abcam, ab37530; RRID:AB_883336): https://www.abcam.cn/products/primary-antibodies/u2af65-antibody-ab37530.html; Rabbit polyclonal anti-H3R26me2 (Abcam, ab127095; RRID: AB_2732841): https://www.abcam.cn/histone-h3-symmetric-di-methyl-r26-antibody-ab127095.html.

Eukaryotic cell lines

Policy information about cell lines and Sex and Gender in Research

Cell line source(s)	The mouse epiblast stem cells (mEpiSCs) were established in Qi Zhou's lab in State Key Laboratory of Stem Cell and Reproductive Biology, Institute of Zoology, Chinese Academy of Sciences. The MCF7 cells were purchased from ATCC (ATCC, HTB-22).

Authentication	Identity of mEpiSCs cell line was frequently checked by the morphological features, but not authenticated. Identity of MCF7 cell line was frequently checked by the morphological features, but not authenticated.
Mycoplasma contamination	The mEpiSCs cell line was regularly tested for mycoplasma contamination and no contamination was found. The MCF7 cell line was regularly tested for mycoplasma contamination and no contamination was found.
Commonly misidentified lines (See ICLAC register)	No commonly misidentified cell lines were used.

Animals and other research organisms

Policy information about studies involving animals; ARRIVE guidelines recommended for reporting animal research, and Sex and Gender in Research

Laboratory animals	The CD1 (ICR) mice were purchased from Vital River company. All mice used for experiments were seven- to eight-week-old. All mice were housed under specific pathogen-free conditions with a 12-hour dark/light cycle, an ambient temperature ranging from 21°C to 26°C, and a humidity level of 50% to 60%, in the animal care facilities at the Institute of Zoology, Chinese Academy of Sciences. To obtain preimplantation embryos, female mice were injected with 10 U of pregnant mare serum gonadotropin (PMSG, Prospec, HOR-272) and 10 U of human chorionic gonadotropin (hCG, Prospec, HOR-250) at 46- to 48-hour intervals, and then crossed with 7- to 8-week-old CD1 (ICR) male mice. Embryos were collected at the following times post hCG injection: early one-cell stage (phCG 19 hours), late one-cell stage (phCG 30 hours), early two-cell stage (phCG 39 hours), late two-cell stage (phCG 48 hours), early four-cell stage (phCG 54 hours), late four-cell stage (phCG 62 hours), early eight-cell stage (phCG 68 hours), late eight-cell stage (phCG 74 hours), 16-cell stage (phCG 80 hours), 32-cell stage (phCG 90 hours), early blastocyst stage (phCG 98 hours), and late blastocyst stage (phCG 114 hours).
Wild animals	No wild animals were used in the study.
Reporting on sex	No sex-based experiments were performed.
Field-collected samples	No field-collected samples were used.
Ethics oversight	All the mouse procedures are carried out in compliance with the guidelines of the Animal Care and Use Committee of the Institute of Zoology, Chinese Academy of Sciences, and the Animal Care and Use Committee of the Northeast Agricultural University.

Note that full information on the approval of the study protocol must also be provided in the manuscript.

Plants

Seed stocks	n/a
Novel plant genotypes	n/a
Authentication	n/a

ChIP-seq

Data deposition

☒ Confirm that both raw and final processed data have been deposited in a public database such as GEO.

☒ Confirm that you have deposited or provided access to graph files (e.g. BED files) for the called peaks.

Data access links *May remain private before publication.*	The raw data have been deposited in GSA with the access link, https://ngdc.cncb.ac.cn/gsa/s/QcU5dfun. The processed data in bam file and the bed file for the call peaks have been deposited in the OMIX, China National Center for Bioinformation / Beijing Institute of Genomics, Chinese Academy of Sciences (https://ngdc.cncb.ac.cn/omix), with accession no. OMIX004027 and OMIX004026, respectively.
Files in database submission	input: input_1.fq.gz, input_2.fq.gz LincGET_ChIP_rep1: V350003627_L04_612_1.fq.gz, V350003627_L04_612_2.fq.gz LincGET_ChIP_rep2: V350003627_L04_613_1.fq.gz, V350003627_L04_613_2.fq.gz LincGET_ChIP_rep3, V350003627_L04_614_1.fq.gz, V350003627_L04_614_2.fq.gz
Genome browser session (e.g. UCSC)	https://ftp.ebi.ac.uk/pub/databases/gencode/Gencode_mouse/release_M30/GRCm39.primary_assembly.genome.fa.gz https://ftp.ebi.ac.uk/pub/databases/gencode/Gencode_mouse/release_M32/ gencode.vM32.chr_patch_hapl_scaff.annotation.gtf.gz

Methodology

Replicates	One replicates for input, and three replicates for ChIP.
Sequencing depth	Sequencing depth for input, LincGET_ChIP_rep1, LincGET_ChIP_rep2, and LincGET_ChIP_rep3 were 4,673,619,900, 4,785,825,600,

Sequencing depth	4,790,067,900, and 4,807,644,300, respectively. Total number of reads for input, LincGET_ChIP_rep1, LincGET_ChIP_rep2, and LincGET_ChIP_rep3 were 31,157,466, 31,905,504, 31,933,786, and 32,050,962, respectively. Total number of uniquely mapped reads for input, LincGET_ChIP_rep1, LincGET_ChIP_rep2, and LincGET_ChIP_rep3 were 29,990,741, 29,211,776, 29,118,337, and 29,271,751, respectively. Length of reads is 150 bp. Reads were paired-end.
Antibodies	rabbit polyclonal anti-HA antibody (Abcam, ab9110)

Peak calling parameters	# index building
	$ bwa index mm10.fa -p mm10
	# reads mapping
	$ bwa mem -M -t 8 index/mm10 input_1.fq.gz input_2.fq.gz > input.bwa.sam
	$ bwa mem -M -t 8 index/mm10 V350003627_L04_612_1.fq.gz V350003627_L04_612_2.fq.gz > LincGET_rep1.bwa.sam
	$ bwa mem -M -t 8 index/mm10 V350003627_L04_613_1.fq.gz V350003627_L04_613_2.fq.gz > LincGET_rep2.bwa.sam
	$ bwa mem -M -t 8 index/mm10 V350003627_L04_614_1.fq.gz V350003627_L04_614_2.fq.gz > LincGET_rep3.bwa.sam
	# unmapped reads removing and sorting
	$ samtools view -bS -F 4 input.bwa.sam > input.bwa.mapped.bam
	$ samtools view -bS -F 4 LincGET_rep1.bwa.sam > LincGET_rep1.bwa.mapped.bam
	$ samtools view -bS -F 4 LincGET_rep2.bwa.sam > LincGET_rep2.bwa.mapped.bam
	$ samtools view -bS -F 4 LincGET_rep3.bwa.sam > LincGET_rep3.bwa.mapped.bam
	$ samtools sort input.bwa.mapped.bam > input.bwa.mapped.sort.bam
	$ samtools sort LincGET_rep1.bwa.mapped.bam > LincGET_rep1.bwa.mapped.sort.bam
	$ samtools sort LincGET_rep2.bwa.mapped.bam > LincGET_rep2.bwa.mapped.sort.bam
	$ samtools sort LincGET_rep3.bwa.mapped.bam > LincGET_rep3.bwa.mapped.sort.bam
	# duplex removing
	$ picard MarkDuplicates REMOVE_DUPLICATES=true I= input.bwa.mapped.sort.bam O= input_deduplicate_bam M= input.log; done
	$ picard MarkDuplicates REMOVE_DUPLICATES=true I= LincGET_rep1.bwa.mapped.sort.bam O= LincGET_rep1_deduplicate_bam M= input.log; done
	$ picard MarkDuplicates REMOVE_DUPLICATES=true I= LincGET_rep2.bwa.mapped.sort.bam O= LincGET_rep2_deduplicate_bam M= input.log; done
	$ picard MarkDuplicates REMOVE_DUPLICATES=true I= LincGET_rep3.bwa.mapped.sort.bam O= LincGET_rep3_deduplicate_bam M= input.log; done
	# peak calling
	$ macs2 callpeak -t LincGET_rep1_deduplicate_bam -c input_deduplicate_bam -f BAMPE -g mm -n LincGET_rep1 -B -q 0.05
	$ macs2 callpeak -t LincGET_rep2_deduplicate_bam -c input_deduplicate_bam -f BAMPE -g mm -n LincGET_rep1 -B -q 0.05
	$ macs2 callpeak -t LincGET_rep3_deduplicate_bam -c input_deduplicate_bam -f BAMPE -g mm -n LincGET_rep1 -B -q 0.05

Data quality	The number of peaks at FDR 5% and above 5-fold enrichment in LincGET_ChIP_rep1, LincGET_ChIP_rep2, and LincGET_ChIP_rep3 are 43,794, 43,095, and 43,082, respectively.
Software	The deep sequencing datasets of LincGET-ChIP-seq were trimmed by trim_galore (v 0.6.7) software with default parameters. The reads were mapped to mouse genome sequences (https://ftp.ebi.ac.uk/pub/databases/gencode/Gencode_mouse/release_M29/GRCm39.primary_assembly.genome.fa.gz) by bwa (v 0.7.17-r1188) software with default parameters and transferred into .bam files with samtools (v1.9) software. The .bam files were loaded into the IGV for visualization. Peak calling was performed by macs2 (2.1.1.20160309) software, after duplex removing by picard (2.18.29-0) software.